

THESIS FOR THE DEGREE OF DOCTOR OF PHILOSOPHY

Nanoscale $\text{YBa}_2\text{Cu}_3\text{O}_{7-\delta}$ devices
-Searching for a subdominant order parameter using a single electron
transistor

DAVID GUSTAFSSON



Department of Microtechnology and Nanoscience - MC2
CHALMERS UNIVERSITY OF TECHNOLOGY
Göteborg, Sweden 2012

Nanoscale $\text{YBa}_2\text{Cu}_3\text{O}_{7-\delta}$ devices

-Searching for a subdominant order parameter using a single electron transistor

DAVID GUSTAFSSON

ISBN 978-91-7385-680-5

© DAVID GUSTAFSSON, 2012.

Doktorsavhandlingar vid Chalmers tekniska högskola

Ny serie nr 3361

ISSN 0346-718X

Quantum Device Physics Laboratory

Department of Microtechnology and Nanoscience - MC2

Chalmers University of Technology

SE-412 96 Göteborg

Sweden

Telephone: +46 (0)31-772 1000

ISSN 1652-0769

Technical Report MC2-228

Chalmers Reproservice

Göteborg, Sweden 2012

Nanoscale $\text{YBa}_2\text{Cu}_3\text{O}_{7-\delta}$ devices

-Searching for a subdominant order parameter using a single electron transistor

DAVID GUSTAFSSON

Department of Microtechnology and Nanoscience

Chalmers University of Technology

Göteborg, Sweden 2012

Abstract

The microscopic origin of High critical Temperature Superconductivity (HTS) is still an open issue in condensed matter physics. It is believed that by exploring the quasiparticle energy spectrum one can learn about the mechanism promoting the superconducting state.

In this thesis we have developed a nanoscale spectroscopic tool, an all superconducting $\text{YBa}_2\text{Cu}_3\text{O}_{7-\delta}$ (YBCO) Single Electron Transistor, allowing us to obtain information from the quasiparticle spectrum of an entire nanometer scale island. In this experiment we find a fully gapped superconductivity which strongly depends on the externally applied magnetic field. This finding shows that the order parameter is not purely $d_{x^2-y^2}$ with nodes, instead it has an additional subdominant imaginary component which lifts the zero energy quasiparticles.

The realization of the transistor has required the engineering of nanoscale YBCO Josephson grain boundary (GB) junctions with stringent demands on the transport properties. Part of the work in this thesis has been devoted to the development and characterization of two methods to fabricate nanoscale GB junctions. A conventional method based on e-beam lithography and ion milling and a new soft nanopatterning technique. The new method is based on the phase competition between superconducting YBCO and insulating greenphase at the grain boundary. This has allowed the creation of junctions with minimal damage in the fabrication process. Together, the two methods create grain boundaries that span a large range of critical current densities and normal resistivities, which can be employed in various applications.

Keywords: Josephson junctions, high temperature superconductivity, single electron transistors, grain boundary, YBCO

LIST OF APPENDED PAPERS

This thesis is based on the work contained in the following papers

- I. **Soft Nanostructuring of YBCO Josephson Junctions by Phase Separation**
D. Gustafsson, H. Pettersson, B. Iandolo, E. Olsson, T. Bauch and F. Lombardi
Nano Letters **10**, 4824 (2010).
- II. **Noise properties of nanoscale $\text{YBa}_2\text{Cu}_3\text{O}_{7-\delta}$ Josephson junctions**
D. Gustafsson, F. Lombardi, and T. Bauch
Physical Review B **84**, 184526 (2011)
- III. **Low capacitance HTS junctions for single electron transistors**
D. Gustafsson, T. Bauch, S. Nawaz, M. Mumtaz Virk, G. Signorello, and F. Lombardi
Physica C **470**, S188 (2010).
- IV. **Fully gapped superconductivity in a nanometer size $\text{YBa}_2\text{Cu}_3\text{O}_{7-\delta}$ island**
D. Gustafsson, D. Golubev, M. Fogelström, T. Bauch and F. Lombardi
Manuscript (2012)
- V. **High critical temperature superconductor Josephson junctions for quantum circuit applications**
T. Bauch, D. Gustafsson, K. Cedergren, S. Nawaz, M. Mumtaz Virk, H. Pettersson, E. Olsson, and F. Lombardi
Physica Scripta **T173**, 014006 (2009).

Contents

1	Introduction	1
2	Introduction to superconductivity	5
2.1	Superconductivity	5
2.2	Brief review of the basic properties of HTS	6
3	The Josephson effect	11
3.1	The resistively and capacitively shunted junction model . . .	12
3.2	Josephson junctions in magnetic field	16
3.3	Superconducting Quantum Interference Device	17
3.4	N Josephson junctions in parallel	21
4	Grain boundaries	23
4.1	HTS Josephson Junctions	23
4.1.1	Bicrystal junctions	24
4.1.2	Step-edge junctions	24
4.1.3	Biepitaxial junctions	26
4.1.4	The $I_C R_N$ -product	26
4.2	The grain boundary interface	27
4.2.1	The filament model	27
4.2.2	The intrinsically shunted junction model	28
4.2.3	Homogeneous barrier, SIS	28
4.2.4	The band-bending model	29
4.3	Noise and the transport models for HTS GBs	30
4.4	Effects of d -wave symmetry on GB	32
4.4.1	Faceting	32
4.4.2	Andreev reflection	33
5	The single electron transistor	37
5.1	The single electron transistor	37
5.2	Superconducting SET	44

5.2.1	The NISIN SET	44
5.2.2	The SISIS SET	46
6	Fabrication of grain boundary junctions	51
6.1	The choice of substrate	51
6.2	Fabrication of biepitaxial grain boundary junctions	52
6.3	Nucleation of greenphase on MgO (110)	56
6.4	Soft nanopatterning	59
7	The measurement setups	61
7.1	280 mK system - Heliox	61
7.2	15 mk system	63
8	DC characterization of nano grain boundary junctions	65
8.1	Critical current densities and normal resistances	65
8.2	Testing the validity of the soft nanopatterning method	68
8.3	Extracting the effective width - Soft nanopatterned junctions	69
8.4	Extracting the effective width - Conventionally nanopatterned junctions	70
8.5	Characterization of a nanoSQUID	71
9	Noise characterization of nano grain boundary junctions	73
9.1	S_i and S_r	74
9.2	2-level fluctuators	76
9.2.1	2-level fluctuators in conventionally nanopatterned junctions	78
10	An all YBCO single electron transistor	81
10.1	Nanojunctions by direct etching through a carbon mask	82
10.2	Big island SET	82
10.2.1	Characterization	83
10.2.2	Results for Big island SETs	84
10.3	Single grain SET	87
10.3.1	Results for single grain SET	89
10.3.2	Detailed characterization of the device	89
10.3.3	Fitting IV characteristics to the orthodox theory to ex- tract C , Δ , T_{eff} and E_C	92
10.4	Size quantization	95
10.5	Conclusions	97
11	Conclusions	99

A Fabrication of biepitaxial grain boundaries	101
Acknowledgements	105
Bibliography	107
Appended papers	117

Definitions of symbols

θ	Phase of the superconducting wavefunction
ϕ	Phase difference across a junction $\theta_1 - \theta_2$
Ψ	Superconducting wavefunction
S_V	Voltage-noise spectral density, [V ² /Hz]
S_i	Relative current-noise spectral density, [1/Hz]
S_i^{RTS}	Relative noise spectral density of a 2-level charge trap, [1/Hz]
q	Ratio between the current and resistance spectral densities, $q = \sqrt{S_i/S_r}$
A_J	Total junction area
A_t	Charge trap cross-sectional area
A_{cp}	Cooper pair transport channel area
A_{qp}	Quasiparticle transport channel area
Φ_0	Flux quantum, $h/2e$
E_C	Charging energy, $e^2/2C_\Sigma$
E_J	Josephson energy, $\frac{\hbar}{2e}I_C$
F	Even-odd free energy
V_{SD}	Source drain voltage
V_g	Gate voltage
n_g	Normalized gate induced charge, $n_g = C_g V_g / e$
λ_L	London penetration depth
λ_J	Josephson penetration depth
R_N	Normal Resistance
ρ_N	Specific resistance
I_C	Critical current
J_C	Critical current density

List of Abbreviations

SET	Single Electron Transistor
GB	Grain Boundary
SQUID	Superconducting QUantum Interference Device
SEM	Scanning Electron Microscope
AFM	Atomic Force Microscope
TEM	Transmission Electron Microscope
FIB	Focused Ion Beam
IVC	Current Voltage Characteristics
CPR	Current Phase Relation
LTS	Low critical Temperature Superconductor
HTS	High critical Temperature Superconductor

Chapter 1

Introduction

At the time of the completion of this thesis the superconducting phenomenon has just celebrated its 100th anniversary since its discovery. The microscopic origin of conventional superconductivity is well explained by the Bardeen-Cooper-Schrieffer (BCS) theory where the electron-phonon interaction is responsible for the formation of Cooper-pairs, consisting of two electrons with opposite spin and momentum. The condensate of the Cooper pairs determines the long range coherent ground state of the system. The BCS theory has experienced great success in explaining the phenomenology of conventional metal (and compound) superconductors. For the cuprate High Temperature Superconductors (HTS) discovered by Bednorz and Müller in 1986 a microscopic theory is still missing.

The difficulties in formulating a microscopic theory for the HTS materials are related to a delicate competition of several degrees of freedom; charge, spin, orbital and lattice requiring a strongly correlated electron picture. At doping levels below the onset of superconductivity the cuprates are in an antiferromagnetic Mott insulator state. Doping into a Mott insulator is commonly used as a starting point for the evolution into a superconducting state. The mechanism behind superconductivity in these materials is not generally agreed upon. Several models that give a net attractive interaction energy between electrons have been suggested. Both scenarios where phonon interactions are assisting in the pairing and models that achieve the pair creation without phonons have been proposed. It has been realized that if the phonons are involved in the pair condensation the mechanism must be more complex than in the BCS theory. Among the theories that do not require assistance from the phonons to form pairs, a model based on the spin-spin interaction of the electrons has received a noticeable amount of attention. Here the spin-interaction potential of elec-

trons of opposite spins will oscillate in space and can, for certain conditions, result in a net attractive force, resulting in the formation of a spin singlet state[1].

Other unresolved issues are related to the normal state properties in different doping regimes of the cuprate HTS materials. In the underdoped regime a pseudogap state exists with a gap like feature in the electronic density of states even at temperatures above the superconducting transition. At higher doping levels the normal state is more metal-like and appears to be rather well described by a Fermi liquid.

Despite the difficulties in formulating a microscopic theory a number of physical properties have been established since the discovery of the cuprate HTS. It is clear that the superconducting state is made up of Cooper pairs with the spin state being a singlet. It has also been clarified that the superconducting ground state is predominantly defined by a $d_{x^2-y^2}$ -wave symmetry of the order parameter (OP). The $d_{x^2-y^2}$ -wave OP has four lobes with alternating sign and nodes where the superconducting gap goes to zero.

Most of the studies of the complicated cuprates phase diagram[2] have used advanced spectroscopic tools such as ARPES (Angle Resolved Photoemission Spectra) and STM (Scanning Tunneling Microscopy) techniques on highly pure single crystals (in very few cases thin films). However for collective phenomena such as superconductivity a different degree of ordering is expected to occur near surfaces and interfaces, leading to an intrinsic dependence on the sample size. The preparation of HTS superconductors in a low-dimensional form, like nanodots, will enhance the underlying physics. Spectroscopic studies on low dimensional HTS superconductors will help to better understand the "parent" bulk material properties.

It is in this scientific scenario that this thesis work aims to give a contribution. The main goal is to get new insights into the role of quasiparticle excitations in HTS oxides which are fundamental for the understanding of the ground state. We will approach the problem from a completely different perspective. By pushing the nanotechnologies and material science applied to HTS oxides beyond the present state of art we have fabricated and measured nanoscale HTS devices in transport regimes never accessed earlier.

We have realized an all HTS Single Electron Transistor (SET) to study the excitation spectrum of an YBCO island at the nanoscale. We have achieved a regime where charging effects are dominating and we have used the HTS SET as a spectroscopic tool to reveal a fully gapped superconducting state. The question of the existence of a weak subdominant imaginary order parameter, which sums up with the predominant $d_{x^2-y^2}$, at low

temperatures, is still open. Experiments of thermal transport in Bi-Sr-Cu-O superconductors[3] for example, have revealed a number of anomalies, prompting the suggestions that a secondary superconducting order parameter is developed in an external magnetic field.

In this thesis work the *parity effect* in an all HTS SET is studied. In such a device the electrostatic energy required to add an odd number of excess quasiparticles to the island is higher than for an even number due to the presence of a condensate of Cooper pairs, and of a full energy gap in the excitation spectrum. This results in a parity dependent free energy F of the island.

A $d_{x^2-y^2}$ order parameter together with disorder and scattering effects results in a finite quasiparticle density of states even at zero energy[4]. In an SET this will make the two cases of even and odd number of excess quasiparticles on the island energetically equivalent, i.e. the even/odd free energy difference is equal to zero. Instead, we observe a finite parity dependent free energy, which is consistent with a complex order parameter of the type $d_{x^2-y^2} + is$ or $d_{x^2-y^2} + id_{xy}$ resulting in a fully gapped quasiparticle density of states.

A prerequisite to fabricate an all YBCO SET is the ability to define Josephson Junctions on the nanoscale with the proper parameters, such as normal resistance, capacitance and critical current. This is quite a challenging task and two technological paths based on biepitaxial grain boundaries have been assessed in this thesis. A conventional method, used frequently in the past, based on an amorphous carbon mask and ion milling and a new method based on the phase competition between superconducting YBCO and the insulating *green phase* at the grain boundary. The new method is developed to minimize the damage caused by the ion beam in the fabrication process. With these two approaches we have been able to cover a wide span of junction parameters which could allow the technology to also be used in other applications.

During the development and characterization of these two fabrication methods a natural opportunity also arose for a more fundamental study of the properties of the grain boundary. Voltage noise measurements were performed to determine the microscopic transport properties by comparing the data to theoretical models of the grain boundary interface described in literature.

Chapter 2

Introduction to superconductivity

2.1 Superconductivity

Superconductivity was discovered in 1911 when Kamerlingh Onnes observed a sharp drop in the electrical resistance of a solid mercury sample immersed in liquid helium. The transition to a state of zero resistance occurred at a *critical temperature*, T_C . Since then superconductivity has been found in a large number of metals and compounds. However, a microscopic theory explaining the superconductive phenomenon was formulated first in 1957 by Bardeen, Cooper and Schrieffer[5].

In this model, known as the BCS theory, electrons of opposite spin and momentum close to the Fermi surface pair up into *Cooper pairs* and form a condensate. This is possible due to a weak attractive force mediated by the electron-phonon interactions that allows the electrons to overcome the Coulomb repulsion when $T \leq T_C$. The pairs are spin singlets and behave as bosons occupying the same quantum state. The length scale of the pair interactions is determined by the *coherence length*, ξ . The BCS theory also predicts a gap, Δ , in the excitation spectrum of superconductors where 2Δ represents the energy needed to break a Cooper pair.

The superconducting condensate can be described by a wavefunction $\Psi(\mathbf{r}) = |\Psi(\mathbf{r})| e^{i\theta(\mathbf{r})}$, where $|\Psi(\mathbf{r})|^2$ gives the density of Cooper pairs and θ is the phase of the ground state. It is also referred to as an order parameter. The order parameter is proportional to Δ and for *Low critical Temperature Superconducting* (LTS) materials, described by the BCS theory, it is isotropic, i.e. with an *s*-wave symmetry.

A superconductor is also a perfect diamagnet. A magnetic field less

than a critical value, B_C , will be excluded from the bulk of a superconductor when it is cooled down below T_C . This effect is called *Meissner effect* and is due to screening currents flowing in a thin region at the surface of the superconductor. The field is screened completely in the bulk of the material penetrating only a short distance λ_L , known as the *London penetration depth*, from the surface of the superconductor.

2.2 Brief review of the basic properties of HTS

The history of superconductivity took a new turn in 1986 when the first High critical Temperature cuprate Superconductor (HTS) was discovered. A superconducting transition around 30 K was shown for the compound Ba-La-Cu-O[6]. In the following years a multitude of cuprate superconductors were discovered. The most studied one, Yttrium Barium Copper Oxide ($\text{YBa}_2\text{Cu}_3\text{O}_{7-\delta}$ or YBCO) has a T_C of 92 K[7].

This new class of superconductors has a basic structure which derives from the perovskite unit cell. A perovskite consists of 2 different cations (A and B) and 3 oxygen anions. The unit cell is a cube where the B cations are placed at the corners, the oxygen placed in the middle edge position and the A cation in the center of the cell[8]. The YBCO unit cell is made up of 3 perovskite cells stacked on top of each other with the A cation alternating between Ba, Y and Ba while the B cation is Cu for all cells (see figure 2.1).

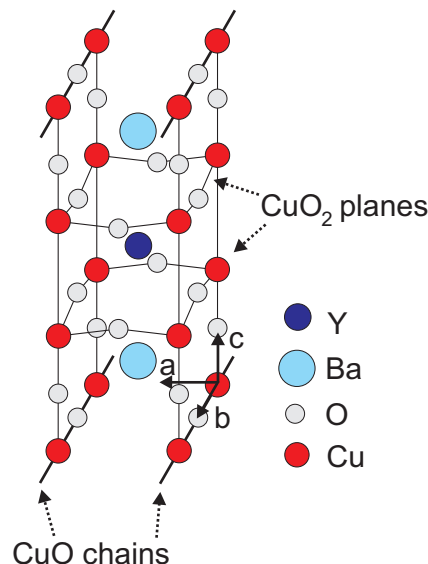


Figure 2.1: The unit cell of $\text{YBa}_2\text{Cu}_3\text{O}_7$.

2.2. BRIEF REVIEW OF THE BASIC PROPERTIES OF HTS

Strategic oxygen vacancies are also introduced, reducing the total oxygen number to the range 6-7[9]. The lattice parameters of the unit cell are $a \approx 3.88 \text{ \AA}$, $b \approx 3.82 \text{ \AA}$ and $c \approx 11.7 \text{ \AA}$ [10]. Two CuO_2 planes are positioned right above and below the Y ion (see figure 2.1). These CuO_2 planes are a common denominator for all HTS cuprates and are believed to play an important role in the formation of the superconducting state.

In the CuO planes delimiting the unit cell specific oxygen vacancies lead to the formation of CuO chains in the b -direction. Figure 2.1 shows a unit cell with 7 oxygen atoms. Adding or removing oxygen in the CuO chains will cause the number of available charge carriers in the material to change. This is addressed by using a chemical formula $\text{YBa}_2\text{Cu}_3\text{O}_{7-\delta}$ where δ is a measure of free "doping" of the material.

There are both electron and hole doped HTS cuprates, however YBCO is hole doped. The T_C vary with the oxygen content and for δ above ≈ 0.7 the material is no longer superconducting. Cuprate superconductors like YBCO exhibits a number of complex behaviors in different doping regions. The phase diagram is shown in figure 2.2 a).

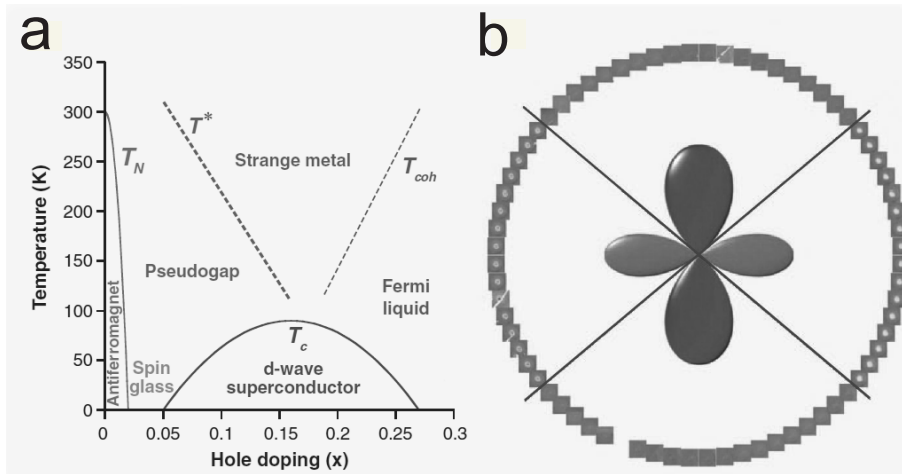


Figure 2.2: a) Schematic phase diagram for hole doped superconducting cuprates. The phases are shown as a function of hole doping per planar copper atom. b) The dominating d -wave order parameter with a subdominant s -wave, which results in asymmetric orthogonal lobes[19]. The figure is after [14].

For a very low oxygen content (δ close to 1) the YBCO enters an antiferromagnetic insulating phase with a tetragonal structure. For higher oxygen content, in the superconducting region and beyond, the unit cell

	a-b (nm)	c (nm)
λ_L	135	1000
ξ	1.6	0.24

Table 2.1: London penetration depth and coherence length for optimally doped YBCO[15][16].

has an orthorhombic structure. The normal state of YBCO, at temperatures above T_C , consists of a phase that has poor conductivity and an unusual and nonmetallic temperature dependence of the resistivity and the Hall coefficient[11]. This region is often referred to as a Non-fermi liquid or "weird metal" phase. For lower doping values (with respect to the optimal value, corresponding to the highest T_C) to the left of the T^* line in figure 2.2 a) YBCO in the normal state will undergo a transition into a Pseudogap region. In this phase, gap like features are present in the density of states (DOS). The microscopic mechanisms leading to the pseudogap are not clearly understood. It has been suggested both that it is connected to the onset of the superconducting state and that it might compete with superconductivity[12][13].

Due to the complex behavior when the doping is changed it is important to consider the possibility of out diffusion of oxygen when fabricating YBCO devices. Small dimension samples and excess heating are two known causes that may lead to underdoped films.

A consequence of the complex crystal structure of YBCO is that both the superconducting and normal metal properties are highly anisotropic. Table 2.1 summarizes the values of characteristic lengths in the a-b planes and along the c-axis direction.

The BCS theory developed more than 50 years ago has been successful in explaining the microscopic mechanisms leading to the superconductive phenomenon in conventional metals and compounds. However it does not apply to the cuprate superconductors whose microscopic mechanisms is still debated. One significant difference between the conventional LTS materials and most of HTS including YBCO is the symmetry of the order parameter. It has been shown that it is of the $d_{x^2-y^2}$ type instead of the isotropic s-wave symmetry of conventional superconductors. The $d_{x^2-y^2}$ order parameter can be expressed as[17][18]:

$$\Delta(\mathbf{k}) = \Delta_0[\cos(k_x a) - \cos(k_y a)] \quad (2.1)$$

This order parameter, also referred to as *d*-wave, is characterized by four

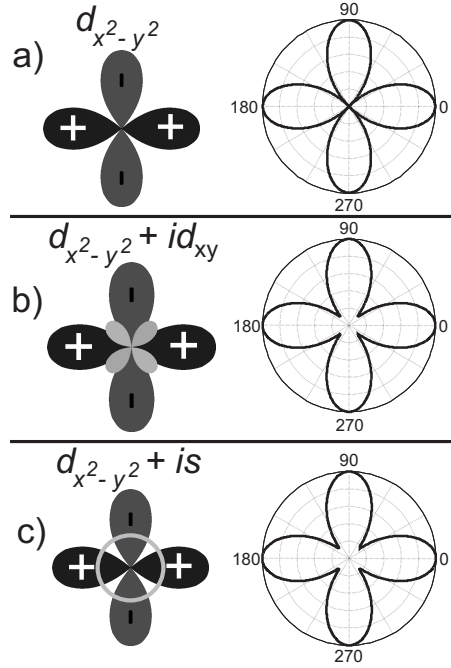


Figure 2.3: The left side shows, from the top, a sketch of pure d -wave, d -wave + id and d -wave+ is . The right side shows the absolute value of the three order parameters as a function of angle in k -space. Here $\epsilon = 0.25$.

lobes separated by nodes where the gap is suppressed, see figure 2.3 a). The phase of neighboring lobes changes sign. These properties have a number of important consequences for the transport mechanisms in these materials.

More recently it has been demonstrated that the symmetry of the order parameter is not purely $d_{x^2-y^2}$. There is also a subdominant s -wave order parameter which sum up to the dominant d -wave. This leads to an order parameter with asymmetric orthogonal lobes, but still with nodes[19], see figure 2.2 b). It is still an open question if subdominant s or d_{xy} , allowed by the orthorhombic structure of the YBCO, can be summed up to the dominant d -wave as imaginary terms. In the $d_{x^2-y^2} + id_{xy}$ case one would have[17][18]:

$$\Delta(\mathbf{k}) = \Delta_0[(1 - \epsilon)[\cos(k_x a) - \cos(k_y a)] + i\epsilon[2\sin(k_x a)\sin(k_y a)]] \quad (2.2)$$

and for $d_{x^2-y^2} + is_{xy}$ the expression for the complex order parameter would be:

$$\Delta(\mathbf{k}) = \Delta_0[i\epsilon + (1 - \epsilon)[\cos(k_x a) - \cos(k_y a)]] \quad (2.3)$$

Here ϵ gives the fraction of the imaginary component with respect to the dominating d -wave. Figure 2.3 b) and c) show a sketch and plot of $d_{x^2-y^2} + id_{xy}$ and $d_{x^2-y^2} + is$ respectively. The important difference, that a small imaginary component creates, is that a gap will open in the nodes establishing a "fully gaped" superconductor. Kirtley and coworkers[19] have determined that if an imaginary component exists, it is very small, 2.5% or less of the dominating $\Delta_{x^2-y^2}$.

Additional experiments that searched for a subdominant imaginary order parameter involved tunneling experiments[20][21][22], and thermal conductivity measurements[3]. The question is still open and one of the main goals of this thesis is to investigate if YBCO experience a transition to a fully gaped state at low temperatures.

Chapter 3

The Josephson effect

One of the most remarkable behavior of superconductors was theoretically predicted in 1962 by Brian D. Josephson[23]. It concerns the phenomenology of two superconductors that are weakly connected through for example, a thin insulating barrier, see figure 3.1 a). The current through the weak link is described by the equation for the d.c. Josephson effect:

$$I_S = I_C \sin\phi \quad (3.1)$$

Here $\phi (= \theta_1 - \theta_2)$ is the phase difference between the wavefunctions of the two bulk superconductors (see figure 3.1 b)) and I_C is the *critical current* which is the maximum supercurrent a Josephson junction can sustain without dissipation. I_C is inversely proportional to the normal resistance R_N and for conventional BCS superconductors the theoretical value is given by the Ambegaokar-Baratoff equation[24]:

$$I_C = \frac{\pi\Delta}{R_N 2e} \tanh(\Delta/2k_b T) \quad (3.2)$$

where T is the temperature. For low temperatures we have:

$$I_C \approx \frac{\pi\Delta}{R_N 2e} \quad (3.3)$$

The time evolution of the phase difference is given by:

$$\frac{d\phi}{dt} = \frac{2eV}{\hbar} \quad (3.4)$$

often referred to as the a.c. Josephson effect. It results in an oscillating supercurrent when a constant voltage (V) is applied[24].

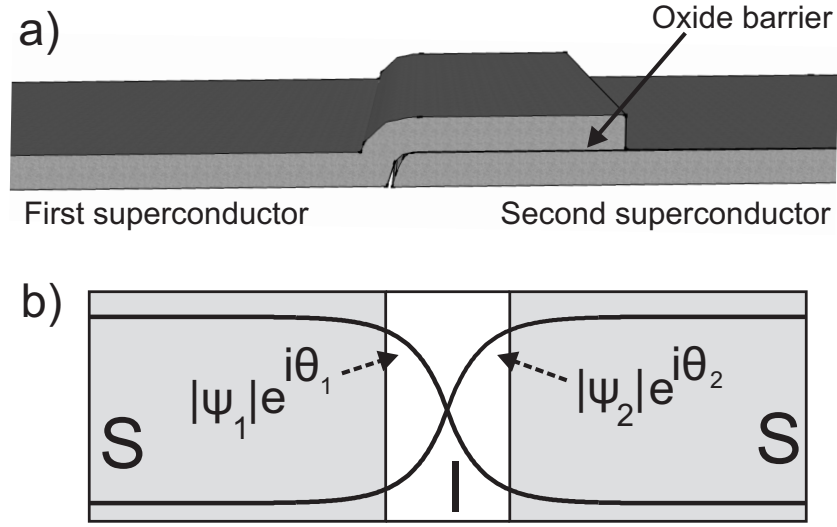


Figure 3.1: a) A possible realization of a Josephson junction with metal superconductors. b) A sketch of a Josephson junction showing the overlapping order parameter in the barrier.

Equation 3.1 is the simplest form of the d.c. Josephson effect including only the $\sin(\phi)$ term. A more general version also includes higher order terms:

$$I_S = \sum_{n=1}^{\infty} I_{C_n} \sin(n\phi) \quad (3.5)$$

For certain types of HTS Josephson junctions a second harmonic component has been detected in experiments[25].

3.1 The resistively and capacitively shunted junction model

A circuit equivalent for a Josephson junction is illustrated in figure 3.2. Here the Josephson junction is in parallel with a resistance R and capacitance C . This model is called the resistively and capacitively shunted junction (RCSJ) model.

From a circuit point of view a Josephson junction behaves as a non-linear inductor. This can easily be seen by differentiating the Josephson d.c. equation with respect to time[26]:

$$\frac{dI_S}{dt} = I_C \cos(\phi) \frac{d\phi}{dt} \quad (3.6)$$

3.1. THE RESISTIVELY AND CAPACITIVELY SHUNTED JUNCTION MODEL

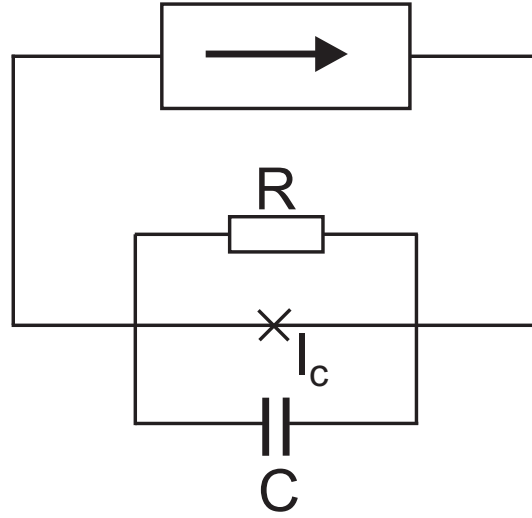


Figure 3.2: A sketch of the Josephson junction in the RCSJ model where the junction is shunted by a resistance and a capacitance.

Inserting equation 3.4 will give us:

$$V = \frac{\hbar}{2eI_C \cos(\phi)} \frac{dI_S}{dt} \quad (3.7)$$

From the right side term we directly get the *Josephson inductance*:

$$L_J = \frac{\hbar}{2eI_C \cos(\phi)} \quad (3.8)$$

By adding the current contributions of the three separate elements the equation for the circuit of figure 3.2 reads:

$$I = I_C \sin \phi + V/R + C \frac{dV}{dt} \quad (3.9)$$

By inserting equation 3.4 in 3.9 one gets a second order differential equation[24]:

$$I - I_C \sin \phi = \frac{\hbar}{2eR} \frac{d\phi}{dt} + \frac{C\hbar}{2e} \frac{d^2\phi}{dt^2} \quad (3.10)$$

To visualize the junction dynamics one can compare it to a mechanical analogue of a particle moving in a washboard potential given by:

$$U(\phi) = -E_J \cos(\phi) - \frac{\hbar I}{2e} \phi \quad (3.11)$$

where $E_J = \frac{\hbar}{2e} I_C$ is the *Josephson energy*. If we consider a bias current of $I=0$ the *phase particle* is trapped in a potential well and it oscillates at a frequency ω_p , called the *plasma frequency*, given by:

$$\omega_p = \frac{1}{\sqrt{L_J C}} \quad (3.12)$$

Another important parameter is the *quality factor* which is connected to the dissipation in the junction and defined by:

$$Q = \omega_p R C \quad (3.13)$$

The mechanical system will be governed by a differential equation similar to the Josephson junction. The position and velocity of the particle is given by ϕ and voltage ($V \sim \frac{d\phi}{dt}$) respectively. The particle has a mass of: $(\frac{\hbar}{2e})^2 C$ and is subjected to a viscous drag force: $(\frac{\hbar}{2e})^2 \frac{1}{R} \frac{d\phi}{dt}$. By using equations 3.8, 3.12 and 3.13 one can rewrite the differential equation (3.10):

$$\frac{I}{I_C} = \sin\phi + \frac{1}{Q} \frac{d\phi}{d\tau} + \frac{d^2\phi}{d\tau^2} \quad (3.14)$$

here we have introduced $\tau = \omega_p t$. A finite bias current will tilt the washboard, when $I < I_C$ the particle will stay still in a local minimum (if we neglect thermal and quantum fluctuations). A stationary phase particle represents a Josephson junction in the zero voltage superconducting state. When $I = I_C$ the tilt is high enough for the particle to escape and start sliding down the washboard. This corresponds to a Josephson junction that makes a transition to the non-zero voltage resistive state (known as the *running state*). Figure 3.3 show a sketch of the washboard potential at different values of I . In the running state the trajectory of the moving particle is connected to the dissipation of the junction. For a highly dissipative, low Q , the particle will follow the washboard closely. A high Q will instead result in a trajectory not following the shape of the potential, see the bottom part of figure 3.3. The resulting current voltage characteristics (IVC) of the junction will have different features according to the value of Q . Here we will assume a temperature low enough to neglect thermal fluctuations:

Case 1, $Q \ll 1$ A negligible small C will result in an *overdamped junction*. Equation 3.10 reduces to:

$$I - I_C \sin\phi = \frac{\hbar}{2eR} \frac{d\phi}{dt} \quad (3.15)$$

In the mechanical analogue this is equivalent to removing the inertia of the particle. This means that, while in the running state, by lowering the bias current below I_C the particle is immediately trapped in a local minima.

3.1. THE RESISTIVELY AND CAPACITIVELY SHUNTED JUNCTION MODEL

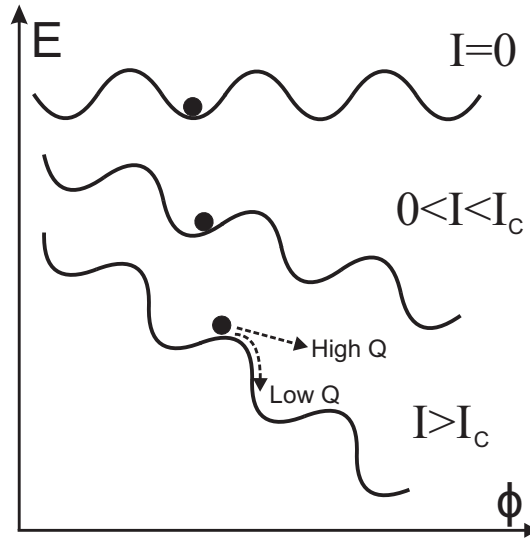


Figure 3.3: The RCSJ Washboard potential. In the top curve no bias current is applied and the particle is trapped in a potential minima. In the middle case a bias current less than I_C is applied and if thermal and quantum fluctuations are neglected the particle cannot escape. In the bottom curve the current is high enough for the particle to escape into the running state, the trajectory depends on the Q value.

Equation 3.15 has an analytical solution when integrated and the time averaged voltage is given by[27]:

$$V = R(I^2 - I_C^2)^{1/2} \quad (3.16)$$

The experimental IVC of an overdamped Josephson junction is plotted in Figure 3.4 a).

Case 2, $Q > 1$) For non negligible capacitances the junctions is in the *underdamped* regime and the IVC will be hysteretic, see figure 3.4 b). The initial switch to the finite voltage state still happen at $I = I_C$. The massive particle at the top of the barrier will immediately gain a high velocity since the trajectory does not follow the potential. This corresponds to an abrupt switch to the resistive state compared to the overdamped junctions. When the bias current is ramped down below I_C , the particle will due to its kinetic energy, not be retrapped in the washboard potential. A further decrease of the bias current will lead to the particle hitting the potential and getting trapped in a minima. When this happens the junction switches back to the superconducting state.

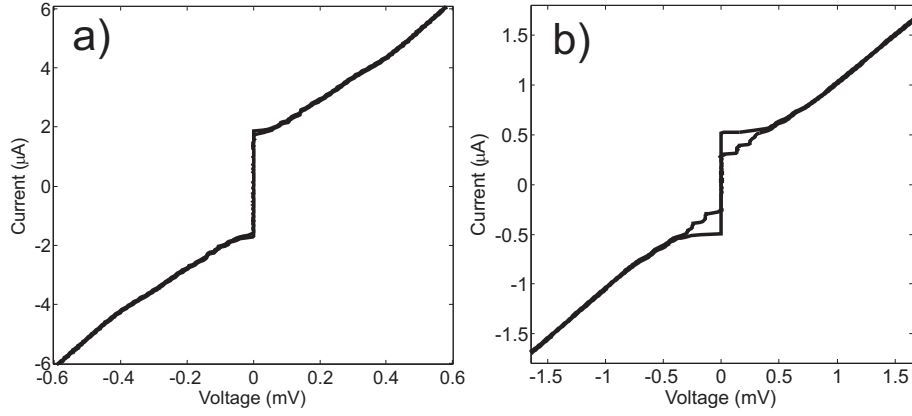


Figure 3.4: Example of an experimental a) Overdamped and b) Underdamped IVC.

The value of the bias current when the retrapping happens is given by[24]:

$$I_R \approx \frac{4I_C}{\pi Q} \quad (3.17)$$

At finite temperatures thermal fluctuations can allow the particle to overcome the barrier of the washboard potential before the threshold $I = I_C$ is reached (compared to the $T = 0$ case). After a premature escape the particle will start moving down the washboard and, for $Q > 1$, reach a high enough velocity that it does not retrap in another minima. This corresponds to the junction switching to the finite voltage state at a current lower than I_C .

3.2 Josephson junctions in magnetic field

We will now consider the effect of an external magnetic field on the Josephson current. In bulk superconductors the characteristic penetration depth of a magnetic field is the London penetration depth λ_L . The Josephson current in a junction will screen the magnetic field from the interior of the superconducting electrodes similarly to surface currents in a bulk superconductor. The field will only penetrate a length known as the *Josephson penetration depth* into the junction:

$$\lambda_J = \sqrt{\frac{\Phi_0}{2\pi J_C \mu_0 (2\lambda_L + d)}} \quad (3.18)$$

3.3. SUPERCONDUCTING QUANTUM INTERFERENCE DEVICE

Here $\Phi_0 = \frac{h}{2e}$ is the magnetic flux quantum, μ_0 the vacuum permeability, J_C the *critical current density* ($J_C = I_C / A_J$, where A_J is the total junction area) and d is the thickness of the barrier. λ_J determines the magnetic length of the junction and in this way influence the response of I_C to an external magnetic field. λ_J is important when compared to the junction width, w . If $w < \lambda_J$ we have the case of a *short junction* where both J_C and B are uniform. The supercurrent of a Josephson junction will modulate when an external magnetic field is applied due to the fields interaction with the phase. The phase change across the width of the junction when a perpendicular magnetic field, B , is applied is given by[28]:

$$\phi(x) = \frac{2\pi B(2\lambda_L + d)}{\Phi_0}x + \phi(0) \quad (3.19)$$

where $\phi(0)$ is a phase constant to be determined below. For a simple junction with a uniform supercurrent density the field dependence of the Josephson current can be derived by substituting equation 3.19 into the d.c. Josephson expression and first integrate along the width of the junction and then maximize with respect to $\phi(0)$, resulting in:

$$I_C(\Phi) = I_C(0) \left| \frac{\sin(\pi\Phi/\Phi_0)}{\pi\Phi/\Phi_0} \right| \quad (3.20)$$

Here $\Phi = B \cdot w \cdot (d + 2\lambda_L)$ is the magnetic flux through the junction. This relation is plotted in Figure 3.5. The pattern is comparable to that of light being diffracted by a single narrow slit and it is generally referred to as a Fraunhofer diffraction pattern. This analogy with optics will also be present in systems with multiple Josephson junctions.

3.3 Superconducting Quantum Interference Device

A Superconducting QUantum Interference Device (SQUID) consists of two Josephson junctions connected in parallel by a superconducting loop (see figure 3.6). To understand the behavior of a SQUID one can start by considering a superconducting ring without junctions. The total phase change along any closed path is given by the line integral[28]:

$$-\oint \nabla\theta \, d\mathbf{l} = \frac{2e}{\hbar} \oint \mathbf{A} \, d\mathbf{l} \quad (3.21)$$

where \mathbf{A} is the magnetic vector potential. The path is taken deep inside the ring where there are no screening currents. To keep the wave function single valued the integral of $\nabla\theta$ over the full path must be an integer multiple

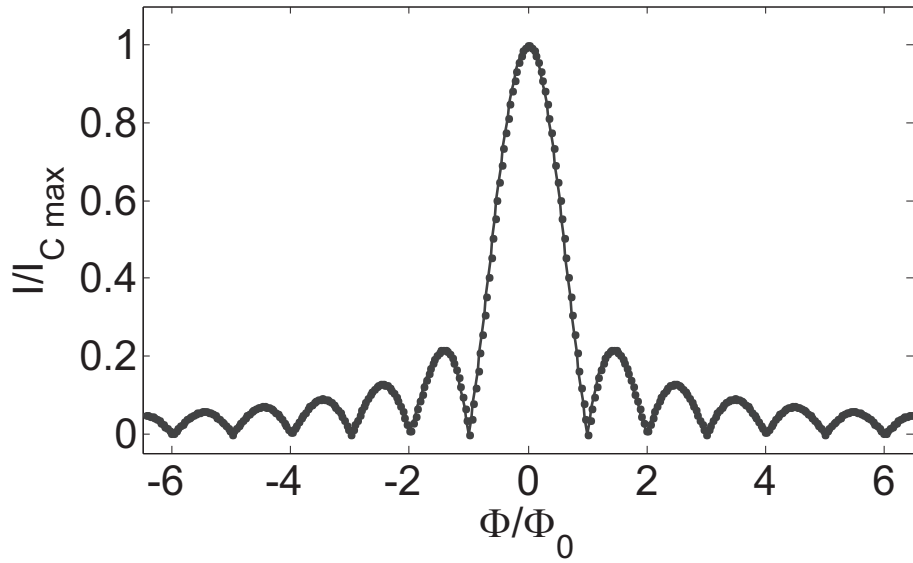


Figure 3.5: Critical current vs magnetic flux for a short Josephson junction with uniform current density.

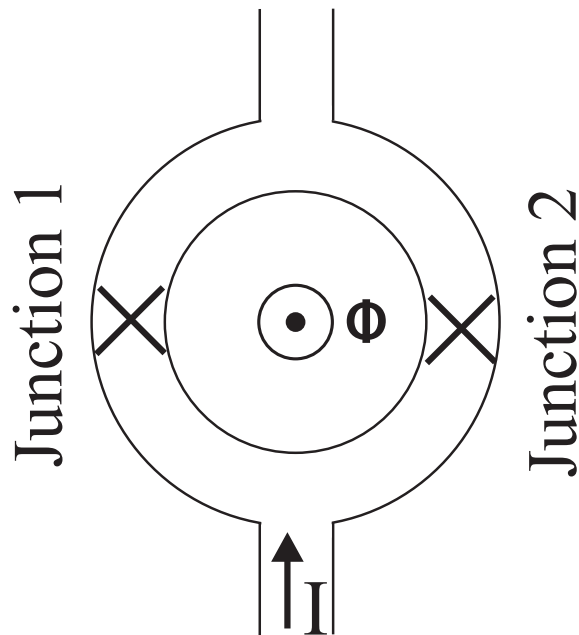


Figure 3.6: Sketch of a Superconducting QUantum Interference Device (SQUID).

3.3. SUPERCONDUCTING QUANTUM INTERFERENCE DEVICE

of 2π :

$$-2\pi n = \frac{2e}{\hbar} \oint \mathbf{A} d\mathbf{l} \quad (3.22)$$

Using Stokes theorem the right side term of equation 3.21 can be written as:

$$\frac{2e}{\hbar} \oint \mathbf{A} d\mathbf{l} = \frac{2e}{\hbar} \int_S \nabla \times \mathbf{A} dS \quad (3.23)$$

The curl of the vector potential is simply the definition of the magnetic field \mathbf{B} . The integral will consequently give the flux into the loop:

$$\frac{2e}{\hbar} \int_S \mathbf{B} dS = \frac{2e}{\hbar} \Phi = 2\pi \frac{\Phi}{\Phi_0} \quad (3.24)$$

Equation 3.21 therefore gives the flux quantization through a superconducting loop:

$$\Phi = n\Phi_0 \quad (3.25)$$

When two Josephson junctions are added to the ring in equation 3.21 one has to include the phase difference ϕ_1 and ϕ_2 across junction 1 and 2 respectively. This results in the following expression:

$$n2\pi - (\phi_1 - \phi_2) = 2\pi \frac{\Phi}{\Phi_0} \quad (3.26)$$

The total critical current of the SQUID will be the sum of the current contributions of the two junctions:

$$I_{SQUID} = I_{C1}\sin\phi_1 + I_{C2}\sin\phi_2 \quad (3.27)$$

To find the maximum I_{SQUID} at zero voltage one can use equation 3.26 to get:

$$I_{SQUID} = I_{C1}\sin\phi_1 + I_{C2}\sin\left(\phi_1 + 2\pi \frac{\Phi}{\Phi_0} - n2\pi\right) \quad (3.28)$$

and maximize this with respect to ϕ_1 . For junctions of equal critical currents and negligible self-inductance of the loop the expression for the I_{SQUID} dependence on magnetic flux is simply given by:

$$I_{SQUID} = 2I_C \left| \cos\left(\frac{\pi\Phi}{\Phi_0}\right) \right| \quad (3.29)$$

An example of this modulation pattern is plotted in Figure 3.7 a).

In the previous case the junctions forming the SQUID were point like. Since the work in this thesis involve SQUID's with submicron size loop area it is important to consider the scenario where the junctions do not have negligible dimensions compared to the SQUID loop (this case is commonly

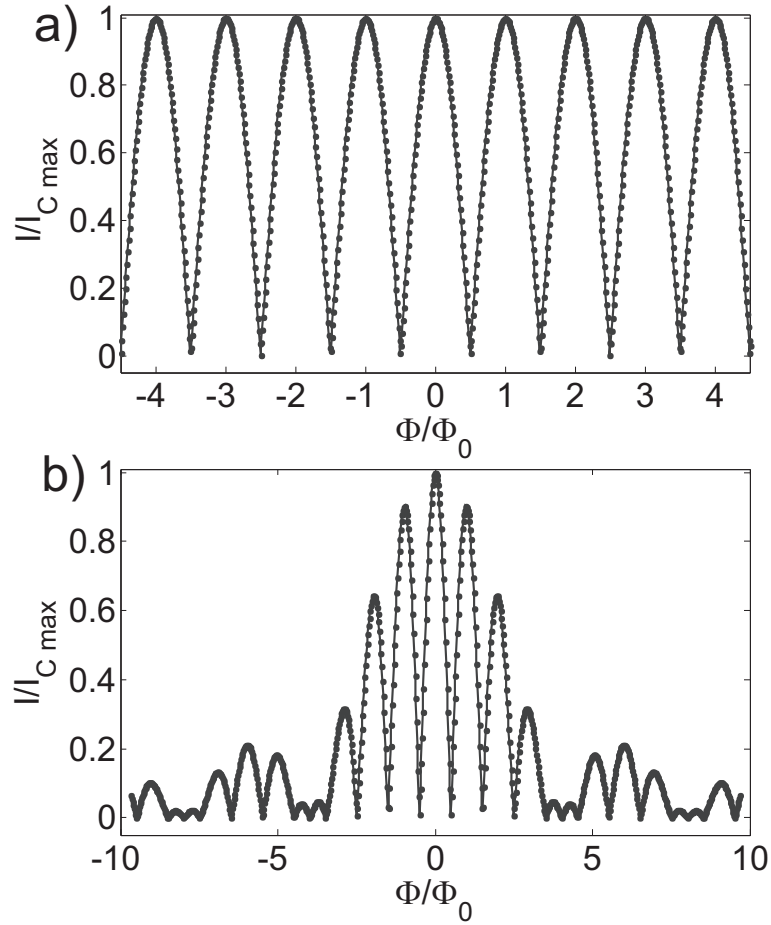


Figure 3.7: Critical current vs magnetic flux for a SQUID with negligible self-inductance and a) point like junctions b) distributed junctions ($\Phi_J/\Phi=0.25$).

referred to as a *distributed SQUID*). Here the total I_C vs Φ behavior will be the product of the SQUID and junction magnetic field patterns. This can be seen as a Fraunhofer pattern acting as an envelope on top of the SQUID modulations, described by[28]:

$$I_{SQUID} = 2I_C \left| \cos\left(\frac{\pi\Phi}{\Phi_0}\right) \frac{\sin(\pi\Phi_J/\Phi_0)}{\pi\Phi_J/\Phi_0} \right| \quad (3.30)$$

where Φ_J is the flux through the junctions. The ratio of SQUID and junction modulations is related to Φ_J/Φ . Figure 3.7 b) shows a modulation pattern of a SQUID where $\Phi_J/\Phi=0.25$.

3.4 N Josephson junctions in parallel

We now consider the case of N (>2) Josephson junctions connected in parallel. This will give rise to interference patterns more complex than for the SQUID. Figure 3.8 a) shows a sketch of an interferometer with 6 junctions in parallel. A structure with N Josephson junctions will in addition to the main modulation period Φ_0 have a quasi period, Φ_0/N , that becomes smaller when more junctions are added in parallel. At the same time the main maxima will be enhanced and sharper as N grows. The total critical current and its dependence on the flux is described by[29]:

$$I_{Ctot} = \sum_{n=1}^N I_{Cn} \sin\left(\phi_1 - \frac{2\pi(n-1)\Phi}{\Phi_0}\right) \quad (3.31)$$

Here it is assumed that the loops are of equal size and self-induced flux is neglected. As in the SQUID case described earlier this expression should be maximized with respect to ϕ_1 . If all the junctions have equal I_C it can be simplified to[30]:

$$I_{Ctot} = I_{C+} \left| \frac{1 - \cos\left(N\frac{2\pi\Phi}{\Phi_0}\right)}{1 - \cos\left(\frac{2\pi\Phi}{\Phi_0}\right)} \right|^{1/2} \quad (3.32)$$

where I_{C+} is the sum of the I_C of all the junctions in parallel. Figure 3.8 b) shows an I_{Ctot} vs Φ plot where the 6 parallel junctions have the same I_C . When asymmetries in the I_C of the junctions are introduced the pattern will become more complex. Figure 3.8 c) shows the case of dissimilar I_C .

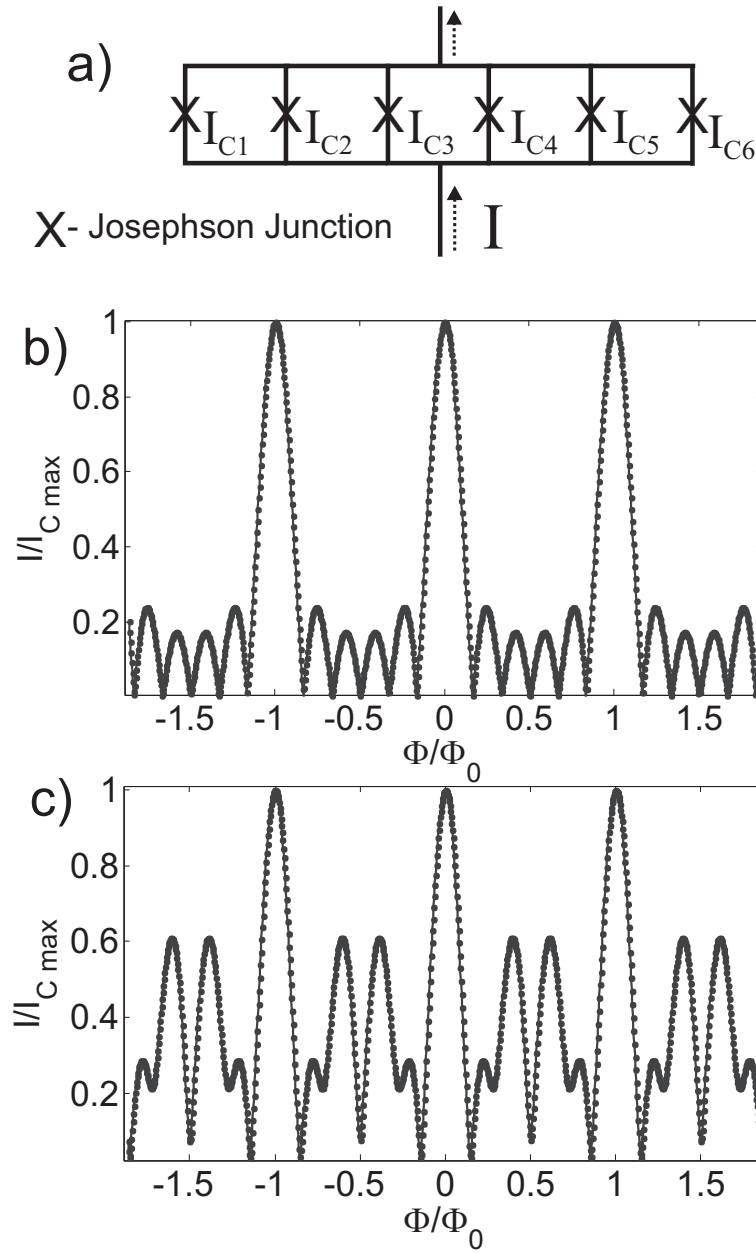


Figure 3.8: a) A sketch of a circuit containing 6 parallel Josephson junctions. b) Magnetic field pattern in the case where the critical currents of the junctions are equal and in c) when they differ according to $I_{C1} = 2$, $I_{C2} = 0.3$, $I_{C3} = 2.5$, $I_{C4} = 1$, $I_{C5} = 0.5$ and $I_{C6} = 3$ (arbitrary units, the currents are normalized to the maximum critical current, I_{Cmax}).

Chapter 4

Grain boundaries

The electrical transport of superconducting cuprate grain boundary Josephson junctions exhibit unconventional phenomenology not seen in their LTS counterpart. This chapter is dedicated to describing some common types of HTS grain boundaries, their structure and their transport mechanisms.

4.1 HTS Josephson Junctions

When the cuprate superconductors were discovered there was a great interest in realizing Josephson junctions. However, the fabrication methods had to take a different route compared with the fabrication methods of LTS. The cuprates need very high temperatures for good epitaxial growth ($\approx 700\text{-}800^\circ\text{C}$ for YBCO). This makes lift-off techniques not applicable due to the effect these high temperatures have on the resist layers. Moreover the chemical and structural instability of HTS's surfaces makes the conventional trilayer technique hard to implement. Instead of using an insulating layer as a barrier in HTS, structural defects interrupting the periodic lattice in epitaxial films, have been employed to create weak links. These defects can be created artificially at the border between regions with different crystallographic orientations and they are usually called Grain Boundaries (GB). The merging point between differently oriented grains can in certain conditions behave as a weak link showing Josephson properties. The GBs can be characterized by the mis-orientation angle α between the two grains and the direction of the axis of rotation: [100], [010] or [001]. For a rotation around an axis in the grain boundary plane we have a *tilt* junction and when the rotation is around an axis perpendicular to the grain boundary we have a *twist* junction. Figure 4.1 a) shows the 90° [010]-twist GB and figure 4.1 b) the 90° [100]-tilt case.

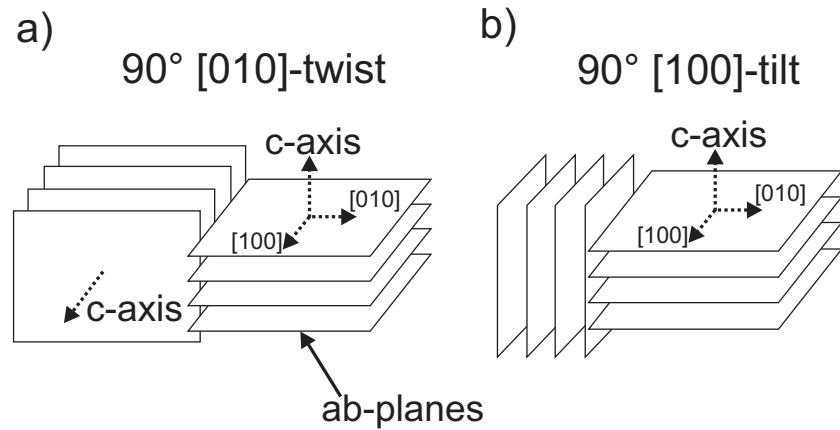


Figure 4.1: a) Shows a 90° [010]-twist GB and b) shows a 90° [100]-tilt GB.

The main methods to create artificial HTS GB junctions are the Bicrystal, Biepitaxial and Step edge technique.

4.1.1 Bicrystal junctions

The bicrystal type of GB is one of the simplest to fabricate but it requires a special type of substrate. This substrate is created by gluing together two pieces of the same material with different crystallographic orientation. When an epitaxial HTS film is deposited on this bicrystalline substrate the crystal axes of the film will follow those of the two substrates and a GB will be created at the boundary line, see figure 4.2. The bicrystalline technology tends to give rather reproducible junction properties at the expense of freedom in design. Indeed the junctions are confined at the bicrystal line and they can not be freely placed anywhere on the substrate.

4.1.2 Step-edge junctions

A step-edge junction is created by etching a step into a substrate and then growing a HTS film. If the angle of the step is $\geq 45^\circ$ for perovskite substrates like SrTiO_3 (STO) and LaAlO_3 the film grown on the slope of the step will have a different orientation compared to the film on the flat part of the substrate[31]. This causes the formation of two grain boundaries, one at the top of the step and one at the bottom, see figure 4.3. In the case of non-matched substrates (with respect to the crystallographic YBCO axis), like MgO , step angles of 10° can be enough to form GBs at the top and bottom part of the step. The two junctions in series are usually not desired, one

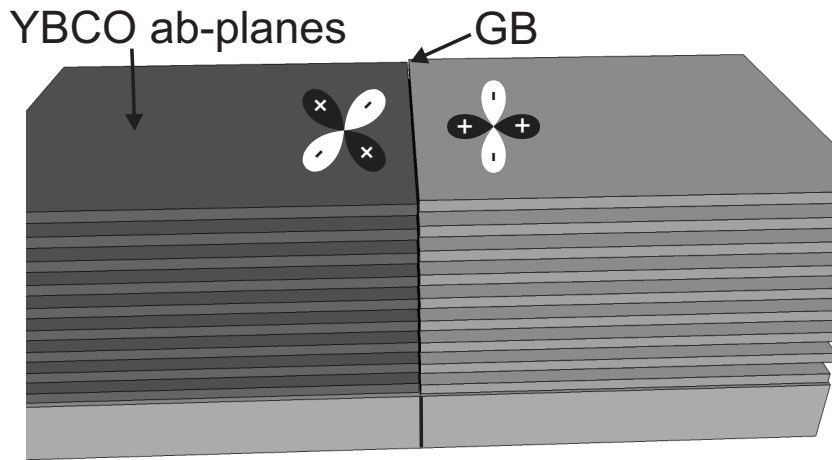


Figure 4.2: A $45^\circ[001]$ -tilt bicrystal grain boundary.

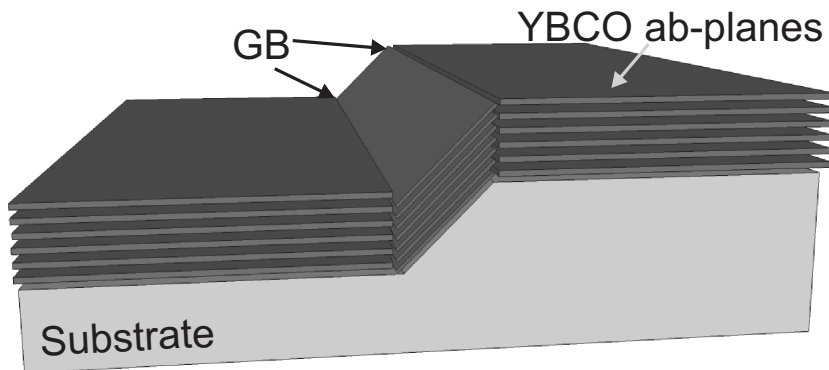


Figure 4.3: A sketch of a Step-edge sample.

can try to make them very dissimilar in critical current so the system will be dominated by the weakly coupled, low I_C , junction[32]. On MgO substrates a second approach is to eliminate one of the junctions completely by creating a smooth bottom step[33]. The step-edge technique allow one to freely place the junctions on the sample, but it also add the difficulty of properly defining the step profile which controls the structural properties of the GB and therefore strongly affects the transport properties of the junctions.

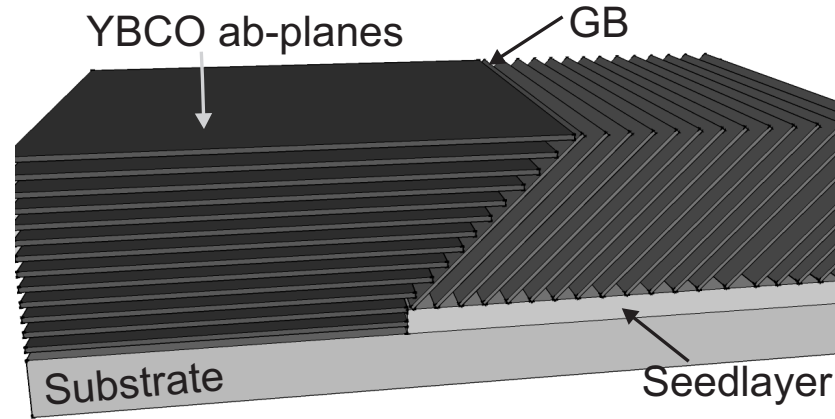


Figure 4.4: A 45° [010]-tilt biepitaxial grain boundary.

4.1.3 Biepitaxial junctions

The fundamental idea behind the biepitaxial technology is to epitaxially grow a *seed layer* on a crystalline substrate and then pattern it to only cover part of the substrate. The seed layer changes the epitaxial relation between the HTS film and the substrate. An example is shown in figure 4.4 where a seed layer of STO (110) is grown and then patterned on a MgO (110) substrate. In this way the YBCO film grows (103) oriented on the seed layer and (001) on the bare substrate. Just as for the bicrystal technique a GB will be formed at the boundary between the two growth directions. However the seed layer creates a step between the two films which is important to keep as small as possible. The depth of this step strongly affects the structural properties of the GB. Using the biepitaxial technique it is possible to place GBs freely on the substrate. Moreover by changing the orientation of the seed layer edge with respect to one of the in plane orientations of the substrate one can grow GBs with different structures and transport properties. All the samples in this thesis were fabricated using the biepitaxial technology; a detailed description is presented in chapter 6.

4.1.4 The $I_C R_N$ -product

A significant difference between LTS and HTS Josephson junctions is the behavior of the $I_C R_N$ -product. For an ideal LTS Superconductor-Insulator-Superconductor (SIS) tunnel junction with a *s*-wave order parameter this product is expected to follow the Ambegaokar-Baratoff relation (equation 3.2). For HTS GB's the $I_C R_N$ -product varies greatly but always being much

less than the Ambegaokar-Baratoff predictions; sometimes even one order of magnitude lower. A number of explanations have been suggested for this behavior including a suppression of the superconducting gap at the boundary, faceting of the interface and the anisotropy of the d -wave order parameter. In addition to this HTS GBs created by using some technologies (but not in all cases) have an $I_C R_N$ that scales with J_C :

$$I_C R_N \propto J_C^p \quad (4.1)$$

where a range of different p values have been reported ($p=0.3-0.6$ [34][35][36]).

4.2 The grain boundary interface

The structure and electrical properties of various GBs have been the subject of many studies over the last 2 decades. The properties of the interface layer depends on growth conditions and mis-orientation angle. Low angle GB's will consist of a combination of dislocations and lattice matched regions. As the angle is increased the dislocations will grow in number and eventually form a continuous layer[36]. The width of this dislocation layer varies for different types of grain boundaries. It has been estimated by Transmission Electron Microscopy (TEM) studies to be on the order of one nanometer [37][38].

The exact transport mechanisms of quasiparticles and Cooper pairs through the GB interface is still not completely understood. Several different models to describe the electrical transport through the GB have been proposed.

4.2.1 The filament model

The filament model proposed by Moeckly and coworkers[39] is based on an interface layer that consists of both a disordered superconducting region and a highly disordered non superconducting region, sandwiched between the bulk of the superconducting film, see figure 4.5. The narrow points, where the disordered superconducting regions from the two sides meet, will act as *filaments* that carry the supercurrent of the GB. In addition to the filaments there is also a parallel array of normal connections, which do not carry any supercurrent. The number of normal connections are generally assumed to be much higher than the number of superconducting filaments. The filaments are assumed to be randomly positioned in the GB and have widths in the range 1-60 nm.

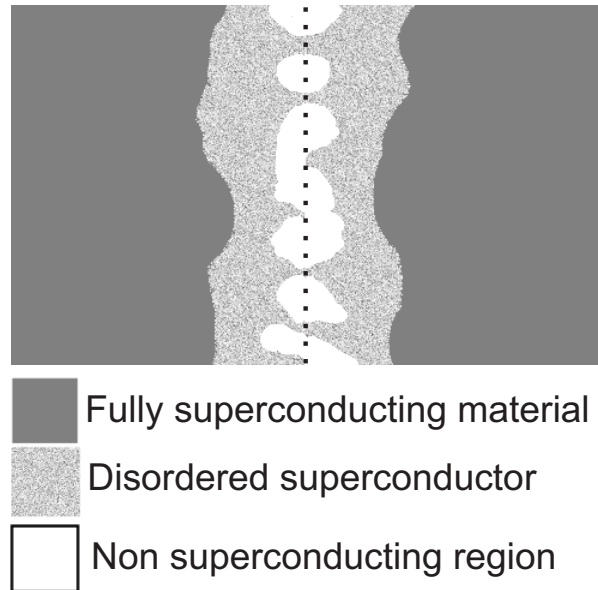


Figure 4.5: A sketch of the grain boundary region as described by the Filament Model.

4.2.2 The intrinsically shunted junction model

A second model that has been introduced (by Gross and Mayer[40]) to describe the transport through the GB and that has found some experimental support is the *intrinsically shunted junction* (ISJ) model[34][41][36]. The ISJ model assumes that the GB consists of an insulating layer that completely separates the two superconducting grains, and that possibly is sandwiched between thin layers of superconducting material with a reduced order parameter (SS'IS'S)[40]. Inside the insulating layer a large amount of localized defect states are found, see figure 4.6. Quasiparticle transport will be possible through resonant tunneling via these localized states. Because of Coulomb repulsion the Cooper pair transport will be restricted to direct tunneling through the insulating barrier[42].

4.2.3 Homogeneous barrier, SIS

Both the previous models assume a scenario where the GB is inhomogeneous and the normal and superconductive transport take place in different channels. In case of an ideal tunnel junction (SIS), both quasiparticles and Cooper pairs tunnel uniformly through the GB, again formed by an insulating barrier separating the two superconducting grains.

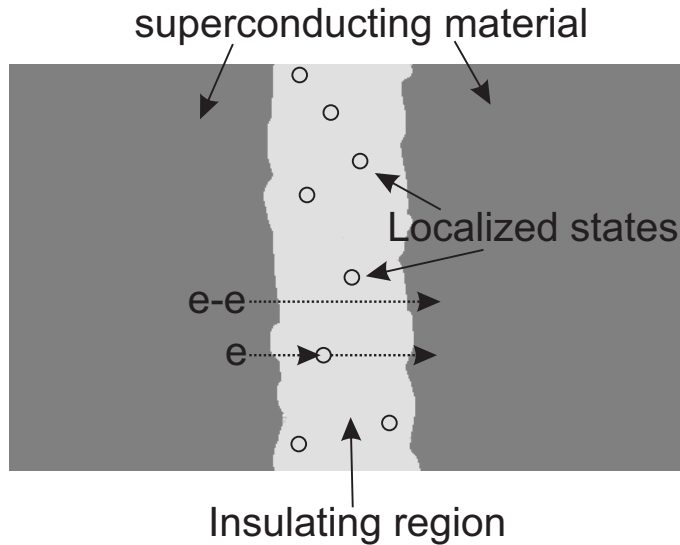


Figure 4.6: The grain boundary according to the intrinsically shunted junction (ISJ) model. Quasiparticles may traverse the barrier through resonant tunneling via the localized states while the Cooper pairs are restricted to direct tunneling.

4.2.4 The band-bending model

In this model proposed by Mannhart and Hilgenkamp[44][45][36] a thin insulating layer exist between the two grains due to structural disorder. Due to the Thomas-Fermi screening length (the length scale over which the electric field is screened by mobile carriers) being on the order of 1 nm for cuprates some effects similar to that of semiconducting materials can occur at the GB. Band bending at the interface can be severe enough to cause a depletion layer. The reduction in carrier density right next to the thin disordered layer will suppress the order parameter and result in an effective insulating layer larger than what is solely caused by the structural disorder. The band bending model does not exclude elements of the 3 previously discussed models that can contribute to build up the GB transport properties. Indeed from the multitude of experiments on GBs since the discovery of HTS it has not been conclusively shown that one of these models describes all types of junctions. It is instead well established that the transport properties strongly depend on the GB micro structure.

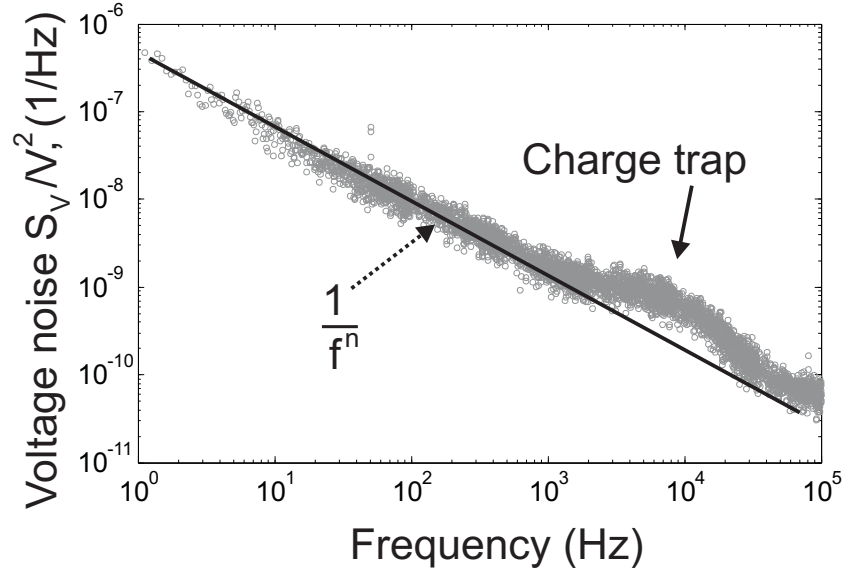


Figure 4.7: Voltage noise spectrum of a submicron grain boundary junction, here $n \approx 1$. The Lorentzian centered around 10 kHz is due to a 2-level charge trap.

4.3 Noise and the transport models for HTS GBs

To gain experimental insight into the structure of the GB barrier and its transport mechanism, one approach is to characterize the low frequency voltage noise at low temperatures. For HTS GBs the voltage fluctuations are made up of critical current fluctuations δI_C and normal resistance fluctuations δR_N . These two quantities are related to the transport mechanisms of cooper pairs and quasiparticles respectively. The noise spectra of HTS GB's will commonly have a predominant $1/f$ component, see figure 4.7 for an example from a biepitaxial YBCO GB.

For Metal-Insulator-Metal junctions it has been known for a long time that the $1/f$ component of the noise is due to 2-level charge trapping states in the barrier[46]. This was understood by noting that when the junction area was reduced to very small dimensions (comparable to the inverse areal density of fluctuators) the $1/f$ spectra started to decompose into a finite number of Lorentzian components. A Lorentzian is caused by a single charge trap that switches between an on (charge trap occupied by electron) and off (charge trap not occupied by electron) state, having mean lifetimes of τ_1 and τ_2 respectively.

It has been shown that this mechanism is likely also the cause for low

frequency $1/f$ noise in HTS GB junctions[43]. In figure 4.7 a weak Lorentzian feature centered around 10 kHz is superimposed onto the $1/f$ background. The frequency of the Lorentzian is given by $1/\tau_{eff}$ where $\tau_{eff} = (\tau_1^{-1} + \tau_2^{-1})^{-1}$ is the effective lifetime.

The trapping of a charge will locally increase the junction barrier making it less transparent. This is effectively the same as a decrease in the total junction area (A_J) by a value proportional to the cross-sectional area of the charge trap, A_t . Assuming that the transport through A_t is completely blocked when the fluctuator is switched on we have that $A_t/A_J = \Delta G/G$ [41] (where ΔG is the change in conductance). This can be used to get information regarding both the fluctuator's area and the Cooper pair/quasiparticle transport channel areas, as will be discussed in chapter 9.

For a current biased overdamped junction the voltage fluctuations, S_V , at a fixed current I depend on the relative root mean-square (rms) fluctuations $\delta I_C/I_C$ and $\delta R_N/R_N$ according to[49]:

$$S_V(f) = (V - R_d I)^2 S_i(f) + V^2 S_r(f) + k(V - R_d I) V S_{ir}(f), \quad (4.2)$$

Here $S_i = |\delta I_C/I_C|^2$, $S_r = |\delta R_N/R_N|^2$, and $S_{ir} = |\delta I_C/I_C| |\delta R_N/R_N|$ is the cross spectral density of the fluctuations and $R_d = \partial V/\partial I$ is the differential resistance. k is the correlation between the δI_C and δR_N . For $k = -2$ and $k = 2$ one has perfectly antiphase and inphase correlated fluctuations, respectively[49]. If $k = 0$ the fluctuations are uncorrelated. From equation 4.2 it is clear that when the differential resistance is very large the first term, containing S_i dominate the expression, this is the case when $I \approx I_C$. When the differential resistance approach the asymptotic normal resistance the second term, $V^2 S_r$, will instead give the main contribution (this is the case for bias currents significantly larger than I_C).

By fitting the measurement data to equation 4.2 one gains important insight into which of the different proposed GB models can describe the transport mechanism. The models give fundamentally different predictions for the ratio between S_i and S_r and for the correlation of the fluctuations.

A simplified version of the Filament model was treated by Miklich et al.[48] where the junction is assumed to consist of a small single superconducting channel in parallel to a large normal conducting channel. The area of the two channels are given by A_{qp} (quasiparticle transport) and A_{cp} (Cooper pair transport) and follow $A_{qp} \gg A_{cp}$. Due to the large difference in channel area, relative critical current fluctuations will be larger than the relative resistance fluctuations, resulting in $\sqrt{S_i/S_r} \approx \sqrt{N}$ (where

$N = A_{qp}/A_{cp}$). Due to the channels being independent from each other no correlation between δI_C and δR_N is predicted for this model ($k = 0$).

The ISJ model and the SIS Model on the other hand are expected to show an antiphase correlation, $k=-2$. This is due to the fact that both these models have an insulating layer that completely separates the two superconducting grains. If a charge trap switches to the on state, locally causing an increase of the junction barrier, I_C will decrease while R_N increases. The opposite is true when the trap switches off and the barrier is lowered[49].

The ratio $\sqrt{S_i/S_r} = q$ can be determined from the scaling behavior of the $I_C R_N$ product. The ISJ model predicts a scaling according to $I_C R_N \propto (J_C)^p$ [49]. From this it follows that $q = 1/(1 - p)$. Values of q in the range 2-4 have been reported in junctions following the ISJ model[34][41].

For an ideal SIS junction with a homogeneous insulating layer the Cooper pairs and quasiparticles will both tunnel directly through the same regions of the GB. The Ambegaokar-Baratoff (equation 3.2) relation is valid for tunnel junctions and give a constant $I_C R_N$ product, resulting in $q = 1$.

4.4 Effects of d -wave symmetry on GB

The d -wave symmetry of the orderparameter will further differentiate the cuprate grain boundary junctions from their LTS counterpart. For Josephson junctions made out of d -wave superconductors the orientation of the order parameter in respect to the interface line plays a significant role for the J_C value. A junction where the lobes of the two order parameters are oriented against each other will have a higher J_C than when a node is facing the GB line. It has been shown that the J_C of d -wave Josephson junction follows the relation[50]:

$$J_C = J_{C,max} [n_x^2 - n_y^2]_L [n_x^2 - n_y^2]_R \sin(\phi) \quad (4.3)$$

here n_x and n_y are the projections of the normal unit vector of the interface (\mathbf{n}) onto the crystallographic axes in the right and left electrodes respectively. More than an order of magnitude difference in J_C have been observed when comparing a junction with a node oriented interface (minimum) to a configuration that give the maximum value[47].

4.4.1 Faceting

An important feature of the GB interface of cuprate superconductors is its *meandering* structure, see figure 4.8. The GB interface consists of facets usually on the length scale of 100-200 nm, the size of which depends on the

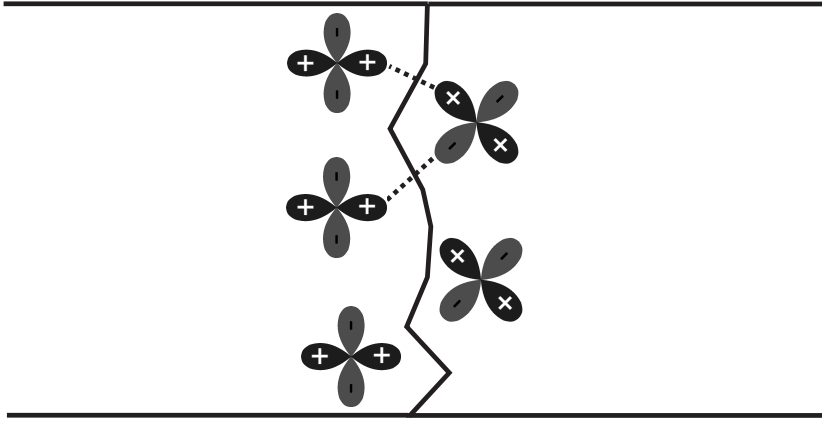


Figure 4.8: The faceting of a grain boundary interface will have a significant impact on the transport properties due to the d -wave order parameter in HTS.

growth conditions and the GB angle. The local GB angle will vary at each facet, making the nominally patterned GB angle an average angle. Due to the d -wave symmetry of the order parameter the meandering will have severe consequences for the electrical transport properties. Each facet will have its own J_C (depending on the GB angle in equation 4.3) and current phase relation. The facets will act as a parallel array and the transport through the GB will depend on this circumstance. This can cause deviations from an ideal I_C vs B patterns and a lower total J_C .

Two adjacent high angle facets may result in a configuration where there is transport both between two "-" lobes and a "+" and "-" lobe facing each other (see dashed lines in figure 4.8). One of these facets will have an extra phase shift of π compared to the phase difference of the other facet. This π -facet will carry a net negative current and decrease the overall J_C of the total GB structure.

Very small GBs may be made up of only a few facets, and when going to deep submicron dimensions only one facet per junctions might be achieved.

4.4.2 Andreev reflection

A charge carrier impinging on a Normal Superconducting (NS) interface may experience a so called *Andreev reflection*. We start by discussing the simplest scenario of an isotropic s -wave superconductor. An electron in the N-side arriving at the interface having an energy $E > \Delta$ will enter the

S-side into the quasiparticle states as an electron like excitation. However, for $E < \Delta$ there are no available states on the S-side and the electron may instead be reflected back as a hole having the same momentum but opposite direction. This reflection process cause the creation of a Cooper pair in the superconducting condensate on the S-side (see figure 4.9 a) for a sketch of the process).

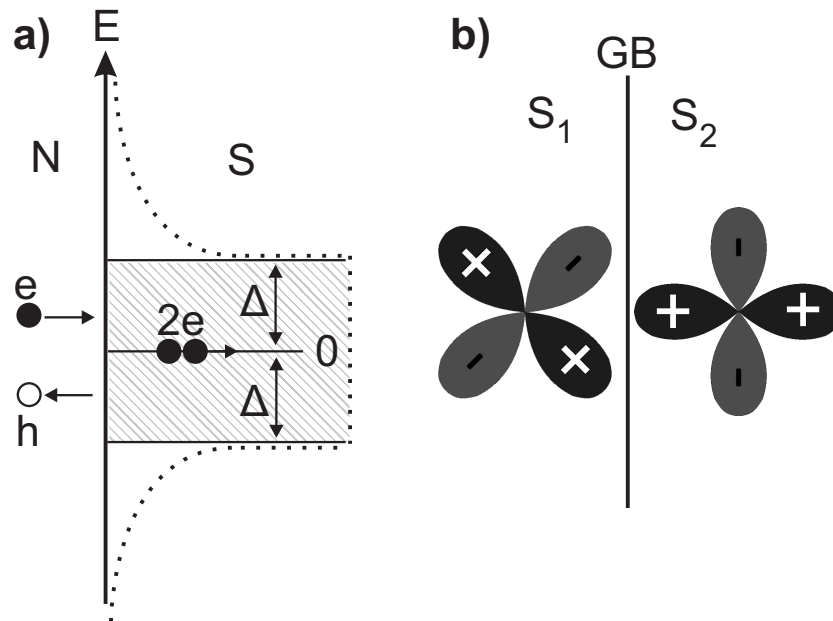


Figure 4.9: a) Andreev reflection in a NS interface for a s -wave superconductor. b) The sign change in the phase of the lobes of the d -wave order parameters results in zero-energy bound states at the interface between two HTS films.

For d -wave superconductors the picture get significantly more complex. Since the order parameter is anisotropic the orientation of the two electrodes in an HTS GB junction is important, see figure 4.9 b). Here the electrode on the left has the ab -planes rotated 45° with respect to the right one. The result is that the lobe of the order parameter on the right faces the node on the left side. The important difference with respect to the case of a s -wave order parameter is that the phase of the d -wave lobes changes sign. In the left electrode of figure 4.9 b) an incoming quasiparticle impinging the barrier at an angle of 45° will, once Andreev reflected, experience a phase change of π due to the d -wave symmetry[52][53]. Constructive interference between the incoming and reflected particles cause zero-energy

4.4. EFFECTS OF D-WAVE SYMMETRY ON GB

bound states (ZES) or midgap states (MGS) to be formed at the Fermi level. The MGS can be observed as a peak in conductance, centered around zero bias. The MGS are not just restricted to GBs like the one shown in figure 4.9 b), they have been observed in GBs with different angles because of the unavoidable faceting of the interface.

The study of MGS was of great interest in the early years of the cuprate superconductors and their observation has contributed to establishing the symmetry of the order parameter. Indeed their existence is due to a sign change of the phase of the order parameter between orthogonal orientations[51].

The MGS contribute to the Josephson properties of a GB junction. The theory is rather complex (for more details see for example [52]). The main results is that for certain grain boundary configurations the bound states present at the junction interface can give rise to a second harmonic component $I^{\text{II}}\sin 2\phi$ in the current-phase relation (CPR) whose amplitude I^{II} can be of the same order (or even higher) than the first component $I^{\text{I}}\sin\phi$. The amplitude of the 2nd order component decreases faster with increasing temperature than the amplitude of the 1st order component[52][54].

CHAPTER 4. GRAIN BOUNDARIES

Chapter 5

The single electron transistor

Tunnel junctions exhibit several interesting physical phenomena at low temperatures. In the previous chapter we have been focusing on the Josephson effect. In this chapter we will introduce another important physical mechanism that appear in junctions that are so small that the charge of single electrons starts to matter.

Consider a single junction with a small capacitance C connected to two electrodes. At low temperatures, the energy required for a single electron to tunnel through the junction, $E_C = e^2/2C$, called *charging energy*, becomes important. When a voltage smaller than $e/2C$ is applied to the junction it is energetically unfavorable for an electron to tunnel. This effect of zero current despite a non zero voltage is called *Coulomb blockade*. The two main requirements for this effect to be realized are:

1. The temperature must be low enough to prevent thermal fluctuations from smearing out the Coulomb blockade: $k_B T < E_C$.
2. The junction resistance must be higher than the quantum resistance, $R_Q = h/4e^2 \sim 6 \text{ k}\Omega$. This is required to prevent quantum fluctuations in the particle number to smear out the Coulomb blockade effects.

We will first consider junctions in the normal state and discuss the scenario of superconducting electrodes later in the chapter.

5.1 The single electron transistor

The observation of blockade effects in single junctions is difficult, even when the junction resistance is larger than R_Q . Indeed the resistance R_P seen by the junction capacitance, i.e. the parallel combination of the tunnel resistance R_T and the resistance (impedance) R_S of the biasing circuitry,

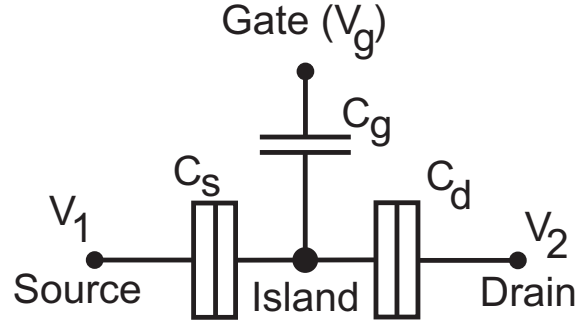


Figure 5.1: A sketch of a single electron transistor. The island is connected to the source and drain electrodes by tunneling junctions while the connection to the gate is purely capacitive.

must exceed the quantum resistance. The relevant time scale of transport through the junction is given by the “discharging time” of the junction capacitor $R_p C \sim 10^{-10}$ s[24], where C is the capacitance of the junction. At such high frequencies the biasing leads near the junction behave like transmission lines with impedance close to 100Ω [24]. This low impedance will prevent the observation of Coulomb blockade effects in a single junction unless special precautions are taken to create a high impedance environment around the junction[55].

The most straightforward way to study charging effects is instead through the *Single Electron Transistor* (SET). The SET consists of a mesoscopic island connected to two electrodes (Source and Drain) through tunnel junctions (having capacitances C_1 and C_2 respectively) and capacitively connected to a gate electrode (C_g), see Figure 5.1. As long as the two tunnel junctions fulfill the two requirements on capacitance (E_C is now given by $e^2/2C_\Sigma$ where $C_\Sigma = C_1 + C_2 + C_g$) and resistance the island will be sufficiently isolated from the electrodes and charging effects can be observed. The main feature of the SET is that the charge of the island can be controlled very accurately through the gate voltage, V_g . The amplitude of the Coulomb blockade is changed by the charge conditions on the island. To model the SET we need an expression for the total energy of the system. This consists of the electrostatic energy, U , and the work W_j done by the voltage when an electron tunnels through junction j . The electrostatic energy will depend on the applied voltage and the number of electrons, n , added to the island, according to[24]:

$$U = \frac{1}{2C_\Sigma} \left(\sum_{i=1,2,3} \sum_{k>i} C_i C_k (V_i - V_k)^2 + (ne)^2 \right) \quad (5.1)$$

5.1. THE SINGLE ELECTRON TRANSISTOR

where $e=1.60 \cdot 10^{-19}\text{C}$ is the electron charge and the index i runs over the two junctions and the gate, $C_3=C_g$. n is the number of *excess electrons* and it is not the total number of electrons on the island. W_j is given by[24]:

$$W_j = -e \sum_{i=1,2,3} (V_j - V_i) \frac{C_i}{C_\Sigma} \quad (5.2)$$

The total energy of the system is now:

$$\begin{aligned} E &= U + \sum_{j=1,2} n_j W_j \quad (5.3) \\ &= \frac{1}{2C_\Sigma} \left(\sum_{i=1,2,3} \sum_{k>i} C_i C_k (V_i - V_k)^2 + (ne)^2 - 2e \sum_{j=1,2} n_j \sum_{i=1,2,3} (V_j - V_i) C_i \right) \end{aligned}$$

where n_j is the number of electrons tunneling through junction j . To gain a basic understanding, of the effect the gate voltage has on the charge state on the island, we first look at the limit of zero source-drain voltage ($V_1=V_2=0$). The work, $n_j W_j$, will now have a unique value equal to $neV_g C_g / C_\Sigma$, independent on which junction the electron tunnels through. The equilibrium energy for this system is now obtained from equation 5.3:

$$E(n, V_g) = \frac{1}{2C_\Sigma} (C_g V_g + ne)^2 + \text{constant} = E_C (n_g + n)^2 \quad (5.4)$$

Here we have introduced the gate induced charge $n_g = C_g V_g / e$. The constant term ($\frac{1}{2C_\Sigma} (C_g V_g^2 (C_1 + C_2 - C_g))$) does not depend on n and can be omitted in this treatment. Equation 5.4 gives rise to a set of energy parabolas, one for each integer n value, see figure 5.2 a). When the gate voltage is changed, the system will follow the lowest available energy curve and change the charge number on the island when required to minimize the energy. When $n_g = k + \frac{1}{2}$, where k is an integer, there is a degeneracy between two neighboring charge states (n). At this gate voltage the Coulomb blockade is lifted and electrons can tunnel to and from the island giving rise to a current peak when an infinitesimal source-drain voltage (V_{SD}) is applied.

The next step is to understand the IV characteristics of the SET and its dependence on the the gate voltage. This is more complex than the oscillating Coulomb blockade at infinitesimal source-drain voltages.

To calculate the current for finite source-drain voltages we start by considering the change in the total system energy as an electron tunnels to ($n \rightarrow n + 1$) or from ($n \rightarrow n - 1$) the island through either of the two junctions. This is done by comparing U (equation 5.1) before and after the

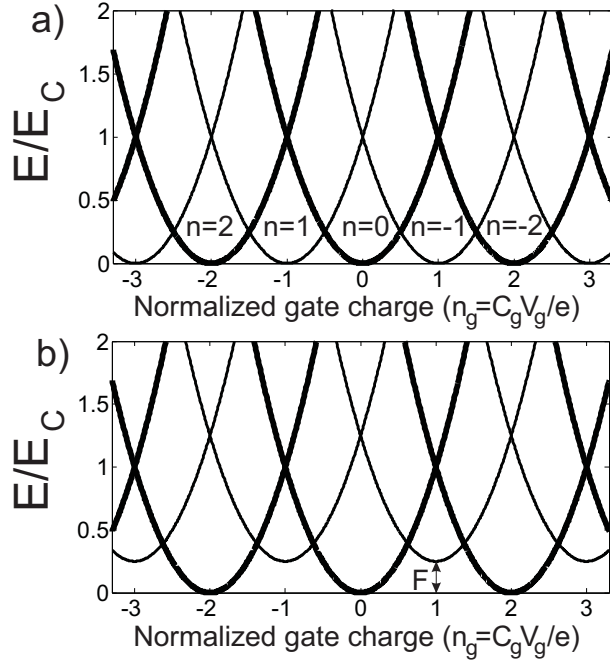


Figure 5.2: Energy parabolas for an SET with a) normal electrodes and island b) normal electrodes and superconducting island. Each curve is connected to a number of excess electrons, n , on the island. When two curves meet at $n_g = k + \frac{1}{2}$, where k is an integer, the blockade is lifted and the current will flow through the island.

change in n and adding the work W . We now put $V_1 = V_{SD}$ and $V_2 = 0$ and get the following expressions for the energy changes[56]:

$$\begin{aligned} \Delta E_1^\pm &= \frac{e^2}{C_\Sigma} \left(\left[\frac{1}{2} \pm (n + n_g) \right] \mp \frac{C_2 V_{SD}}{e} \right) \\ \Delta E_2^\pm &= \frac{e^2}{C_\Sigma} \left(\left[\frac{1}{2} \pm (n + n_g) \right] \pm \frac{C_1 V_{SD}}{e} \right) \end{aligned} \quad (5.5)$$

where ΔE_i^\pm is the energy change when an electron tunnels onto (+) or off (-) the island through junction i . A term containing $C_g \cdot V_{SD}$ has been dropped due to being very small for standard SET parameters. A current will only flow through the SET when the energy is decreased ($\Delta E_1^+, \Delta E_2^- < 0$ or $\Delta E_1^-, \Delta E_2^+ < 0$) for both tunneling onto and off the island. When this is not the case the Coulomb blockade is active and no current flow is allowed. By inspecting 5.5 it is clear that the blockade is a function of both V_g and V_{SD} . Setting $\Delta E = 0$ will define *voltage threshold* lines in the V_{SD}, V_g plane, which

define the onset of the current through the SET:

$$\begin{aligned}
 \text{Junction1} \quad V_{th}^{\pm}(n, n_g) &= \pm \frac{e}{C_2} \left(\frac{1}{2} \pm (n + n_g) \right) \\
 \text{Junction2} \quad V_{th}^{\pm}(n, n_g) &= \mp \frac{e}{C_1} \left(\frac{1}{2} \pm (n + n_g) \right)
 \end{aligned} \tag{5.6}$$

The current through the structure is given by [24]:

$$I(V) = e \sum_{n=-\infty}^{\infty} p(n) [\Gamma_1^-(n) - \Gamma_1^+(n)] = e \sum_{n=-\infty}^{\infty} p(n) [\Gamma_2^+(n) - \Gamma_2^-(n)] \tag{5.7}$$

where $p(n)$ is the probability density to have n electrons on the island and the sum over all values is normalized to 1. The tunneling rate through junction i is:

$$\Gamma_i^{\pm}(n) = \frac{1}{e} I \left(\frac{-\Delta E_i^{\pm}}{e} \right) \left(\frac{1}{1 - \exp(\Delta E_i^{\pm} / k_B T)} \right) \tag{5.8}$$

Here $I(\frac{-\Delta E_i^{\pm}}{e})$ represents the DC current due to an applied voltage. For a normal metal SET Ohm's law can be used: $I(V) = V/R_i$. If the island and/or the electrodes are superconducting this has to be replaced with the suitable formula for SIS or SIN tunneling.

The approach described here is usually called the Orthodox theory. To calculate the current as a function of V_g and V_{SD} for anything but special cases numerical calculations are needed. A basic stability diagram of a normal symmetric ($R_1=R_2$, $C_1=C_2$) SET is plotted in figure 5.3, here the source drain current, I_{SD} , is represented by the colorscale and plotted as a function of n_G and V_{SD} . The bright green rhombic region, commonly referred to as *Coulomb diamonds*, centered around zero V_{SD} represents the blockade regime, where no charge transfer through the transistor is allowed. The two upper insets show the IVCs for the open and closed (blockade) state, the gate position of these two curves are marked in the stability diagram with a blue and red line respectively. The right inset of figure 5.3 shows the source-drain current as a function of the gate charge, $I_{SD}(n_g)$, (*transfer function*) at fixed V_{SD} slightly above zero.

Figure 5.4 a) shows the same simulation as Figure 5.3 with the current replaced by conductance ($G = \partial I_{SD} / \partial V_{SD}$). By plotting the conductance, more structure will be revealed. Indeed several *higher order* diamonds are visible. The different diamonds can be understood as follows: In the blue central diamonds only a constant number of excess electrons are allowed on the island. This corresponds to the blockade regime where no charge

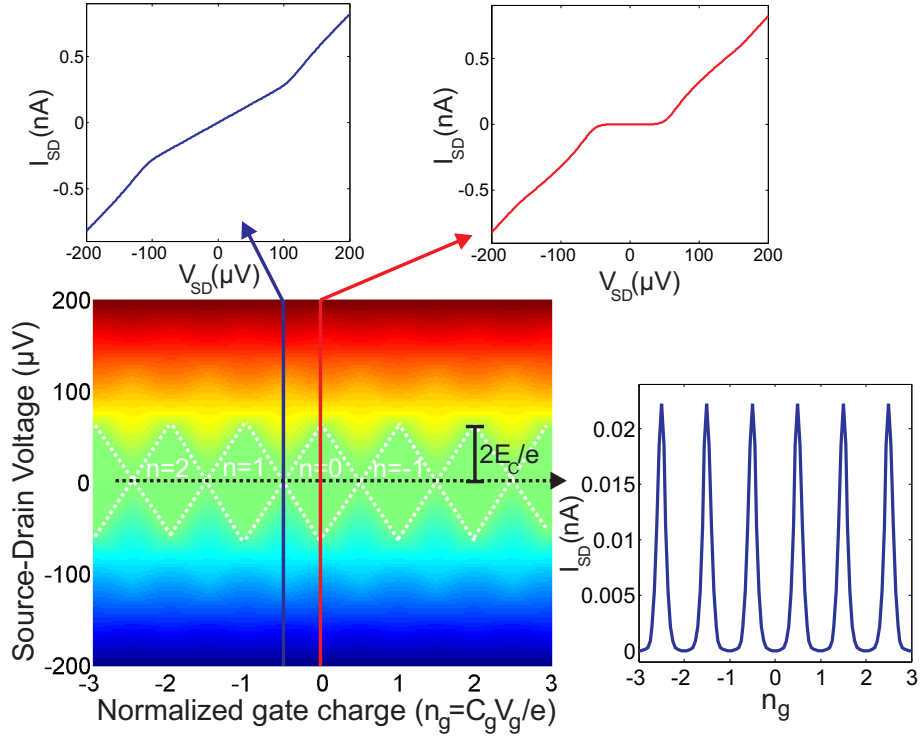


Figure 5.3: A simulated stability diagram of a normal metal SET. The color scale represents the source-drain current. The dashed white lines show the voltage thresholds. The inset to the right shows a transfer function at a V_{SD} slightly above zero. The two IVCs show the transistor in the open (blue) and closed (red) state respectively. The parameters used in the simulation were $R_1 = R_2 = 90 \text{ k}\Omega$, $C_1 = C_2 = 1.5 \text{ fF}$, $E_C = 27 \text{ }\mu\text{eV}$ and $T = 30 \text{ mK}$.

transfer through the island is allowed. For the cyan diamonds at higher V_{SD} the number of excess electrons on the island fluctuates over time between two values (differing by 1), giving rise to a finite current. The next red-yellow diamonds are described by a higher conductance due to three possible values of excess electrons on the island.

In the following section we will discuss the effects of junction asymmetry in an SET, both in resistance and capacitance, on the transport properties, i.e. the stability diagram. In Figure 5.4 b) - e) the simulated conductance $G(V_{SD}, n_g)$ of devices with asymmetric tunneling resistance ($R_1 \neq R_2$, $C_1 = C_2$) are shown, using asymmetry ratios: $R_1/R_2 = 1.5 - 4$. As the resistance asymmetry is increased the diamond structures for voltages above the Coulomb blockade are step by step changed into a slanted line of high

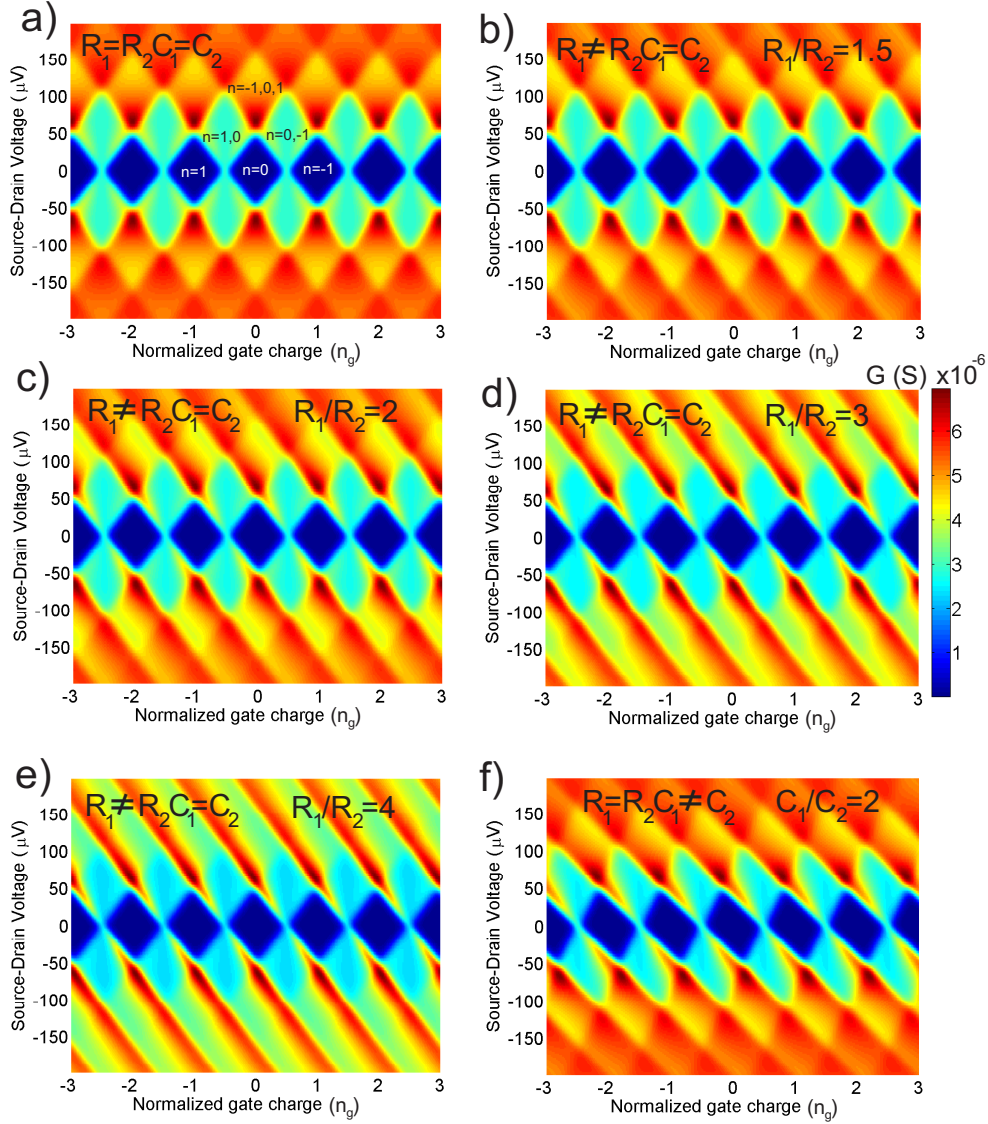


Figure 5.4: Simulated stability diagrams of a normal metal SET showing the conductance as a function of V_{SD} and n_g . a) Here the fully symmetric case, $R_1=R_2$, $C_1=C_2$, is shown. b) to e) show stability diagrams simulated for increasing resistance asymmetry while f) shows the case of symmetric resistance and asymmetric capacitance.

conductance. Already at $R_1/R_2 = 3$ the higher order diamonds are almost completely gone and replaced by a set of parallel lines.

For asymmetric junction capacitance ($R_1=R_2, C_1 \neq C_2$) much of the original diamond structure is maintained, however the pattern will be slanted in a direction that depends on the two junction capacitances, see figure 5.4 f). The slope of the two lines (only one for SETs asymmetric in R) that make up the diamonds can be used together with the gate capacitance to estimate the junction capacitances from SET measurement data.

5.2 Superconducting SET

The realization of an SET with some or all components made out of a superconducting material will add several new and interesting features to the transport phenomenology. The superconducting gap can, under certain conditions, modify the periodicity of the Coulomb blockade, effectively doubling it; this is referred to as the *parity effect*. In an SET with a superconducting island and normal electrodes it is possible to observe this effect. This so called NISIN SET will be discussed in the following section. The fully superconductive case, the SISIS SET, will briefly be addressed in the end of the chapter.

5.2.1 The NISIN SET

When the island is superconducting the gap, Δ , introduces another energy scale into the SET. The energy cost to add an electron to the island will depend on the parity of the system. If the tunnel event leads to an odd number n on the island the quasiparticle will be put at the first available state above the energy gap. Whereas if the number is even the quasiparticle can recombine to the condensate.

In experiments on parity effect in aluminum SETs Averin et.al.[57] and Tuominen et. al.[58] introduced the free energy difference, F , between the even and odd state. The observation of parity effect have thus far been limited to aluminum. In experiments using niobium SETs the even odd energy have not been detected[66][67].

Figure 5.2 b) shows an energy diagram where F is included. The odd parabolas have been displaced by a value F to higher energies. This causes the periodicity of the Coulomb oscillations of the SET to change from e to $2e$. At $T=0$ K F is equal to Δ , with increasing temperature F decreases and reaches zero at a transition temperature, T^* . The dependence of F on T is close to linear for all but temperatures close to T^* and can be approximated

with[59]:

$$F \approx \Delta - k_B T \ln(N_{eff}). \quad (5.9)$$

Here N_{eff} is the effective number of available states for quasiparticle excitations in a region $k_B T$ above Δ . The transition temperature is now approximately given by $T^* \approx \Delta / (\ln(N_{eff})k_B)$.

To add the effects of a superconducting island to the stability diagram, one needs to include F in the energy difference equation 5.5. If the tunneling event results in an odd n the energy cost of the event is increased and F should be added. If the end result is instead an even n , F should be subtracted, resulting in:

$$\begin{aligned} \Delta E_1^\pm &= \frac{e^2}{C_\Sigma} \left(\left[\frac{1}{2} \pm (n + n_g) \right] \mp \frac{C_2 V_{SD}}{e} \right) + (-1)^n F \\ \Delta E_2^\pm &= \frac{e^2}{C_\Sigma} \left(\left[\frac{1}{2} \pm (n + n_g) \right] \pm \frac{C_1 V_{SD}}{e} \right) + (-1)^n F \end{aligned} \quad (5.10)$$

In this treatment we will only consider single quasiparticle sequential tunneling.

The second modification for an SET with a superconducting island is that the ohmic $I(V)$ expression in the tunneling rate equation (5.8) need to be replaced. A general expression for the tunneling current is given by[28]:

$$I(V) = \frac{1}{R_i e} \int_{-\infty}^{\infty} \frac{N_1(\epsilon - eV)}{N_{n1}(0)} \frac{N_2(\epsilon)}{N_{n2}(0)} [f(\epsilon - eV) - f(\epsilon)] d\epsilon \quad (5.11)$$

where $f(\epsilon)$ is the Fermi function and N_j/N_{nj} is the density of states (DOS) for electrode j divided by the normal state DOS (N_{nj}). For a small bias range N_{nj} is effectively constant and therefore $N_1(\epsilon)/N_{n1}(0)=1$ in the normal metal electrode. If we consider a BCS superconductor for the other electrode, having an isotropic s-wave gap, the DOS is given by:

$$\frac{N_2(\epsilon)}{N_{n2}(0)} = \begin{cases} \frac{\epsilon}{\sqrt{\epsilon^2 - \Delta^2}} & |\epsilon| \geq \Delta \\ 0 & |\epsilon| < \Delta \end{cases} \quad (5.12)$$

The resulting SIN tunneling current is now:

$$I(V) = \frac{1}{R_i e} \int_{-\infty}^{\infty} \frac{\epsilon}{\sqrt{\epsilon^2 - \Delta^2}} [f(\epsilon - eV) - f(\epsilon)] d\epsilon. \quad (5.13)$$

Here the range $|\epsilon| < \Delta$ is excluded from the integration. The threshold voltages for an SET with a superconducting island are found by first setting $\Delta E = 0$ in equation 5.10. Since we are dealing with SIN junctions a charge carrier that tunnels also need to overcome Δ , which will increase the voltage

needed to drive a current through the SET. This addition is independent of n_g and n therefore Δ can simply be added[60]. This results in the following expression for the threshold voltages for $n \rightarrow n \pm 1$ transitions:

$$\begin{aligned} \text{Junction1 } V_{th}^{\pm}(n, n_g) &= \pm \left(\frac{e}{C_2} \left(\frac{1}{2} \pm (n + n_g) \right) + \frac{C_{\Sigma}}{eC_2} (\Delta + (-1)^n F) \right) \\ \text{Junction2 } V_{th}^{\pm}(n, n_g) &= \mp \left(\frac{e}{C_1} \left(\frac{1}{2} \pm (n + n_g) \right) + \frac{C_{\Sigma}}{eC_1} (\Delta + (-1)^n F) \right) \end{aligned} \quad (5.14)$$

This expression will be useful later when we need to extract F and C from our measurement data.

A simulated stability diagram for finite F and Δ is shown in figure 5.5, the voltage threshold lines are also indicated. There are two important differences compared to the case of the normal conducting SET. Due to the inclusion of SIN junctions, tunneling currents up to a source-drain voltage of $2\Delta/e$ are suppressed. The two IVCs shows that even when the SET is in the open state there is still a region of suppressed current for low voltages.

The second difference is that the presence of the even/odd energy F will make the diamonds either larger or smaller depending on if they represent an island with even or odd n . Consequently the current peaks shown in the transfer function to the right in figure 5.5 will no longer be equidistant, and the periodicity is now $2e$ rather than e as for the case of a normal island. The change in position between two sequential peaks can be used to calculate F .

5.2.2 The SISIS SET

For completeness this section contains a short discussion on a few features of the transport through a SISIS SET. In particular I will point out some of the processes which might be relevant for our experiment.

Here we consider an SET where both the island and the electrodes are superconducting (the SISIS case). In this case due to Cooper pair tunneling additional features appears in the IVC compared to the NISIN case. In the following we will discuss how the ratio between the Josephson Energy and E_C will affect the IVC of the SISIS SET.

When $E_J \gg E_C$ the Josephson effect will dominate and there will be a supercurrent, independent of the gate voltage, flowing though the SET. Lowering the Josephson energy to the region $E_C \approx E_J$ the supercurrent can be modulated by the gate voltage[24].

When E_J is much smaller than E_C the critical current will be suppressed and the device will be dominated by the Coulomb blockade. In this case

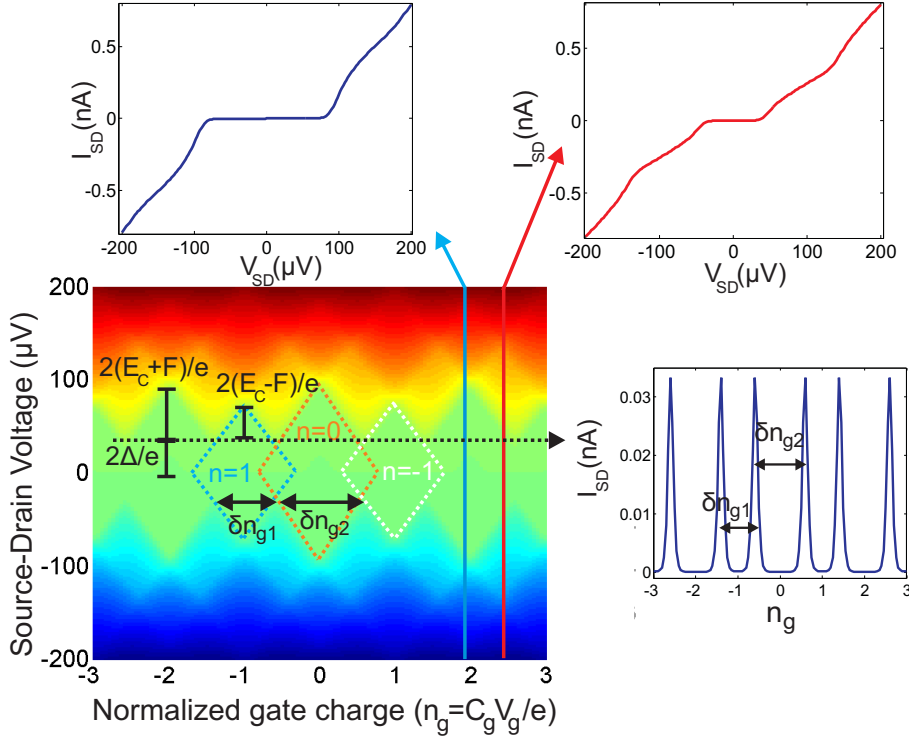


Figure 5.5: A simulated stability diagram of a NISIN SET. The color scale represents the source-drain current. The inset to the right shows a transfer function at a $V_{SD} \approx 2\Delta/e$. The two IVCs shows the transistor in the closed (blue) and open (red) state respectively. The parameters used in the simulation was $R_1 = R_2 = 90 \text{ k}\Omega$, $C_1 = C_2 = 1.5 \text{ fF}$, $E_C = 27 \text{ }\mu\text{eV}$, $T = 30 \text{ mK}$, $\Delta = 15 \text{ }\mu\text{eV}$ and $F = 5 \text{ }\mu\text{eV}$.

the IVC shows some similarities to the NISIN case. However the single electron tunneling blockade region around zero source-drain voltage will be expanded by $4\Delta/e$ instead of $2\Delta/e$ and modulate in the V_{SD} range $4\Delta/e$ to $(4\Delta + 2E_C + 2F)/e$ [60].

A significant difference from the NISIN case is that inside the gap region there are different tunneling cycles that can show up and give a sharp increase in current. The Josephson Quasiparticle cycle (JQP) is a resonant tunneling process where a Cooper pair tunnels through the first junction and two quasiparticles tunnel through the second[61][58]. The JQP peak will start to appear for bias voltages larger than $(2\Delta + E_C)/e$. The double JQP (DJQP) process involves the resonant tunneling of a Cooper pair at the first junction and a quasiparticle through the second. This is followed by

the resonant tunneling of a Cooper pair at the second junction followed by a quasiparticle tunneling through the first[62]. The DJQP cycle results in a current peak at a bias voltage of $2E_C/e$. Both these two tunneling cycles have a gate voltage dependence, see figure 5.6.

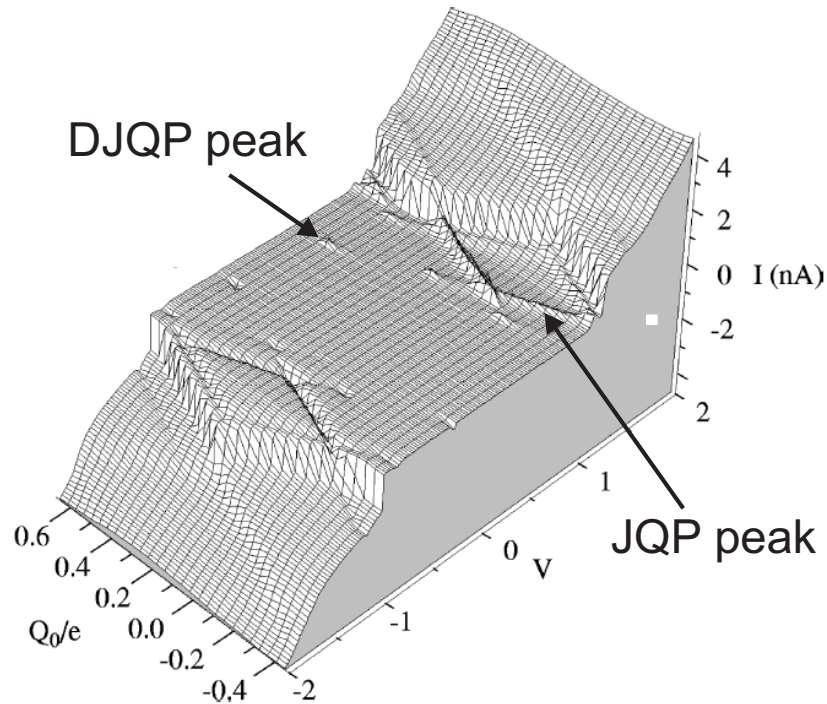


Figure 5.6: IVCs as a function of gate charge for an SISIS SET, adapted from [60]

Another effect to consider is transport due to Andreev reflection. This has been observed both in NISIN[63], [64] and SISIS[60] SETs. First an electron is Andreev reflected into a hole at junction nr 1. This creates a Cooper pair on the island. In the second step a hole is reflected into an electron at junction nr 2 and the Cooper pair in the island is destroyed. The effect of these two steps is the transfer of $2e$ through the SET. This type of transport may have a $2e$ periodicity with respect to the gate voltage and is not suppressed for V_{SD} values below $2\Delta/e$ ($4\Delta/e$ for SISIS) as in the case of sequential quasiparticle tunneling. For a NISIN SET a blockade region, centered at zero V_{SD} , exists for the Andreev current which will modulate between 0 and $2E_C/e$ as the gate voltage is changed[64]. The Andreev cur-

rent is strongly suppressed for low transmission barriers making it difficult to observe for high resistance junctions[65].

It is interesting to note that the parity effect observed in aluminum SETs in past experiments have always involved a transport process that include Cooper pair tunneling and/or Andreev reflection. These processes are always confined to the the V_{SD} region below $4\Delta/e$ for SISIS SETs and $2\Delta/e$ for NISIN SETs.

Chapter 6

Fabrication of grain boundary junctions

One of the aims of this thesis is to study the properties of deep submicron grain boundary junctions and devices made by these junctions. To fabricate HTS junctions on the nanoscale, that retain their superconducting properties, through all the nanofabrication procedures is a rather complicated task. Here we will describe two different approaches.

The artificial grain boundaries are created using the biepitaxial technique. The motivation for this is the freedom the technique give us in designing any combination of junction angle and position on the same sample.

6.1 The choice of substrate

In the past years a significant amount of work has been done on biepitaxial YBCO junctions fabricated on SrTiO_3 (110) substrates using CeO_2 (110) as seed layer[47][68][69]. However, in these works the large dielectric constant 277[70] of the SrTiO_3 (which increase to about 20000 at sub Kelvin temperatures[71] for single crystals) is a serious limitation for microwave applications and for the design of devices where charging effects are relevant (because of the large stray capacitance of the substrate in parallel with the junction). For our experiments Magnesium oxide (MgO) was chosen as a substrate material. It has a dielectric constant of 9.65 [70]. We have chosen a thin film of SrTiO_3 as seedlayer. The dielectric constant of a thin film is much smaller than that of a single crystal.

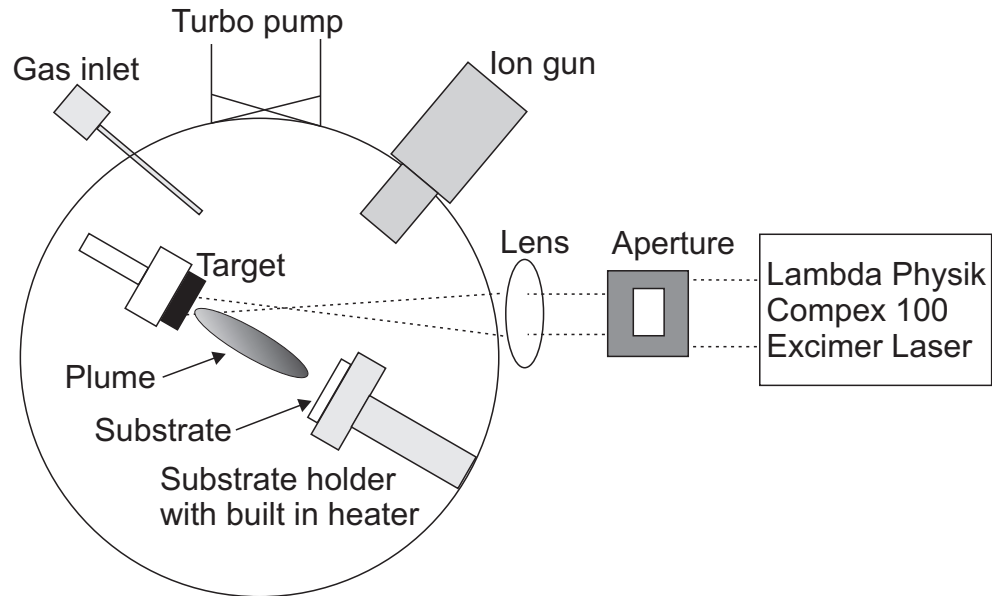


Figure 6.1: A sketch of the PLD system used in this thesis.

6.2 Fabrication of biepitaxial grain boundary junctions

In this work all the STO and YBCO films were deposited by Pulsed Laser Deposition (PLD). In the PLD method a target is hit repeatedly by short laser pulses. Each pulse will cause a highly directional plume of evaporated material that comes out from the target. The ejected material will hit a substrate that is glued to a heater and oriented with the surface against the plume, see figure 6.1. PLD is a very flexible method that allows thin films of many different materials to be grown. In optimal deposition conditions the deposited material will have a stoichiometry close to that of the target.

At the same time PLD is a rather complex deposition technique involving precise control of several parameters. For the deposition of oxide thin films one needs a careful tuning of:

1. Temperature of the substrate.
2. Distance between target and substrate.
3. Oxygen pressure during deposition.
4. Energy of the pulse and frequency.
5. Annealing procedure (in oxygen) when the thin film deposition is completed.

6.2. FABRICATION OF BIEPITAXIAL GRAIN BOUNDARY JUNCTIONS

Parameter	STO	YBCO
Deposition temperature, T_D (C°)	680	790
Pulse frequency (Hz)	1	10
Deposition pressure (mb)	0.2	0.6
Energy density (J/cm ²)	1.8-1.9	1.8-1.9
Annealing pressure (mb)	800	800

Table 6.1: Parameters used when depositing oxide films by PLD.

In table 6.1 the values of these parameters are listed for YBCO and STO depositions.

The key steps to fabricate our biepitaxial films are outlined in Figure 6.2. A MgO (110) substrate and STO (110) seed layer are chosen to achieve the desired orientations for the YBCO film, see figure 6.2 a). After the STO is deposited by PLD an amorphous carbon mask is deposited. The mask is patterned using electron beam (e-beam) lithography and oxygen plasma. The seed layer is then partially removed using ion milling, see figure 6.2 b). The YBCO film is then deposited. For our choice of deposition parameters it will grow with a (001) orientation on the MgO substrate and (103) on the seed layer. The interface, where the ab planes of the (001) film meet the tilted planes of the (103) growth will constitute the grain boundary, see figure 6.2 c). To define the junctions the YBCO film is patterned again using a carbon mask, e-beam and ion milling cycle. In this way the final width of the grain boundary junction, w_J , is defined. In our work we have used w_J in the range 200 - 500 nm. This way of patterning the grain boundaries will be referred to as the *conventional method*. A more detailed description of all the steps involved in the process is available in Appendix A.

YBCO (103) films which grows on a flat STO (110) surface consists of a mixture of [103] and [-103] grains. To select only one growth we use vicinal substrates cut with a small angle of 6° with respect to the [110] direction[72].

The interface angle of the grain boundary is characterized by θ which is defined with respect to the MgO [001] in plane direction. In figure 6.2 c) the two GB cases for an interface angle of $\theta = 0^\circ$ and 90° , which are referred to as $45^\circ[0\ 1\ 0]$ tilt and $45^\circ[0\ 1\ 0]$ twist respectively, are marked with arrows. For intermediate values of θ the grain boundary will gradually make a transition between these two cases. The type of rotation influence the microstructure of the GB, which in turn impacts the transport properties.

Figure 6.3 shows a TEM image of an interface of a biepitaxial junction

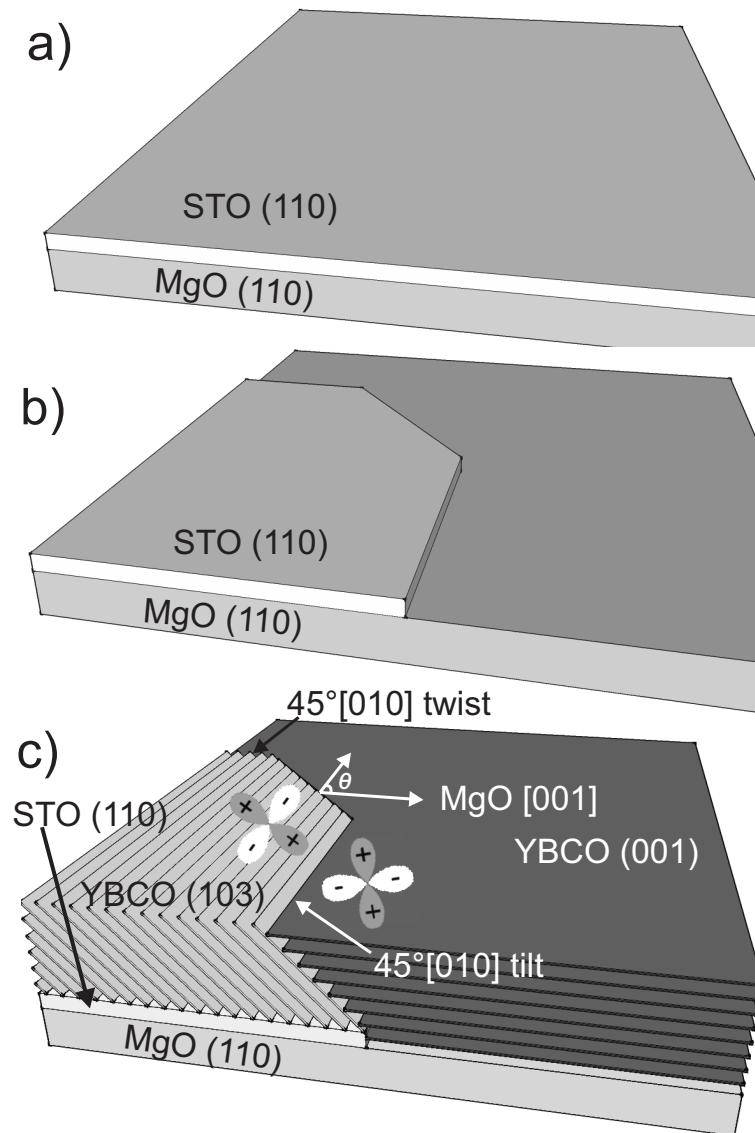


Figure 6.2: a) The MgO (110) substrate with a STO (110) seed layer deposited by PLD. b) The seed layer after patterning by e-beam and ion milling. The different orientations of the three defined seed layer edges give junctions with different structural and transport properties. c) The YBCO film grows (001) on the MgO and (103) on the STO. The 45° [010] tilt and 45° [010] twist junctions are marked as well as the orientation of the d-wave order parameter.

6.2. FABRICATION OF BIEPITAXIAL GRAIN BOUNDARY JUNCTIONS

having $\theta = 0^\circ$. In the two insets a disordered layer can clearly be seen in the region where the two grains meet. In our junctions we have seen two types of grain boundaries: In the top left inset of figure 6.3 a Basal plane Grain boundary is shown, here the ab-planes of the left grain terminate into a single ab-plane of the grain on the right. In the lower right inset the ab-planes of the left grain terminate into the ab-planes of the right side.

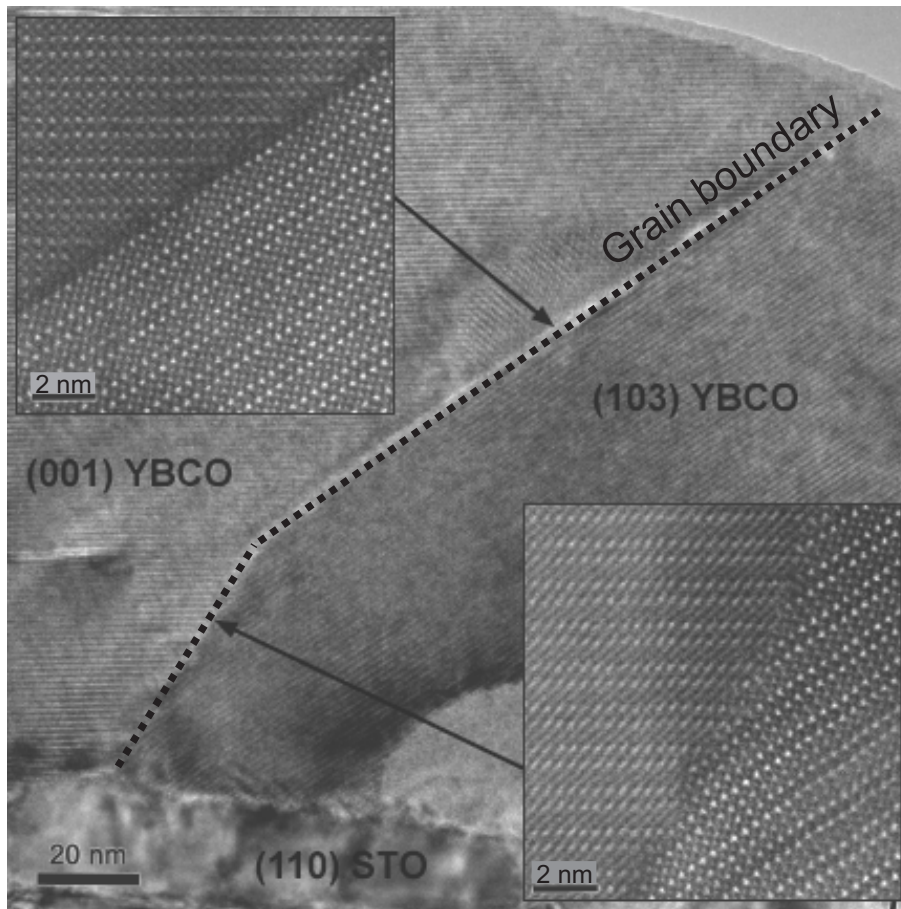


Figure 6.3: Transmission Electron Microscope image of a cross section of one of our biepitaxial junctions. The grain boundary is marked with a dashed line. The brightness of an atom in the image depends on its weight. The white, slightly larger, Ba atoms are clearly seen. In the middle position in the unit cells the slightly weaker Y atom is visible.

6.3 Nucleation of greenphase on MgO (110)

By using conventional nanopatterning (e-beam lithography and a carbon mask) one can in principle reach widths below 100 nm. However, the ion milling procedure causes considerable damage to the grain boundary. This is especially severe for widths below 300 nm. We shall come back to this point in chapter 8 and 9. To approach this problem we have engineered a new *soft-patterning* method. The essential part of this new method is the fact that on MgO (110) the greenphase, Y_2BaCuO_5 (Y211), will compete with the growth of the superconducting $\text{YBa}_2\text{Cu}_3\text{O}_{7-\delta}$ (Y123). Y211 has an orthorhombic structure[73] and is an insulator.

Figure 6.4 a) and b) shows two Scanning Electron Microscope (SEM) images of interfaces between (001) and (103) YBCO. The two samples were deposited using similar parameters, however some distinct differences are visible. The film in figure 6.4 a) has a rather homogeneous growth. In figure 6.4 b) the greenphase appears as an elongated grainy structures preferentially located at the grain boundary.

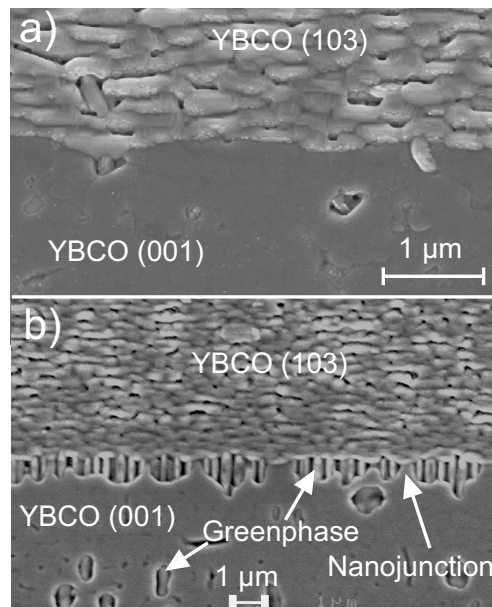


Figure 6.4: a) A SEM image of a YBCO film with a homogeneous grain boundary (the interface shows the faceting behavior common in all our samples). The (001) YBCO have a fairly uniform growth while the (103) YBCO consists of elliptical grains resulting in a rough film. b) A considerable amount of greenphase can be seen at the grain boundary of this film.

6.3. NUCLEATION OF GREENPHASE ON MGO (110)

It is not completely clear under what conditions the Y211 precipitate will start to nucleate in films dominated by the Y123 phase. In bulk samples there is a clear transition from Y123 to a Y211 at high temperatures[74]. Figure 6.5 shows the phase diagram for bulk YBCO as a function of oxygen pressure and temperature. Our films have been optimized to a pressure of 0.6 mb which, according to the phase diagram, place the Y123 to Y211 transition at almost 1000°C. This is significantly higher than the deposition temperature (T_D) ranges used to optimize our Y123 growth (740-800°C). Y211 has also been observed in bulk samples at lower temperatures, but this seems to require a high oxygen pressure[75].

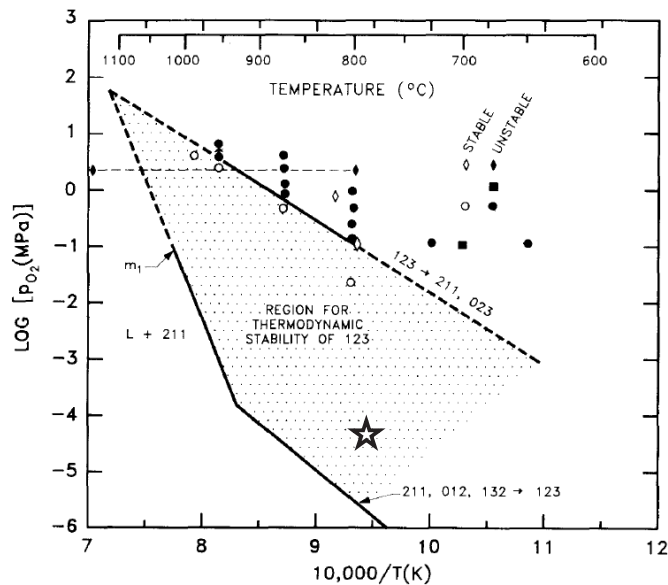


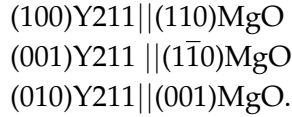
Figure 6.5: Phase diagram for bulk YBCO, adapted from [74]. The different YBCO phases are shown as a function of oxygen pressure and temperature. The star represents the region of the parameters used in this thesis.

Despite the behavior of bulk samples of YBCO, the Y211 growth is clearly present in a number of our films grown on MgO (110). Scotti di Uccio and coworkers[76] studied the growth of precipitates on a STO substrate with a MgO seed layer. They also observe nucleation of Y211 on the MgO, but not on the STO side of the substrate. Films with noticeable amounts of Y211 require an excess of yttrium in the growth. This would suggest that it should also nucleate on the STO surface. However a different yttrium rich phase, Y₂O₃, is favorable on STO and will grow in the Y123 film. When there is an excess of yttrium, Y₂O₃ is the more likely precipitate

Parameter	MgO (Å)	STO (Å)	YBCO (Y123) (Å)	Y211 (Å)
a,b [100], [010]	4.2	3.9	3.88	a= 7.19 b=12.18
[110]	5.9	5.52	-	-
c,[001]	4.2	3.9	11.7	5.66

Table 6.2: The lattices parameters of the materials used in this thesis[76][10][70].

for most substrate choices. On MgO (110) however, Y211 will nucleate in yttrium rich depositions due to its favorable epitaxial relationship with the substrate. The lattice parameters of the substrates and films are reported in table 6.2. The Y211 grows on the MgO substrate with the following epitaxial relations[76]:



An important detail is that the greenphase growth increases significantly at the grain boundary interface. This has been attributed to the fact that when the Y211 nucleates on the MgO substrate the concentration of yttrium adatoms decrease on this side of the boundary. Excess yttrium from the STO side will migrate to equalize the concentration and results in an increased growth of Y211 on the MgO substrate in the region close to the interface line. [76]. The mixture of Y211 and Y123 at the interface is the key component of our new method to make nanoscale GB junctions.

Early studies in our group suggested that there was a connection between T_D and the growth of Y211 on the MgO substrate. We have therefore deposited a number of films at different temperatures and checked for greenphase growth. However, it has been difficult to find a strong correlation between the density of greenphase and T_D . In our films we have observed significant amounts of greenphase at T_D both above and below the optimal value = 790° (optimal in respect to critical temperature and film uniformity). However the most successful films were deposited at a temperature of $740^\circ C$, 50 degrees below the optimal T_D . The quality of the MgO surface might also play a role in the formation of the Y211 phase. In the fabrication process there are two steps where the substrate is etched by ion milling, any inhomogeneities formed here will affect the YBCO growth and possibly cause spurious phases.

6.4 Soft nanopatterning

The soft nanopatterning technique is based on the possibility to create GB interfaces where nano sized superconducting Y123 connections are embedded in insulating greenphase. First $10\ \mu\text{m}$ wide grain boundary junctions are created using the conventional lithography method. A slightly lower T_D is used for the YBCO film. The grain boundary is examined using atomic force microscopy (AFM) and scanning electron microscopy (SEM), see figure 6.6 a).

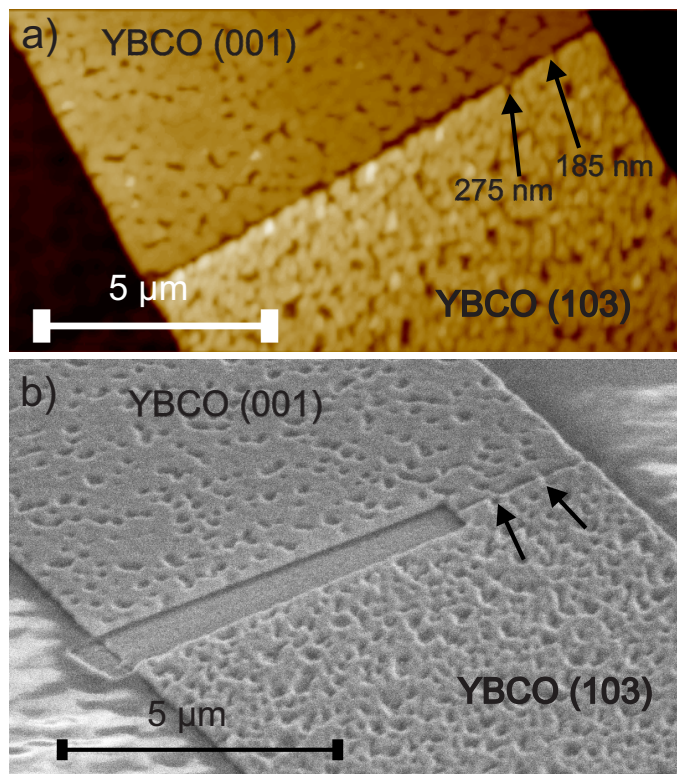


Figure 6.6: a) AFM image of an interface containing a large amount of greenphase before the FIB step. b) SEM image of the same interface after a region of the film have been removed by FIB leaving two nanojunctions, 275 and 185 nm wide, and approximately 500 nm of greenphase on each side. The resulting device is a nanoSQUID with a loop area of approximately $0.1\ \mu\text{m}^2$.

Using a Focused Ion Beam (FIB) one or two Y123 connections are isolated while at the same time leaving 300-400 nm of greenphase on each side, see figure 6.7. In this way the lateral sides of the superconducting

connection will not be in direct contact with the ion beam, which is the main source of damage of the grain boundary. The Y211 phase is insulating and will not contribute to the electrical transport of the junction. Figure 6.6 b) shows an interface after the FIB cut leaving two Y123 connections 275 and 185 nm wide. The resulting device is a nanoSQUID with a loop area of approximately $0.1 \mu\text{m}^2$.

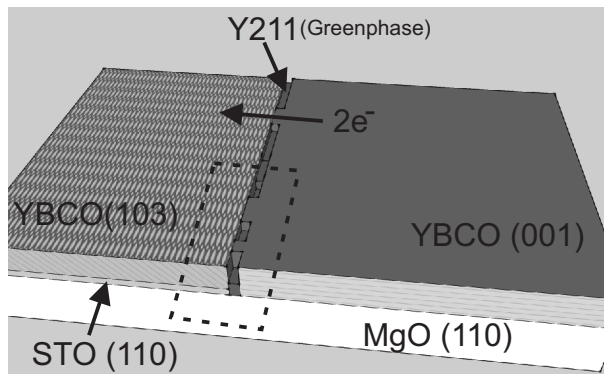


Figure 6.7: A sketch of the grain boundary interface showing a mixture of greenphase and nanojunctions connecting the two films. The dashed region is to be removed by FIB leaving a single nanojunction that has not been in direct contact with the ion beam.

Chapter 7

The measurement setups

Two different refrigerators were used to reach the sub kelvin temperatures required when characterizing our samples. An Oxford Heliox VL ^3He and an Oxford TLE 200 dilution refrigerator for temperatures down to 280 mK and 15 mK, respectively. In both cases the sample is glued to a sample holder (unique for each fridge). The junctions and devices on the sample are connected to gold pads deposited on top of the YBCO electrodes. These pads are connected to the contacts of the sample holder by wedge bonding using a gold wire of 25 μm diameter.

7.1 280 mK system - Heliox

The measurements in chapter 8 and 9 were all done in the Heliox system. All the devices were fairly low ohmic with finite critical currents, therefore measurements was carried out in a current biased mode. A high ohmic series resistance R_b , is used to bias the device and another smaller resistor, R_s , is used to indirectly measure the current. The refrigerator and battery driven voltage preamplifiers are placed in an electromagnetic interference shielded room. Voltage and current sources, Digital multimeters, analog to digital converters (ADC) and the computer, are instead positioned outside the shielded room, see figure 7.1. At the input/output of the matrix box, where the lines are connected to the amplifiers and source, the signal is filtered by simple LC filters. The electronics used in the measurements were:

- 2 Stanford Research SR560 voltage preamplifiers
- 2 HP 34401A multimeters

CHAPTER 7. THE MEASUREMENT SETUPS

- 1 Fluke PM3380A Oscilloscope
- 1 Yokogawa 7651 dc-source, used as a source for a small coil of copper coated niobium wire used to generate a magnetic field up to about 40 mT
- 1 Agilent 33220A arbitrary function generator, used for biasing
- 1 Stanford Research Dynamic Signal analyzer SR785, used for the noise measurements.
- 1 National Instruments PCI-6052E data acquisition card (DAQ)

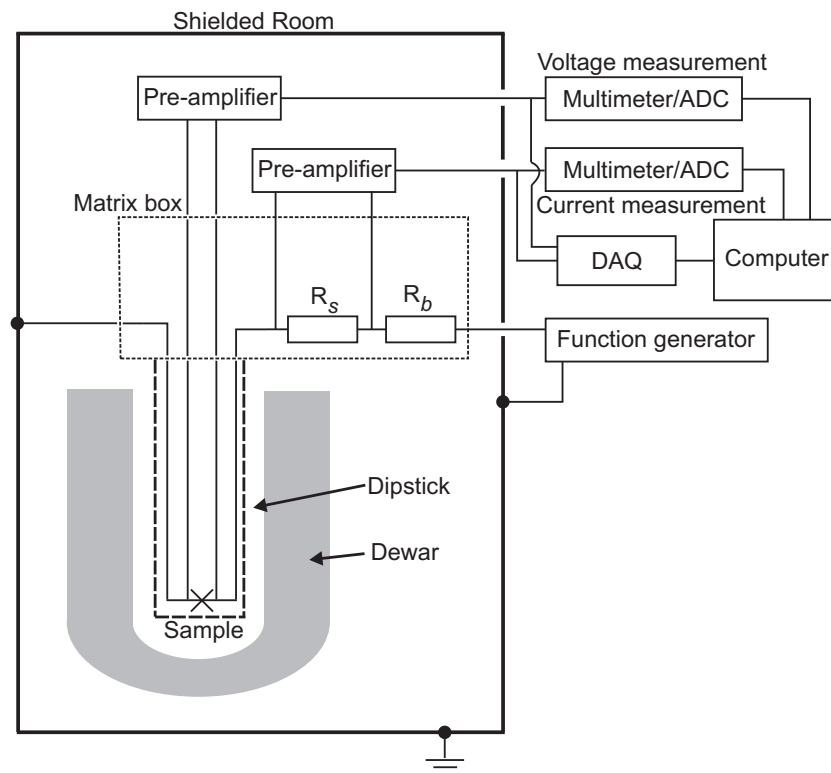


Figure 7.1: A schematic illustration of the 300 mK Heliox measurement setup.

7.2 15 mk system

The SETs in chapter 10 were all measured in the dilution fridge. The low base temperature (15 mK) allows us to study charging effects which would be impossible to observe in the Heliox system due to thermal smearing in our low E_C devices.

Several filters are used to minimize high-frequency noise in the measurements, a sketch of the filters and measurement electronics can be seen in figure 7.2. The cryostat and amplifiers are situated in a shielded room similarly to the Heliox setup. On top of the fridge, at room temperature, every line is equipped with a feed-through capacitor (100 pF). At the 1 K pot the lines go through a multistage RCL filter and finally at the 15 mK stage the lines are once again filtered using a copper-powder filter and a Thermocoax[77]. The latter two filters are very effective in attenuating photons above 1 GHz. This strong attenuation is a requirement to thermalize the electron system of our devices to the base temperature of the fridge.

Due to the large range of resistances of the measured devices in this system the electronic setup varied quite a lot. The basic setup was similar to what was used in the Heliox system, a simple current bias through a resistor (R_b) and two voltage preamplifiers (all built into one box). For the high resistive samples a voltage bias setup was used instead (shown in figure 7.2). Here a current preamplifier was used together with a single voltage preamplifier. The input of the voltage amplifier was connected to the source, outside the shielded room, and the two outputs to a multimeter and the line going down to the sample respectively. The list of electronics used in this setup was:

- 2 Stanford Research SR560 voltage preamplifiers
- 2 Keithley model 2000 multimeters
- 1 Kenwood CS-4125 Oscilloscope
- A Keithley 213 Quad Voltage Source and a Yokogawa 7651 dc-source, used to bias the device and the gate connection.
- A Stanford Research SR570 current preamplifier or a Femto DDPCA-300 Current Amplifier

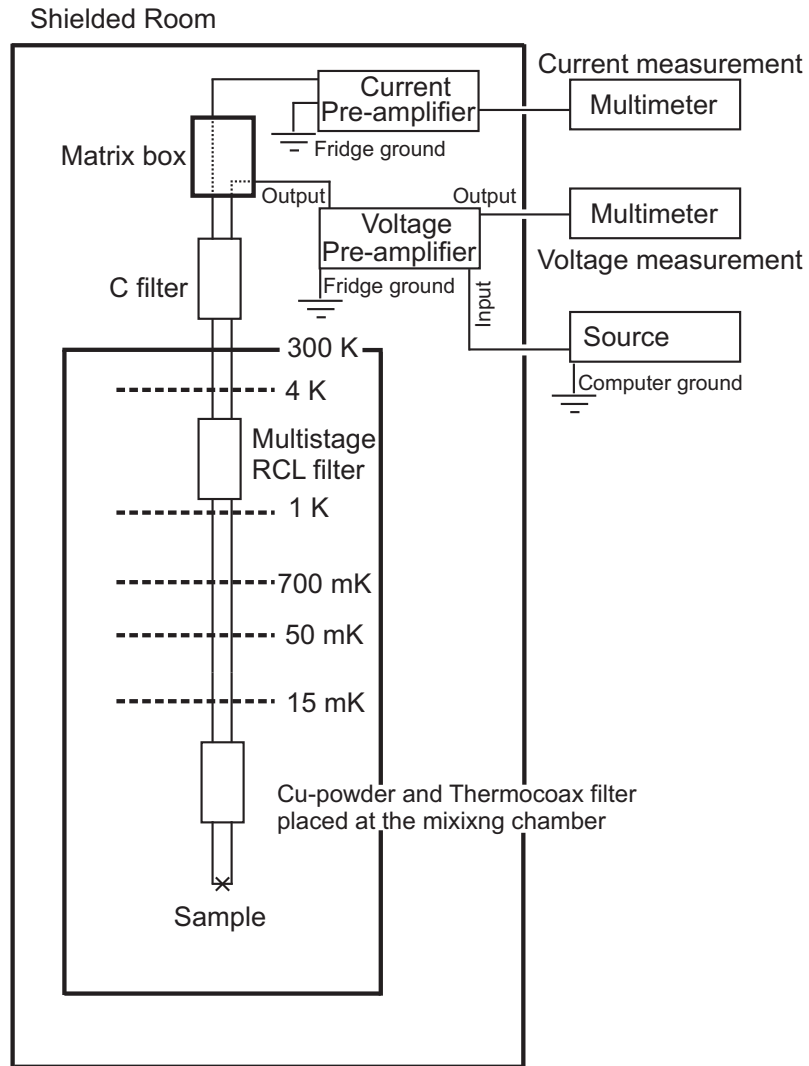


Figure 7.2: A sketch of the 15 mK system showing the voltage bias setup. The voltage preamplifier was a Stanford SR560 and the current preamplifier were either a Stanford SR570 or a Femto DDPCA-300.

Chapter 8

DC characterization of nano grain boundary junctions

The many complex steps of the fabrication of submicron HTS junctions may deteriorate the transport properties of the GB. For example, in fabrication steps involving high temperatures oxygen out diffusion can change the doping of the material.

To define the GB width either a focused ion beam procedure or ion milling etching is commonly used. In particular the ion milling can lead to structural damages or Ion implantation in the sensitive GB region.

In this chapter we compare the transport properties of nanojunctions fabricated with two different methods, namely conventional patterning (e-beam lithography using a carbon mask) and our novel soft nanopatterning technique. We will show that ion milling indeed causes serious deterioration in GB junctions of widths less than 500 nm, and that our soft nanopatterning method instead preserves the pristine GB region down to widths of 100 nm.

8.1 Critical current densities and normal resistances

Junctions with nominal widths in the range 200-500 and 100-500 nm were obtained for the conventional and soft patterning methods, respectively. The layout of the conventionally patterned GBs consisted of 2 junctions in series to allow the study of charge blockade effects (addressed in detail in chapter 10).

Figure 8.1 shows three different IVCs of samples fabricated with conventional patterning. The 200 nm wide junction shown in a) is representative for all measured junctions of the same width on the same sample. They

either showed a high resistive nonlinear IVC or were an open circuit. The two IVCs shown in b) and c) are both from 300 nm wide junctions; despite the same width the critical currents are very different. Results for the junctions of the "conventional sample" are summarized in table 8.1.

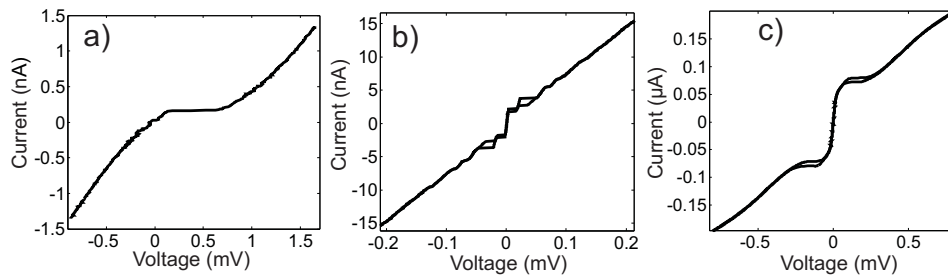


Figure 8.1: Current voltage characteristics for grain boundary junction fabricated with the conventional nanopatterning method, having a junction width of a) a 200 nm, b) and c) 300 nm. The second switch is due to our layout consisting of two Josephson junctions in series to also study charging effects.

Sample nr	Junction Width (nm)	J_C (A/cm ²)	R_N (Ω)	IVC Behaviour
Nr 1	200	0	75 M	"Blockade like"
Nr 2	200	0	2.1 M	"Blockade like"
Nr 3	500	3	5.6 k	Josephson
Nr 4	200	0	180 k	"Blockade like"
Nr 5	200	0	600 k	"Blockade like"
Nr 6	300	566	1.3 k	Josephson
Nr 7	300	7	12.4 k	Josephson
Nr 8	300	116	10.1 k	Josephson
Nr 9	300	7	13.4 k	Josephson

Table 8.1: A summary of the samples fabricated by the conventional method. The table shows the total R_N for two junctions in series. All of the conventional junctions had an interface angle $\theta = 0$.

8.1. CRITICAL CURRENT DENSITIES AND NORMAL RESISTANCES

Junction nr	θ	Junction Width (nm)	J_C (A/cm ²)	R_N (Ω)
Nr 1	30°	270	$12.3 \cdot 10^3$	170
Nr 2	35°	260	$12.8 \cdot 10^3$	80
Nr 3	40°	100*	$2.9 \cdot 10^3$	1050
Nr 4	50°	240+280	$8.9 \cdot 10^3$	90
Nr 5	55°	250+230	$3.8 \cdot 10^3$	560
Nr 6	60°	190+280	$5.3 \cdot 10^3$	300
Nr 7	65°	200	$2.6 \cdot 10^3$	900
Nr 8	75°	120+260	$11.5 \cdot 10^3$	80
Nr 9	90°	320	$13 \cdot 10^3$	90

Table 8.2: A summary of the junctions and SQUIDs fabricated by the soft nanopatterning method. * This junction was not clearly seen in AFM, a width of 100 nm was extracted from I_C vs B pattern.

Figure 8.2 shows two typical IVCs for the soft patterning technique, \approx 100 and 200 nm wide respectively. Two significant differences, compared to the conventional junctions, can be pointed out: first the I_C values are order(s) of magnitude higher despite the similar junction areas. Second, the 100 nm wide junction shows a finite I_C instead of the high resistive nonlinear IVC that we have measured for all the 200 nm wide junctions fabricated with conventional patterning. The results for the soft patterned junctions are summarized in table 8.2.

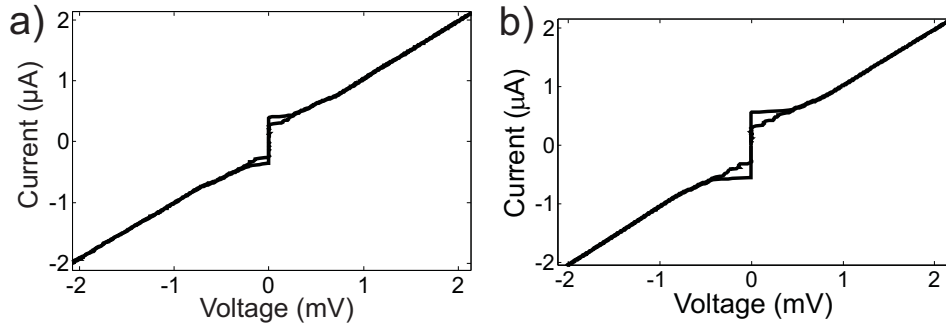


Figure 8.2: IVCs for soft patterned grain boundaries a) \sim 100 and b) 200 nm wide respectively.

By comparing the critical current densities of the junctions created by the two methods one gets a clear indication of the damage done to the grain boundary during the fabrication process. The junctions fabricated by

the soft patterning technique have J_C in the range 10^3 - 10^4 A/cm². While the junctions created with the conventional method have J_C ranging from 10^0 to 10^3 A/cm².

The two methods also show a significant difference in normal resistance. The conventional method gives higher specific resistance, $\rho_N = R_N A_J$, in the range 10^{-7} - 10^{-2} Ωcm^2 , whereas the soft patterning technique gives a ρ_N in the range 10^{-8} - 10^{-7} Ωcm^2 .

The big difference in J_C and ρ_N values between the two fabrication methods shows that part of the superconducting transport through the grain boundary is suppressed in the conventional patterning process.

8.2 Testing the validity of the soft nanopatterning method

To further characterize the Josephson junctions fabricated using the soft patterning method we have recorded the magnetic field response of the Josephson current. The modulation of the critical current gives important information about the grain boundary interface structure. Figure 8.3 a) shows a typical I vs B measurement for a junction before the FIB cut. The critical current modulates rapidly and in an irregular way. This is a consequence of the many parallel superconducting connections separated by insulating greenphase that make the structure resemble an array of parallel Josephson junctions. Figure 8.3 b) shows the magnetic pattern of the same structure after a single superconducting connection has been isolated using FIB. This dependence is much more regular with slower modulations, displaying an almost ideal Fraunhofer-like behavior which is expected for a single Josephson junction.

As a final check of the validity of the soft nanopatterning method we have used high-resolution TEM and studied the cross section of an extracted grain boundary. This is done to distinguish between the scenario of an interface that consist of parallel arrays of Y123 junctions separated by regions of Y211 and the scenario of a single GB with a highly non-uniform J_C distribution. TEM and Energy dispersive X-ray (EDX) was used to confirm the presence of a Y₂BaCuO₅ precipitate that extends all the way from the substrate surface to the top of the film, proving that the first scenario is true for our GBs. The details are available in paper I.

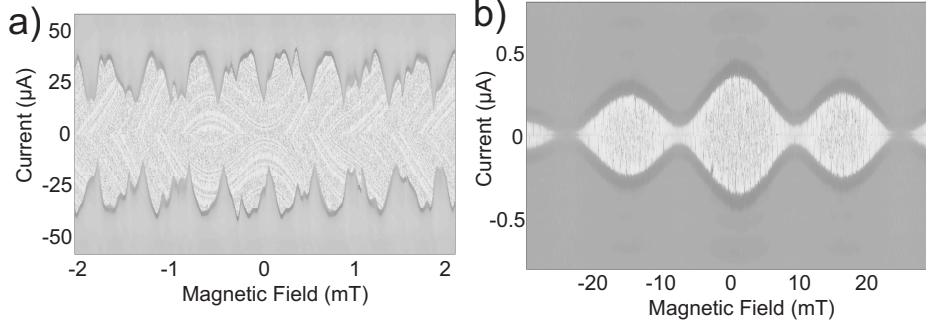


Figure 8.3: I vs B for a $10 \mu\text{m}$ interface a) before the FIB and b) after a single junction has been isolated. This junction was not clearly seen in the AFM scan, however a width of approximately 100 nm was extracted from the magnetic pattern. The gray scale represents the logarithmic conductance and the bright (dark) region corresponds to high (low) conductance. The region of rapid decrease in brightness corresponds to the I_C of the junction.

8.3 Extracting the effective width - Soft nanopatterned junctions

From the modulation period, ΔB , of the I_C versus B pattern it is possible to extract the effective width, w_{eff} , of the superconducting region in the GB. The expression that includes demagnetization effects is given by[80]:

$$\Delta B = \frac{\Phi_0 t}{1.2 w_{eff}^2 (\lambda_{001} + \lambda_{103} + d)} \quad (8.1)$$

where t is the thickness of the film, λ_{001} and λ_{103} is the London penetration depth of the first and second electrode and d is the length of the junction¹. This relation is valid in the *thick film limit* which holds for the soft nanopatterned junctions (when the electrode width, $w_{elec} > \lambda_L^2/t$).

Equation 8.1 was used on a number of junctions fabricated by the soft patterning method to extract w_{eff} . The extracted width was then compared with the width acquired from AFM and SEM images. The result was in good agreement, showing a deviation of at most 40%.

¹ λ_{001} for the YBCO (001) electrode is directly given by $\lambda_{ab} \approx 160 \text{ nm}$ at $T_C=89 \text{ K}$ [81]. λ_{103} will be a combination of λ_{ab} and λ_c with a dependence on the grain boundary angle θ [82]: $\lambda_{103}^2 = \lambda_{ab}^2 \cos^2 \theta + \frac{1}{2} (\lambda_c^2 + \lambda_{ab}^2) \sin^2 \theta$, where $\lambda_c \approx 2 \mu\text{m}$ [16]

8.4 Extracting the effective width - Conventionally nanopatterned junctions

The junctions fabricated by the conventional method are, due to their narrow electrodes (same width as the grain boundary junction), in the *thin film limit* ($w_{elec} \leq \lambda_L^2/t$), where ΔB is given by[80]:

$$\Delta B = \frac{1.84\Phi_0}{w_{eff}^2} \quad (8.2)$$

Figure 8.4 shows the I vs B for a 300 nm wide conventional junction. At these high magnetic fields flux trapping in the region close to the junctions is almost impossible to avoid. This will cause current jumps in the magnetic pattern and deviations from a conventional behavior. However we were able to extract a ΔB of ≈ 1 T which gives $w_{eff} \approx 60$ nm. Equation 8.2 was used on two more conventional junctions. The extracted widths were approximately 200 nm narrower than the nominal width of the grain boundary. These results show that during the ion milling process a layer (≈ 100 nm wide) on each lateral side of the GBs is formed where the Josephson coupling is absent. This picture is reinforced by the fact that none of the 200 nm wide GBs showed any Josephson current.

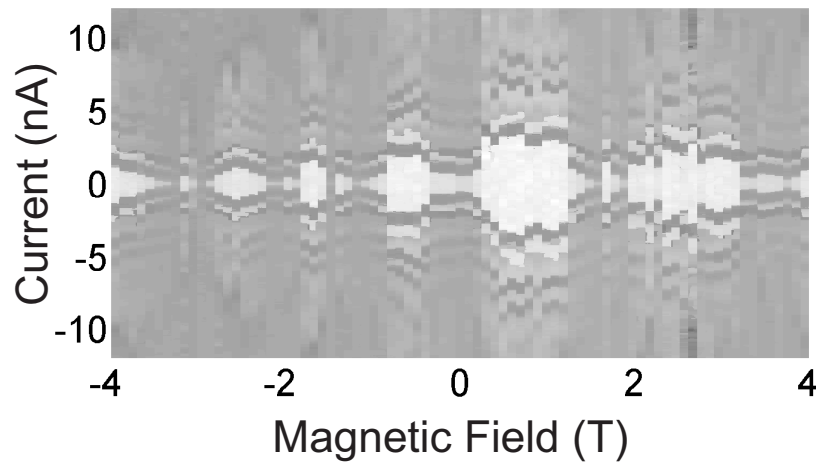


Figure 8.4: I vs B for a conventional grain boundary junction. At these high fields a significant amount of flux trapping takes place, however the modulation period is roughly equal to 1 T.

8.5 Characterization of a nanoSQUID

Figure 8.5 a) shows the I vs B pattern for the nanoSQUID patterned in figure 6.6 before the FIB cut and figure 8.5 b) after the SQUID has been isolated. The magnetic pattern of the 10 μm interface shows the quick and irregular modulations similar to a parallel array of a large number of Josephson junctions. After the FIB cut the pattern resembles that of a SQUID with distributed junctions, which is consistent with the tiny SQUID dimensions.

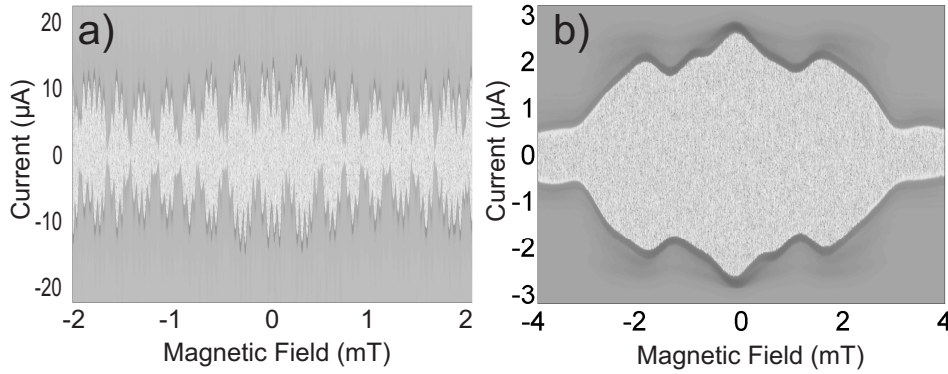


Figure 8.5: I vs B for a 10 μm interface a) before the FIB session and b) after FIB has been used to create a nanoSQUID. The gray scale represents the logarithmic conductance of the SQUID.

A hump can be noticed on the side of the inner lobes. This can be accounted for by considering that the Josephson current-phase relation (CPR) of the junctions is unconventional. Indeed HTS Josephson junctions can have a more complex CPR than conventional LTS Josephson junctions due to d-wave symmetry of the order parameter. For certain grain boundary configurations zero-energy Andreev bound states can be present at the junction interface giving rise to a second harmonic component. In these cases the CPR can be written as:

$$I_S = I^I \sin(\phi) - I^{II} \sin(2\phi). \quad (8.3)$$

We managed to reproduce the peculiar features of the SQUID magnetic field response[25]. Figure 8.6 a) shows the magnetic field dependence of a SQUID considering point-like junctions with a CPR with both first and second order harmonics. The calculated dependence shows that a hump on one side of every lobe appears in asymmetric SQUIDs with one of the two junctions having a larger amplitude of the second order harmonics compared to the other. In figure 8.6 b) we have calculated the magnetic pattern

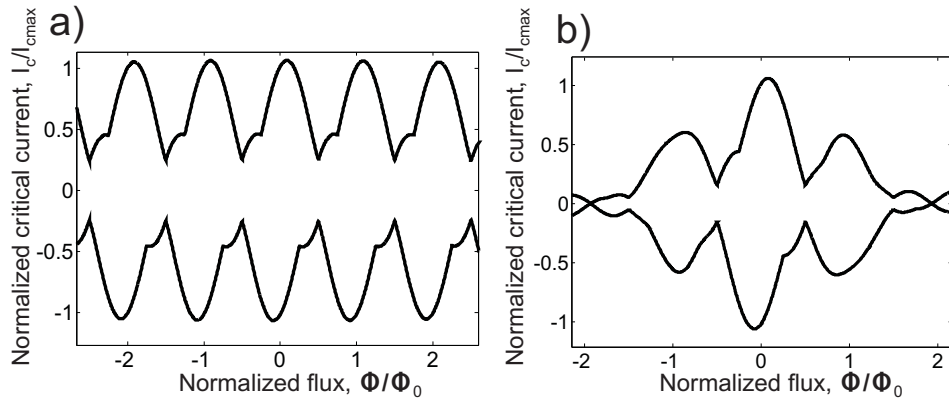


Figure 8.6: a) A simulation of I_C vs B for a SQUID with pointlike junctions, where one of the two junctions has a significant amplitude of second harmonics. b) I_C vs B for a SQUID with distributed junctions and asymmetric current phase relation.

for a distributed SQUID with the two junctions having the same area and widths comparable to the size of the SQUID loop. When the Fraunhofer dependence of the junctions is included it acts as an envelope over the SQUID modulations, making all the features related to the unconventional CPR very similar to those observed in the measured nanoSQUID pattern.

The I_C vs B of the nanoSQUID of figure 8.5 b) was measured at a higher temperature (34 K). Here the hump structure was almost completely suppressed while the main lobes were still clearly visible. A faster decrease of the amplitude of the second harmonic components compared to the first harmonic component with increasing temperature is predicted in the model for zero-energy Andreev bound states[52][25].

The phenomenology we have observed is also compatible with a recently predicted[78] new striped superconductive state for HTS, which can lead to a number of novel phases, like a charge $4e$ state with a corresponding fractional flux quantum $\frac{h}{4e}$ in mesoscopic rings. Our data could also be explained by the occurrence of quartets Cooper pairs tunneling at the interface of specific grain boundaries[79]. Further experiments are required to clarify which mechanism is indeed realized in our nano device.

Chapter 9

Noise characterization of nano grain boundary junctions

To reproducibly fabricate Josephson GB junctions on the nanoscale it is vital to understand the microscopic properties and the mechanisms of charge transport through the GB. The low-frequency noise can be used as a tool to study the transport dynamics of both quasiparticles and Cooper pairs. Through noise characterization it is possible to extract information about the nature of the grain boundary interface and its homogeneity. This chapter will summarize and discuss the results of paper II that focuses on voltage noise measurements of GBs made by the conventional and soft nanopatterning techniques.

In the previous chapter it was shown that the GB junctions fabricated by the two methods have significantly different electronic properties (reflected in the difference in ρ_N , J_C and ΔB). There is additional information regarding the GB interface to be gained by investigating the low frequency noise. The main goal is to compare the noise properties of our junctions to the GB models described in chapter 4.

The width of the outmost superconducting region in the junctions fabricated by the conventional patterning method was shown to be reduced compared to the nominal junction size due to a severely damaged layer, approximately 100 nm wide, on each lateral side of the junction. For the soft patterned junctions these layers are instead close to zero. Figure 9.1 a) and b) show a sketch of the interface area of two possible scenarios for a GB which has been damaged during the patterning procedure. In a) the area through which Cooper pairs flow is evenly spread. The width of that area, w_{eff} , can be much smaller than the nominal width. In b) multiple parallel regions provide the Cooper pair transport, the width of the outer point of

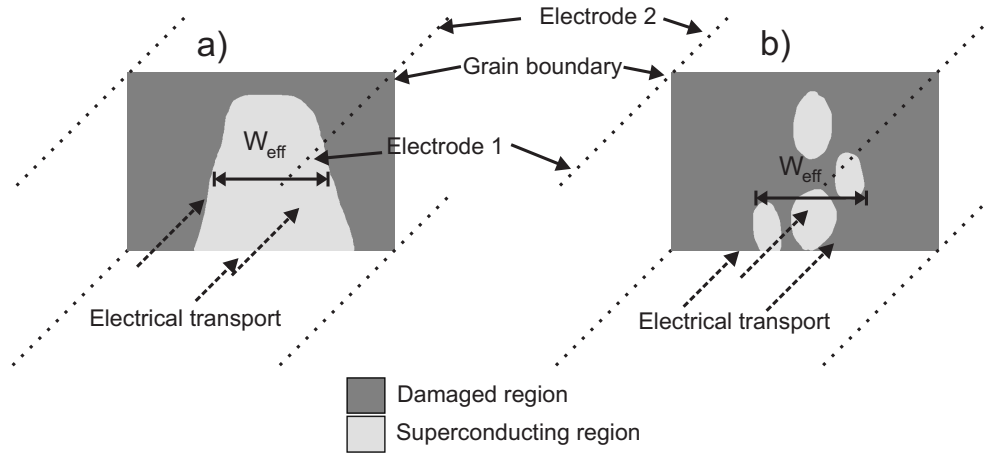


Figure 9.1: Sketch of two possible distributions of the superconducting channels in a grain boundary interface that has been damaged by patterning. a) A single superconducting channel and b) multiple parallel superconducting channels separated by non superconducting regions. The mechanisms described in the ISJ or SIS model can be applied to the superconducting regions of this simple sketch.

the superconducting regions is the same as in a) but the total area is clearly less. By just looking at the magnetic field period (ΔB) of the I_C modulations it is not straight forward to separate between these two scenarios¹ or estimate the total area of the region that carry the Cooper pairs. Both of these issues can be treated by analyzing the voltage noise of the GB.

9.1 S_i and S_r

The voltage noise spectral densities (S_V) of both types of GBs were measured in the frequency range between 1 Hz and 100 kHz using a Stanford Research Dynamic Signal analyzer SR785, see inset of figure 9.2. Voltage noise spectra were acquired for a number of bias points to be able to fit the noise data at a fixed frequency to equation 4.2 and extract S_i and S_r . Figure 9.2 shows S_V at 10 Hz (open circles) as a function of the bias current for a 200 nm wide soft-patterned junction with a nominal interface angle $\theta = 30^\circ$ (from an AFM scan, however, it was learned that the actual angle was closer to 0°). The data points (open circles) are fitted using the theoretical expres-

¹A non Fraunhofer like pattern is an indication of the b) scenario but it could also be caused by faceting.

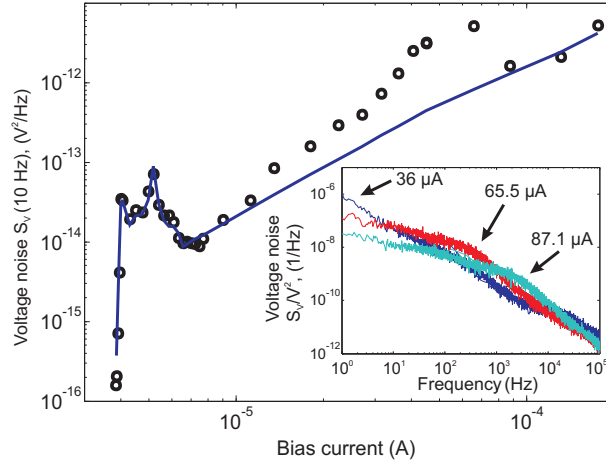


Figure 9.2: Voltage noise at 10 Hz as a function of bias current (open symbols) for a soft-nanopatterned junction. The solid line is a theoretical fit used to determine S_i and S_r . The hump centered around $50 \mu\text{A}$ is due to a 2-level charge trap and move in frequency when the bias is changed (inset).

sion (solid line) for $S_V(I)$ (equation 4.2), resulting in the fitting parameters: $S_i \simeq S_r \simeq 10^{-8}/\text{Hz}$ and $k \simeq -1.3$. In this fit the data points between 20 and $80 \mu\text{A}$ have been neglected due to a single 2-level charge trap present here. These data points deviate from the $1/f$ behavior assumed by equation 4.2. The corner frequency of the charge trap moves to higher f as the bias is increased, which is visible in the inset of figure 9.2. The ratio $\sqrt{S_i/S_r} = q$ for this junction is close to 1 which in combination with a negative correlation value, k , suggest that the GB has a very homogeneous barrier where both quasiparticles and Cooper pairs tunnel directly through the same regions. The junction has a tunnel like conductance spectrum (see fig 5 b in Paper II) which in combination with the q value results in a GB with an SIS like behavior, these properties are compatible with the band-bending model.

Our results for this GB junction on the other hand are not compatible with the ISJ or filaments model, for which a larger q is predicted. A q value close to 1 reinforces the picture that the soft nanopatterning method creates GBs of pristine character with few defects introduced in the patterning process. To the authors knowledge similar results have only been reported in one previous work[83] where $1\text{-}2 \mu\text{m}$ wide $2 \times 14^\circ$ [100]-tilt GB junctions (see figure 9.3 for a sketch) were studied and resulted in $q \approx 1$.

The same procedure was carried out for a second soft-patterned junction having $\theta = 50^\circ$. The fit to theory gave $q=1.8 \pm 0.2$ and $k \simeq -0.5$. This

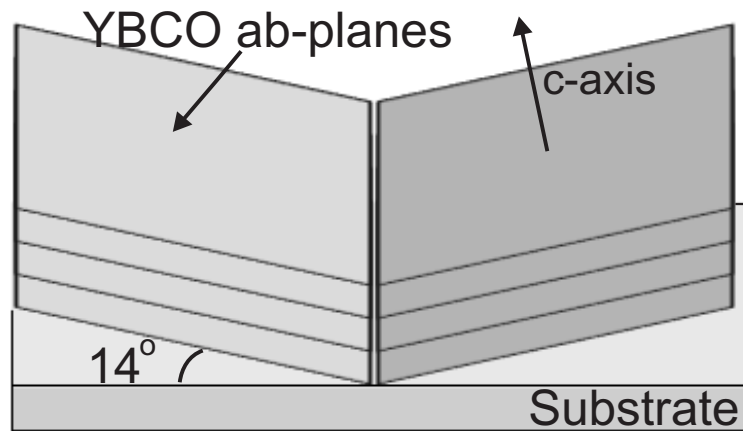


Figure 9.3: Sketch of a $2 \times 14^\circ$ [100]-tilt GB junction.

behavior is best described by the ISJ model.

In paper II a more extensive comparison to HTS GB junctions with different types of rotation and misorientation angle from literature is performed. Although additional studies would be required to conclusively attribute a GB type to a certain transport model, there is a tendency. HTS junctions where the ab planes are rotated around an axis parallel to the GB interface line, for example α° [100] tilt (the type of rotation shown in figure 9.3), are formed with a homogeneous insulating barrier and follow the SIS model (unless the junctions is heavily damaged during fabrication). Other types of GB junctions that deviate from this pure rotation around the interface line, like α° [010] twist (see figure 4.1 a)) or α° [001] tilt (see figure 4.2), tend to be better described by the ISJ model.

TEM images of the GB interface of all these different interface arrangements would be a helpful tool for identifying nanostructures responsible for all these different transport behaviors.

9.2 2-level fluctuators

In this section the focus will be on the Lorentzian spectra, caused by individual 2-level charge fluctuators, that are sitting on top of the $1/f$ background (see figure 9.4). The Lorentzian noise spectra will allow us to extract the area of a charge trap. Moreover from this information we will be able to estimate the area of the junction region through which Cooper pairs can tunnel.

A recurring difficulty with the analysis of the noise measurements of

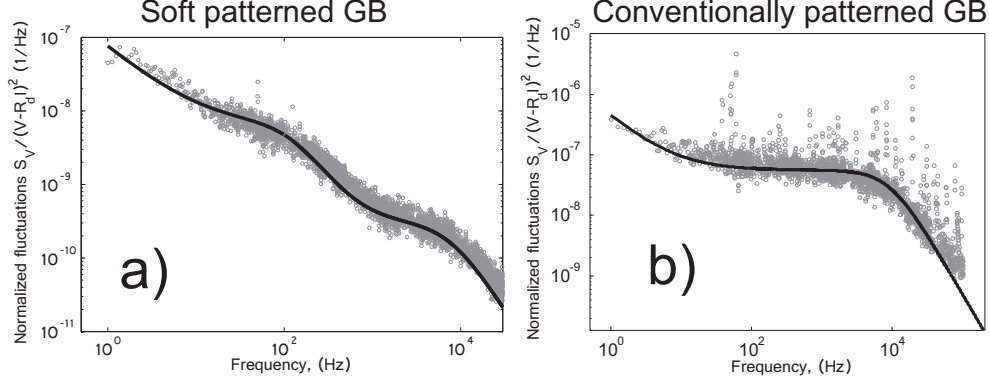


Figure 9.4: a) Noise spectrum for one of the soft-nanopatterned junctions measured at a bias current close to I_C . The solid line is a fit to theory using two Lorentzians and a $1/f$ background. b) Noise spectrum and fit for a conventionally patterned junction measured close to I_C , the charge trap is noticeable stronger than for the soft patterned junction.

our nanopatterned junctions is the appearance of one or a few strong 2-level charge fluctuators. As mentioned previously these are expected when the junction area is very small. Noise measurements performed on conventionally patterned GBs displayed many pronounced 2-level fluctuators. At least one of these fluctuators would always appear at bias currents close to I_C , preventing any attempt at fitting this region to the theory and as a consequence the extraction of S_i . Therefore the value of q could not be determined for the conventional junctions.

In the following we will discuss the effect of a single two level fluctuator on the relative critical current noise spectrum, S_i^{RTS} , and the relative resistance noise spectrum, S_r^{RTS} . Their noise spectra is given by [84][43]:

$$\begin{aligned}
 S_r^{RTS}(f) &= \frac{4\langle(\frac{\delta R_N}{R_N})^2\rangle\tau_{eff}}{1 + (2\pi f\tau_{eff})^2} \\
 S_i^{RTS}(f) &= \frac{4\langle(\frac{\delta I_C}{I_C})^2\rangle\tau_{eff}}{1 + (2\pi f\tau_{eff})^2}.
 \end{aligned} \tag{9.1}$$

Here we use S_i^{RTS} and S_r^{RTS} to indicate that it is the noise contribution of individual charge fluctuators to be distinguished from the S_i and S_r extracted from the $1/f$ spectrum. $\langle(\delta R_N/R_N)^2\rangle$ and $\langle(\delta I_C/I_C)^2\rangle$ are the mean squared relative fluctuations which together with τ_{eff} can be extracted by fitting equation 9.1 (including a weak $1/f$ contribution) to a noise spectrum, see figure 9.4.

The cross-sectional area of the charge trap , A_t , can be understood as the part of the junction area across which charge transport is completely blocked when the trap switches on. In the high bias range, where a junction is dominated by resistance fluctuations, the relative change in junction area can directly be related to the relative root mean-square fluctuations caused by the charge trap:

$$\frac{A_t}{A_{qp}} \simeq 2 \frac{\delta R_N}{R_N}. \quad (9.2)$$

Here A_{qp} is the total area of the quasiparticle transport through the interface. With the same reasoning for bias currents close to I_C the relation is:

$$\frac{A_t}{A_{cp}} \simeq 2 \frac{\delta I_C}{I_C}, \quad (9.3)$$

with A_{cp} being the total area of the Cooper pair transport². From AFM and SEM images it is possible to estimate A_{cp} and A_{qp} (from the I_C vs B measurement of the previous chapter and the fact that $S_r \approx S_i$ they are both assumed to be close to the nominal junction area) for the soft-patterned junctions and in this way extract A_t using equation 9.2. By fitting a total of 24 Lorentzians measured on soft patterned junctions in the high bias range we get an average $A_t = 72 \text{ nm}^2$.

9.2.1 2-level fluctuators in conventionally nanopatterned junctions

The next step is to fit voltage noise spectra from the conventionally fabricated GBs. We know from the previous chapter that the GBs were severely damaged during fabrication so we can not assume that A_{cp} or A_{qp} are close to the nominal junction area. Instead, by assuming that the charge trap area is roughly the same for the two fabrication methods it is possible to estimate the total junction areas that support quasiparticle and Cooper pair transport. $\delta R_N/R_N$ and $\delta I_C/I_C$ are determined by fitting voltage noise spectra in the high bias range and close to I_C , respectively. Using the previously extracted value of the charge trap area A_t together with equation 9.2 and 9.3 we are able to calculate A_{qp} and A_{cp} . In table 9.1 we summarize the results for 3 conventionally fabricated junctions.

There is a significant difference for A_{qp} and A_{cp} for the conventional junctions. While A_{qp} is close to the nominal junction area the Cooper pair area is severely reduced. In the previous chapter a non-superconducting layer of approximately 100 nm on each lateral side of the GB was deduced from the modulation period of the I_C versus B measurements. For junction

²This procedure is described in more detail in paper II

Table 9.1: A_J = Total nominal area, A_{qp} = quasiparticle transport channel area, A_{cp} =Cooper pair transport channel area for 3 conventionally patterned GB junctions. $A_{cp}^{SingleCh}$ is the calculated Cooper pair transport channel area assuming a single channel and a 100 nm non-superconducting layer on each side of the GB.

Sample nr	A_J (nm ²)	A_{qp} (nm ²)	A_{cp} (nm ²)	$A_{cp}^{SingleCh}$
Nr 1	50000	31500	1250	30000
Nr 2	30000	14600	9060	10000
Nr 3	30000	22300	160	10000

nr 1 and 3 in table 9.1 the A_{cp} is an order of magnitude smaller than the Cooper pair area one calculates ($A_{cp}^{SingleCh}$) by assuming a single superconducting channel (figure 9.1 a) and including the non-superconducting layer (film thickness is 100 nm). This strongly indicates that the Josephson coupling is not only switched off on the lateral sides of the conventional GBs. Instead, the total area through which Cooper pairs can tunnel is made up of small and separated regions similar to figure 9.1 b).

We can now evaluate the critical current densities based on the effective area across which Cooper pair transport occurs ($J_C^{eff} = I_C/A_{cp} \simeq 2 - 20kA/cm^2$). The resulting critical current densities are in the same range as those of the soft-patterned junctions. This suggests that the ion milling process switches off the Josephson coupling abruptly rather than gradually decreasing it. The regions that survive the ion milling in the conventional junctions have Josephson properties similar to the soft-patterned junctions.

In conclusion we have not been able to use the $\sqrt{S_i/S_r}$ ratio to correlate the conventionally patterned junctions to one of the GB models. Instead, the information extracted from 2-level charge traps give a strong indication that the conventional GBs are best described by the filament model, where the non-superconducting regions are caused by the patterning process.

*CHAPTER 9. NOISE CHARACTERIZATION OF NANO GRAIN
BOUNDARY JUNCTIONS*

Chapter 10

An all YBCO single electron transistor

To study the symmetry of the superconducting order parameter an all YBCO single electron transistor has been developed. This new nanoscale spectroscopic tool will allow us to obtain information of the quasiparticle spectrum of the entire SET island volume. By studying the parity effect (chapter 5), which is reflected in the gate voltage periodicity of the SET source-drain current, we can discriminate between a superconducting state where the gap has nodes ($d_{x^2-y^2}$) or a fully gapped superconducting state in the island. If the symmetry of the order parameter is purely $d_{x^2-y^2}$ no parity effect is expected, however a fully gapped superconductivity would allow for parity effect which manifests as a $1e$ to $2e$ period transition in the source-drain current. In this chapter we describe two different approaches for realizing YBCO SETs.

The detailed data analysis of the measurements performed on one kind of SETs shows the existence of a full gap in the quasiparticle density of states. These results implies the existence of a subdominant imaginary component in the superconducting order parameter, which lifts the zero energy quasiparticles. This complex ground state has been theoretically predicted[85][86], however, up to now, firm experimental proof has been missing,

10.1 Nanojunctions by direct etching through a carbon mask

To realize an YBCO SET we choose to use nanojunctions fabricated by the conventional technique (e-beam lithography, carbon mask and ion milling). The high values of R_N of these types of junctions has already been discussed in chapter 8. With this technology we can easily achieve $R_N > R_Q$. The remaining question concerns the junctions capacitance. As previously mentioned MgO was chosen as a substrate to avoid the large dielectric constant of STO (and the resulting stray capacitance). As discussed in details in paper III we devised an experiment to measure the capacitance of biepitaxial GB junctions on a MgO substrate. SQUIDs were fabricated and the IVCs were measured as a function of an externally applied magnetic field. From the voltage position of the LC resonances (SQUID resonances) we were able to extract the capacitance of the junctions using the SQUID loop inductance value, determined independently. A C_J/Area of $260 \text{ fF}/\mu\text{m}^2$ was extracted. This is an order of magnitude lower than for the GB junctions on a STO substrate (because of the stray capacitance of the STO). Using the extracted C_J/Area value, a junction width of 100 nm and a film thickness of 100 nm will result in a charging energy of approximately 200 mK. The measured C_J is indeed low enough to reach a regime dominated by charging effects at sub kelvin temperatures.

10.2 Big island SET

In our first attempt to realize an YBCO SET we used a layout with a relatively large island. Figure 10.1 shows a typical geometry where the island is made of (103) oriented YBCO film. We have intentionally avoided an island consisting of YBCO (001) due to the possible presence of greenphase in these films, as discussed in chapter 6. Even for well optimized films there is always some amount of greenphase in the (001) YBCO films grown on MgO (110) substrates. This insulating phase could create problems in defining the effective island and/or creating several islands in series or parallel.

The nominal junction widths were in the range 100 - 400 nm. The SETs were placed $20 \mu\text{m}$ away from a gate electrode running through the center of the sample. Two chips with a total of 40 devices, using this layout, were fabricated. As mentioned previously the conventional fabrication method has a rather poor yield resulting in a large spread in junction parameters. Therefore multiple junction widths are needed, since only a few devices

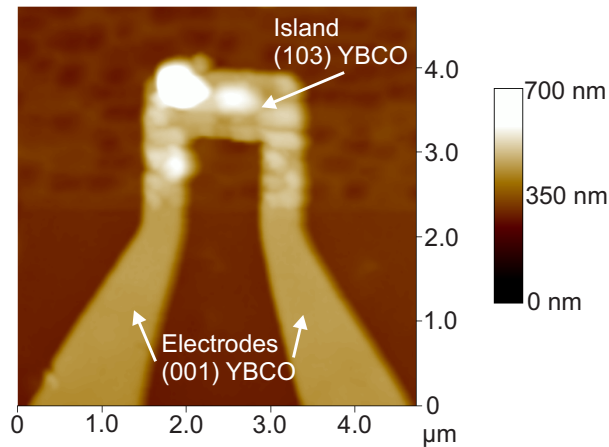


Figure 10.1: AFM image of the SET island (YBCO (103)) and the source-drain electrodes (YBCO (001)).

will reach the regime where charging effects are relevant.

10.2.1 Characterization

To electrically characterize an SET there are two approaches to bias the device and measure the response. The first method is to measure IVCs while stepping the gate voltage. This involves ramping the bias current over the source-drain range while recording the voltage and using a constant gate voltage. When a sweep is finished the gate voltage is incrementally changed and the source-drain sweep is started again. If the SET is of exceptionally high resistance it is also possible to use a voltage biased setup. The second approach is to sweep the gate voltage the full range of interest while keeping the source-drain voltage constant and recording the corresponding current. When one sweep (transfer function) is completed the source-drain bias is incrementally changed and the next gate sweep is started.

In principle the two methods measure the same electric response, although drift and noise jumps in the island charge will appear differently. It seems like a fast change of V_{SD} induces background charge jumps and/or junction resistance fluctuations. The first method gives clear IV characteristics. However, since we are primarily interested in changes of the I_{SD} modulation as a function of the gate the "transfer function method" is the most suitable when looking for a $1e$ to $2e$ period transition.

Device Nr	Junction Width (nm)	E_C (μeV)	R_N (Ω)
Nr 1	200	20	2 M
Nr 2	300	30	14 M
Nr 3	300	500 and 50	2.5 G
Nr 4	400	200 and 60	25 M

Table 10.1: A summary of the parameters for the big island SET. The table shows the total R_N for two junctions in series. Device 3 and 4 both had two distinctly different modulation periods as a function of the gate voltage. The E_C values are roughly approximated from the stability diagrams.

10.2.2 Results for Big island SETs

In total 4 devices showed Coulomb blockade features that could be periodically modulated by a gate voltage. The widths of these devices were 200, 300, 300 and 400 nm (table 10.1 report their R_N and E_C values). Figure 10.2 shows the logarithmic conductance (colorscale) as a function of the gate and source-drain voltage measured at the base temperature of the fridge (16 mK) for a device with 300 nm wide junctions and an interface angle of 0° .

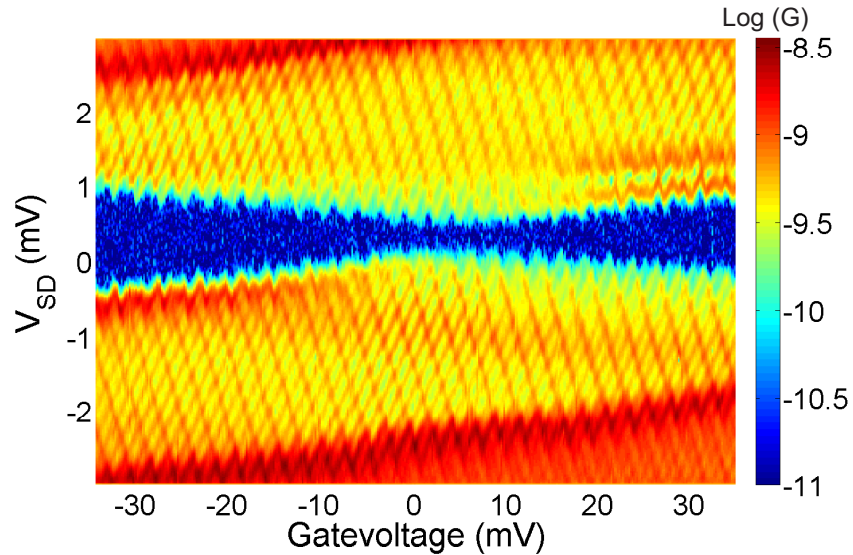


Figure 10.2: Logarithmic conductance as a function of V_{SD} and V_g at a bath temperature of 16 mK for an SET with 300 nm wide junctions (Device Nr 3).

There is a fundamental difference between these data and the theoretical simulation shown in figure 5.3 and 5.4. The data in figure 10.2 have two distinctly different modulations with respect to the gate voltage. A short modulation period on the order of a few mV and a longer one on the order of 100 mV. These effects have been described in earlier studies[87] and stem from an island consisting of multiple grains connected to the two electrodes. The difference in modulation period shows that, the two grains have significantly different capacitance to the gate electrode. This can either be due to a difference in size or electrostatic shielding from the gate electrode (depending on geometric arrangement of islands, source-drain electrodes and gate electrode).

Figure 10.3 a) shows the conductance plot for the same device and a larger gate voltage range at a temperature of 300 mK. The short modulation period has completely disappeared, confirming that the grain responsible for this modulation has a lower charging energy. The temperature dependence and the period of the modulations indeed indicate that we are dealing with two grains of different size: A large grain having large capacitance to the two main electrodes and the gate resulting in a low E_C and a short modulation period. For a smaller grain a higher E_C and a bigger modulation period is expected.

The next step was to examine the behavior of the SET when a magnetic field is applied. Figure 10.3 b) and c) show the $G(V_g, V_{SD})$ measured at fields of 4.5 and 5T (maximum field of the magnet), respectively. The stability diagram is modified when the field is switched on, most clearly at 5T one can see that the blockade region (dark blue) is expanded for the two last diamonds on the right of the stability diagram. However, we do not observe a change of periodicity from $1e$ to $2e$.

Figure 10.4 a) shows the conductance $G(V_g, V_{SD})$ of the second SET with 300 nm wide junctions having $\theta = 90^\circ$ at a magnetic field of 0T. Figure 10.4 b) shows $G(V_g, V_{SD})$ of the same device at an externally applied magnetic field of 4.5 T. The modulation of the Coulomb blockade is completely washed out and only a constant low conductance region is left in the center. Looking at transfer functions at different low biases we have no hint of a doubling of the periodicity.

The analysis of the transport properties of the "big island" samples have shown to be non trivial, especially because of clear multi grain effects. The behavior with a finite magnetic field has not been fully understood and no clear doubling of the periodicity was seen on either of the devices. To simplify the detection and interpretation of the effects that are indicative of a transition between d -wave and fully gapped superconduc-

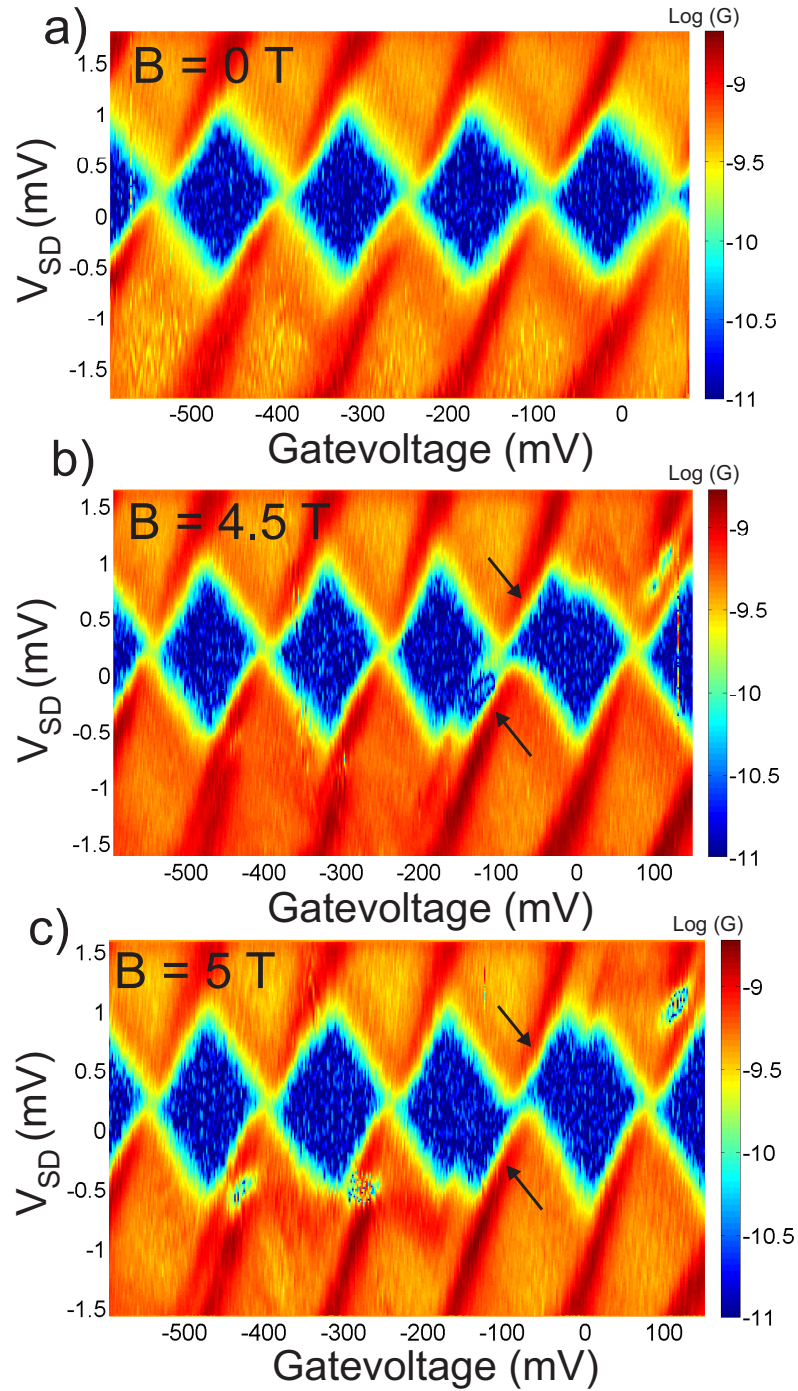


Figure 10.3: Logarithmic conductance as a function of V_{SD} and V_g at a bath temperature of 300 mK and an applied external magnetic field of a) 0T, b) 4.5 T and c) 5T for an SET with 300 nm wide junctions (Device Nr 3).

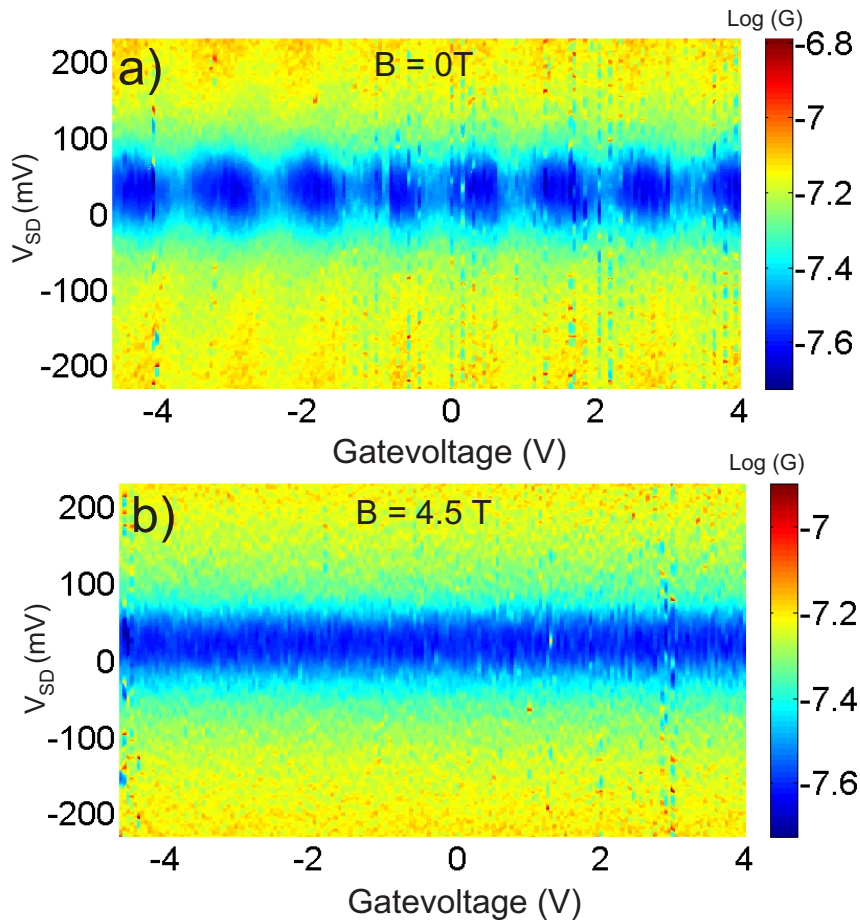


Figure 10.4: Logarithmic conductance as a function of V_{SD} and V_g at a bath temperature of 100 mK and an applied external magnetic field of a) 0T, b) 4.5 T for an SET with 300 nm wide junctions (Device Nr 2)

tivity a new layout was used for the next generation of YBCO SETs. The new layout aimed at creating a single grain island, which would allow us to work with only one single modulation when sweeping the gate voltage.

10.3 Single grain SET

In the new layout we used a different approach to define the islands's geometry. Looking closer at the YBCO (103) films (see figure 6.4 a)) they consists of elliptical grains approximately 500 nm long and 200 nm wide. The aim of the new layout was to define the SET island so as it consists of one

single (103) grain. To achieve this we patterned the seed layer into a 50-200 nm wide wire. When the YBCO film is deposited on top of this thin STO wire using specific growth conditions one can expect to get a single (or double) (103) oriented grain(s), see figure 10.5 a). The source-drain electrodes (dashed lines) are defined and patterned perpendicular to the wire. Figure 10.5 b) shows an AFM image of the finished SET. The dimension of the island grain is approximately $100 \times 200 \times 250 \text{ nm}^3$ (thickness \times length \times width). The gate is once again placed at the side of the SET connected to a common electrode in the center of the sample. The distance between the island and the gate was reduced to $10 \mu\text{m}$ to compensate for the smaller island size. The (001) YBCO film on the MgO (110) substrate grows with the ab planes rotated 45° with respect to the in plane direction of the substrate. This will make a node of the order parameter on the (001)-side of the GBs face a lobe on the (103) grain that constitutes the island.

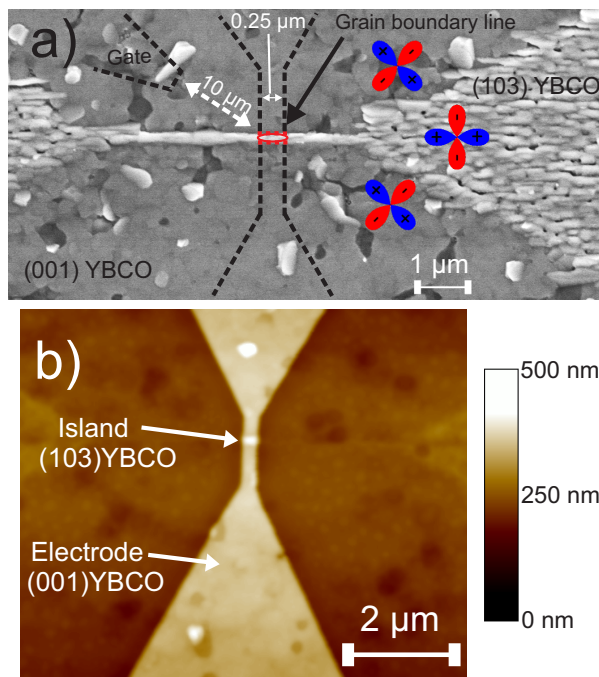


Figure 10.5: a) A SEM image of the YBCO (103) wire before the ion milling to define the SET. The dashed lines shows the region of the mask structure that will define the SET. The triangular structures in the film, on the left and right side of the wire, is used in the lithography process and to make the structures visible in an optical microscope, they serve no purpose for the actual device. b) An AFM image of the final SET after etching.

10.3.1 Results for single grain SET

Figure 10.6 shows I_{SD} as a function of V_{SD} and n_g for positive bias at base temperature (18 mK). This SET displays clear Coulomb oscillations with only one periodicity which tells us that the conducting part of the island behaves as a single grain. Figure 10.7 shows the results for the same device when a magnetic field of 3.9 T is applied. Although the modulations are less clear a pattern of alternating large and small diamonds can be seen. This is consistent with a non zero F value.

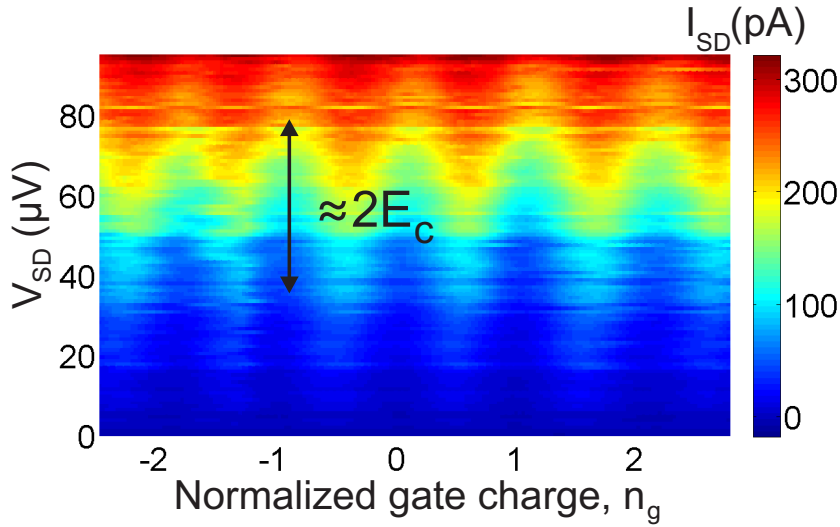


Figure 10.6: Stability diagram at $B = 0$ T and a bath temperature of 18 mK. The color scale shows current. A rough estimation of $2 \cdot E_C$ is marked with an arrow.

10.3.2 Detailed characterization of the device

To gain a deeper understanding of the change that happens when the magnetic field is switched on it is important to look at single transfer functions. Figure 10.8 shows transfer functions measured at 0, 1 and 2 T. The clear change of the periodicity seen here as the field increases is a demonstration of the parity effect in our device. This is the first time parity has been observed in an YBCO SET. In a previous experiment using an YBCO island connected to gold electrodes a fully working SET was realized, although without detecting any parity effect[88].

The distance in gate charge between consecutive peaks can directly be used to calculate F . To extract F from the measurement data one starts with

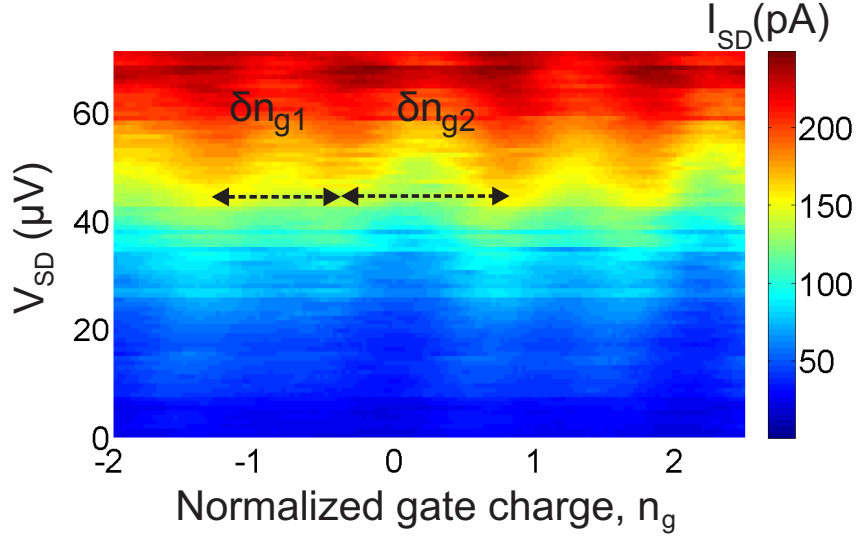


Figure 10.7: Stability diagram at $B = 3.9$ T and a bath temperature of 20 mK. The color scale shows current.

the voltage threshold equation (5.14). We need to know the difference in n_g for two threshold lines corresponding to sequential values of n . This means that we need to express $\delta n_g = n_g(n-1) - n_g(n)$ in terms of F . We look at two threshold lines for an arbitrary but constant value of V_{SD} for junction 1:

$$\begin{aligned} V_{th}^+(n, n_g) &= V_{th}^+(n-1, n_g) \rightarrow \frac{e}{C_2} \left(\frac{1}{2} + (n + n_g(n)) \right) + \frac{C_\Sigma}{eC_2} (\Delta + (-1)^n F) \\ &= \frac{e}{C_2} \left(\frac{1}{2} + (n-1 + n_g(n-1)) \right) + \frac{C_\Sigma}{eC_2} (\Delta + (-1)^{n-1} F) \end{aligned} \quad (10.1)$$

This equation reduces to:

$$\frac{e}{C_2} n_g(n) + \frac{C_\Sigma}{eC_2} (-1)^n F = \frac{e}{C_2} (-1 + n_g(n-1)) + \frac{C_\Sigma}{eC_2} (-1)^{n-1} F \quad (10.2)$$

Rearranging 10.2 and using the definition of δn_g and E_C , for even n , we get:

$$\delta n_g = 1 + F/E_C \quad (10.3)$$

For odd n we will instead get the expression $\delta n_g = 1 - F/E_C$. For an SET with high resistance asymmetry, corresponding to a stability diagram where only one of the two possible conductance (threshold) lines are observed (see figure 5.4 e)), equation 10.3 is valid for any V_{SD} . For a symmet-

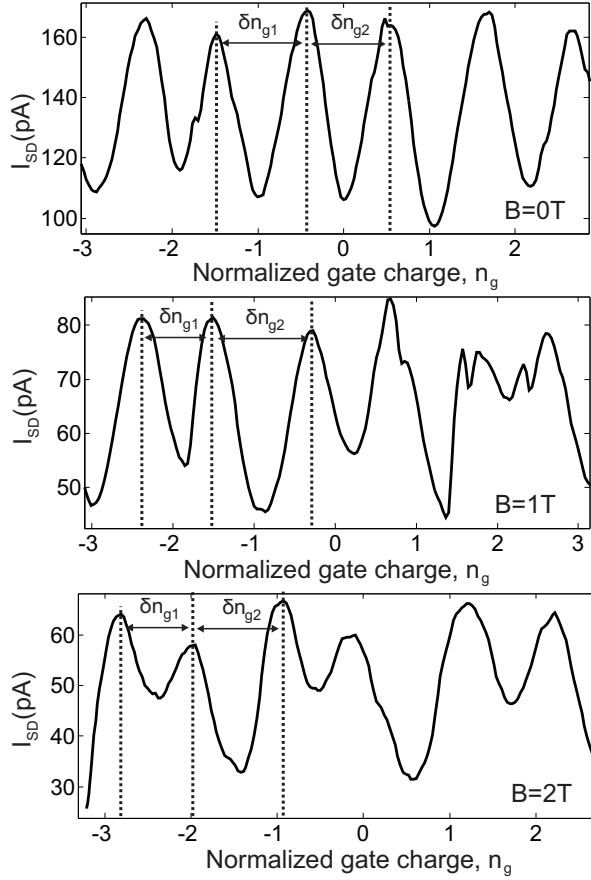


Figure 10.8: Source-drain current as a function of the normalized gate charge. The measurements were done at a) $B=0\text{T}$, b) $B=1\text{T}$ and c) $B=2\text{T}$.

ric transistor this method would only work for V_{SD} values close to $2\Delta/e$. Our SET is asymmetric both in R and C and only one of the lines is visible.

Due to current noise jumps between separate transfer functions our conductance data contains multiple artifacts. Therefore we use the current peaks in the transfer functions at various V_{SD} directly to calculate F . For an asymmetric SET the current peaks follows the threshold lines and exhibit the same F dependent distance in gate voltage between neighboring peaks. The procedure to extract F is now straightforward. Ten of the clearest traces are picked out for the different magnetic fields and the average F is then extracted¹, see Figure 10.9.

¹At first the ratio F/E_C is extracted from the transfer functions. This ratio is used when fitting IV characteristics to theory in the next section, where the fitting parameter E_C is determined.

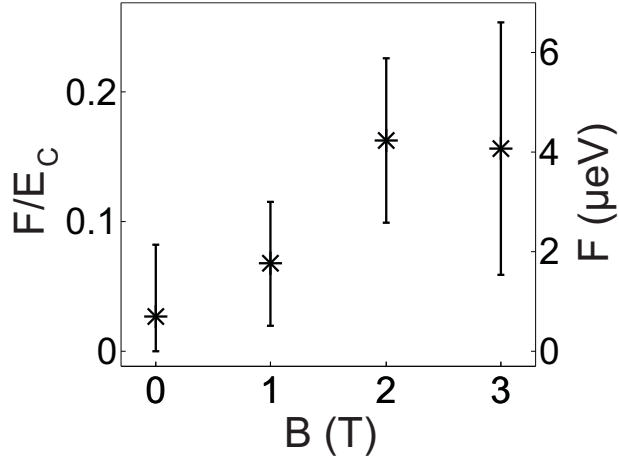


Figure 10.9: The even-odd energy F vs B . The left vertical axis give the F/E_C ratio used when fitting the IVCs. The right axis show the final F values using E_C extracted from the IVC fitting. The error bar is given by the standard deviation of the distribution of F values.

Our device has a small finite value of F at $B = 0$, which clearly grows with increasing applied magnetic field.

10.3.3 Fitting IV characteristics to the orthodox theory to extract C , Δ , T_{eff} and E_C

To extract parameters like Δ , E_C and the effective electron temperature² (T_{eff}) from the data we fit the IV characteristics using the orthodox theory for a NISIN SET where F has been added to the energy expression (as discussed in chapter 5). The choice of NISIN over SISIS is due to the absence of Cooper pair tunneling and Josephson quasiparticle cycles in our data. An attempt using a SISIS model (which includes a separate ΔE for the Cooper pairs and the tunneling formula for SIS junctions) resulted in IV characteristics which could not fit our experimental data. This means that the Δ we extract from fits is related to the island of the SET. It is important to note that the extracted gap Δ is related to the subdominant energy gap of the island resulting in a fully gapped electronic density of states. This subdominant energy gap is much smaller than the maximum of the (dominant) $d_{x^2-y^2}$ gap function.

²The effective electron temperature of the device is expected to be higher than the bath temperature of the fridge during the measurement.

To use the orthodox theory outlined in chapter 5 expressions for the density of states are required. The DOS functions for the source and drain electrodes should in general depend on energy in a $d_{x^2-y^2}$ -wave superconductor. However, in the experimentally relevant interval of energies, $|E| \leq 100\mu eV$, the density of states in the leads remains constant and is dominated by strong contribution from the broad midgap quasiparticle states localized at the surfaces[51][53]. Thus they are effectively constant and we can treat the leads as normal metals. The precise form of the DOS in the island is not known and we choose to model it by the function typical for an s -wave superconductor. This form of the density of states is quite general and naturally arises if a small spectral gap opens up on the constant background. To avoid confusion, it should be emphasized that this does not necessarily imply conventional s -wave superconductivity in the island. Thus, our model is effectively reduced to that of a NISIN SET.

E_C is used as a fitting parameter, but it is first roughly estimated by looking at the size of the diamonds in figure 10.6. The first step is however to determine the capacitances of the junctions and the gate (C_1 , C_2 and C_g). C_g is extracted from the current peaks in the transfer functions by looking at the change in gate (ΔV_g) for a full $2e$ period: $C_g = 2e/\Delta V_g$. The junction capacitances can be extracted from the slope of the current maxima line in the V_{SD}, V_g plane (see figure 5.4 e)). The capacitance can be extracted from the slope of this line ($\partial V_{SD}/\partial V_g^{max}$) by looking at the voltage threshold equation (5.14) and using the definition of n_g ($n_g = V_g C_g/e$). Differentiating with respect to V_g will leave only the third term on the right side giving:

$$\frac{\partial V_{SD}}{\partial V_g^{max}} = \frac{\partial}{\partial V_g^{max}} \frac{e}{C_2} \frac{C_g V_g}{e} = \frac{C_g}{C_2} \quad (10.4)$$

If the second slope is visible (symmetric SET) C_1 can be extracted accordingly using:

$$\frac{\partial V_{SD}}{\partial V_g^{max}} = -\frac{C_g}{C_1} \quad (10.5)$$

Since our device is asymmetric we can only extract the capacitance value of the junction with the higher resistance. The other junction capacitance will have to be left as a variable in the fit of the IVCs (and can be determined through its relation to E_C). From the slope we obtain $C_2 = 1.5$ fF.

We now extract E_C , Δ and T_{eff} at $B = 0T$ by fitting two IVCs at two gate charge values corresponding to maximum and minimum Coulomb blockade for positive V_{SD} . These gate charge values can be determined by first simulating a low resolution stability diagram. Since the maximum/minimum blockade change position on the gate axis when E_C (through its de-

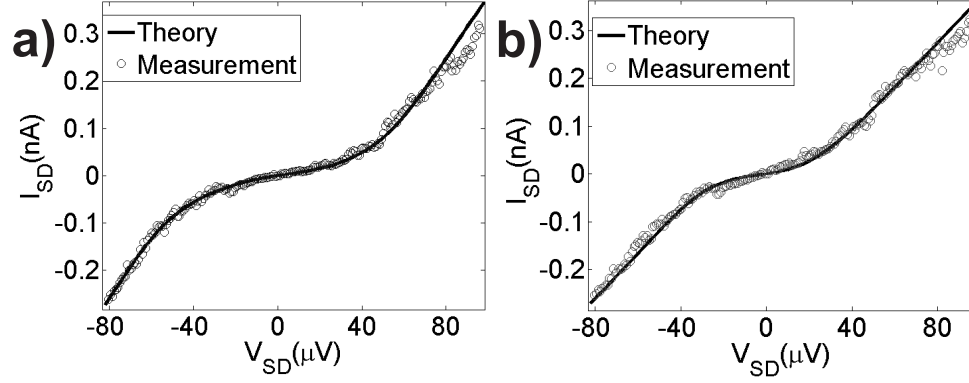


Figure 10.10: Measured and theoretical IV characteristics at $B=0$ T. The a) and b) panel show curves for a gate voltage corresponding to the maximum and minimum blockade at the positive bias side, respectively.

pendence on C_1 and C_2) and Δ are changed one need to iterate between fitting IVCs and calculating the gate charge values until reasonable fits are achieved. The final capacitance values for this device were found to be $C_1 = 2.5$ fF, $C_2 = 1.5$ fF and $C_g = 1.2$ aF. Figure 10.10 shows the two measured IVCs together with the theoretical ones for maximum and minimum Coulomb blockade at $B = 0$ T.

When an acceptable fit was found at $B = 0$ T the same procedure was used for measurements at finite applied magnetic field, with the difference that the charging energy was assumed to be constant for all measurements. Δ as a function of B is plotted in figure 10.11. Δ increases with magnetic field in a similar fashion as F , which is reasonable if the two quantities are connected by equation 5.9. This behavior of Δ and F is opposite to what is seen for Aluminum SETs[59] where both parameters decrease in field.

At fields higher than 3 T the behavior of the SET has been difficult to model and understand. We believe this could be due to vortices entering into the island. A vortex will overcome the entry barrier at an approximate field of $B_s \approx \phi_0/2\pi r\zeta$ [89], where r is the diameter of the sample and ζ the coherence length. For our island we get $B_s \approx 2T$. For fields above this limit the system becomes more complicated and the measurements are not reproducible going back and forth in field. We still observe a strong parity effect at fields $> 3T$, although systematic fitting of IV characteristics has not been possible.

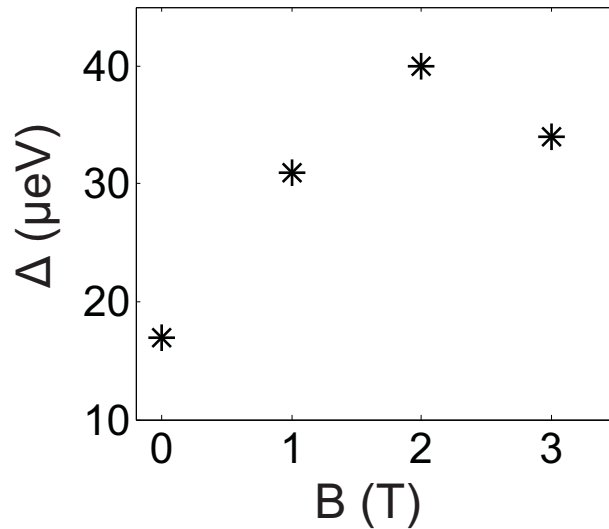


Figure 10.11: Δ vs B extracted by fitting the orthodox theory to experimental IVCs.

10.4 Size quantization

An important issue to consider is if any of the observed behavior in our measurements can have a different explanation. In addition to the electrostatic energies, which governs the SET operation, very tiny islands may have quantized energy levels due to the confinement of electrons[90][91][92] that also affect the dynamics. Devices where this happens are commonly referred to as *quantum dots*. When various levels on the island are filled the system reaches higher energies where the level spacing decreases and for practical considerations eventually become continuous. A major difference between devices only governed by the Coulomb effects and those where size quantization is also relevant is the position of the current peaks on the gate voltage axis. An ideal SET will have periodic oscillations (in the case of parity the period simply doubles) whereas for a quantum dot the peak positions will not only depend on the charging energy but also on the energy level spacing, which varies with the number of electrons added to the island. Figure 10.12 a) shows an example of a transfer function for a quantum dot from Tarucha et. al.[93]; a clear non periodic behavior is seen here. Figure 10.12 b) shows a trace from our SET taken over a larger gate range than the previous data (shown in figure 10.8). We observe that the current peaks are almost perfectly periodic.

In the following we will estimate the average quasiparticle energy level

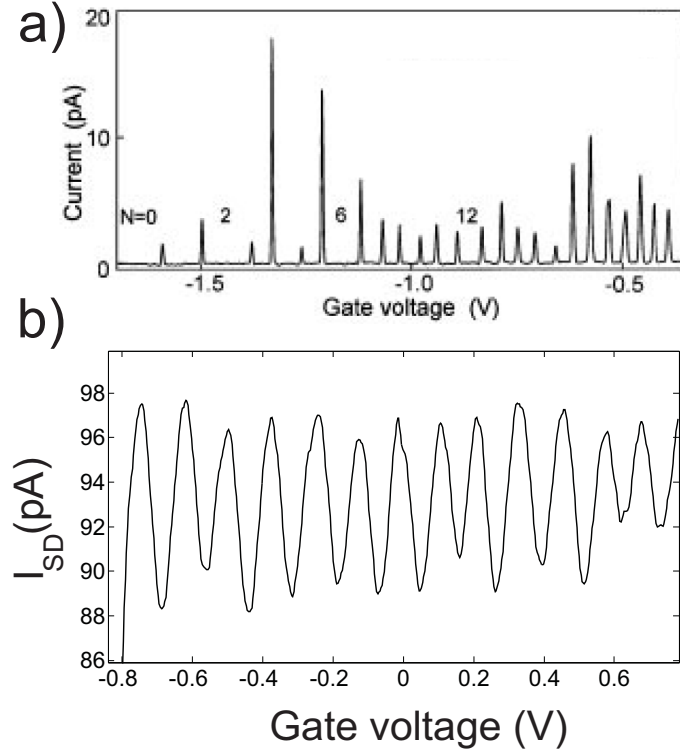


Figure 10.12: a) Transfer function ($I_{SD}(V_g)$) adapted from [93]. b) Averaged transfer function data for our SET acquired at a constant V_{SD} and $B = 0$ T.

spacing, d . From the effective number of quasiparticle states (N_{eff}) and the values of Δ and T_{eff} it is possible to roughly estimate an upper limit for d using equation 5.9. For the quantized energy levels to play a role in the electrical transport this energy needs to be comparable or higher than T_{eff} . Since N_{eff} is the number of available states in a region $k_B T_{eff}$ above the gap a rough approximation can be given by $N_{eff} \approx k_B T_{eff} / d$, leading to:

$$d = k_B T_{eff} e^{-\frac{\Delta - F}{k_B T_{eff}}} \quad (10.6)$$

T_{eff} is a variable parameter when fitting the theoretical IVCs to the measurement data. However we have realized that our quite simple model of a NISIN SET overestimates T_{eff} . Figure 10.13 shows a "flattened" current plot, this means that the average (over gate voltage) IV characteristic has been subtracted from the data, leaving only the modulating current peaks. The a) panel shows our measurement data at 2T while b) and c) show simulated data using the NISIN model at 120 (fitted temperature) and 50 mK

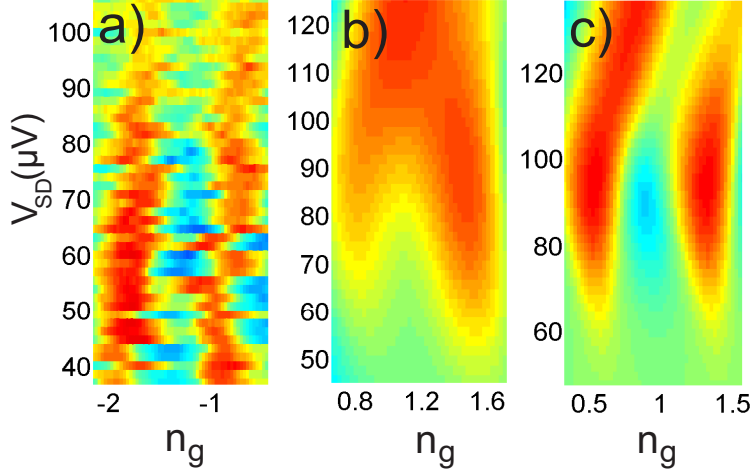


Figure 10.13: Flattened stability diagram emphasizing the current maxima. a) Measured data at 2T, b) simulated data using the experimental parameters extracted from the 2T data and $T_{eff} = 120$ mK (from the IVC fits) and in c) $T_{eff} = 50$ mK.

respectively. At the higher temperature the simulated peaks start to merge. However, we do not see this effect in our measurements, which tells us that the value of $T_{eff} = 120$ mK we extract from the IVCs is overestimated. Despite this fact, it is still possible to give an upper limit of d using equation 10.6. From our fitted parameters we extract a maximum d of $\approx 1 \mu\text{V}$ (≈ 12 mK). The exponential decrease of d as T_{eff} decreases ensure that even with an error in temperature of 40-50% the average quasiparticle energy level spacing of our system is small enough and it should not have any impact on the transport mechanisms in our SET.

10.5 Conclusions

For a pure $d_{x^2-y^2}$ order parameter together with disorder and scattering the quasiparticle density of states is finite even at zero energy[4]. In an SET this will make even and odd number of excess quasiparticles on the island energetically equivalent ($F = 0$). The clear presence of a non-zero F in our device therefore shows that a gap is indeed open for all directions in k-space.

The fits and simulations strongly suggest that the fully gapped superconducting state only appear in the island of the device. There are however

still unsettled questions. There are two different scenarios that support a fully gapped spectrum on the island. Either a $d_{x^2-y^2} + id_{xy}$ state is fully supported in bulk of the island[85] or a $d_{x^2-y^2} + is$ state that is formed at the surface of the grain[86][94] extending into the bulk by proximity effect. A surface induced subdominant state decays exponentially inside the bulk of the YBCO. However, the small dimensions of the island might support the proximity effect resulting in a fully gapped DOS within the whole grain, albeit with a decaying gap inside the island. From the results presented here it is not possible to, with certainty, correlate the observed full gap in the quasiparticle excitation spectrum to one of these two scenarios.

Chapter 11

Conclusions

In this thesis we have demonstrated the presence of a parity dependent free energy in a mesoscopic YBCO island in a Single Electron Transistor configuration. This finding implies the existence of a fully gapped quasiparticle density of states and consequently that the YBCO order parameter goes beyond a pure d -wave symmetry. Our observation is compatible with a subdominant pairing channel resulting in an imaginary order parameter admixed to the dominant d -wave order parameter.

Future plans will involve systematic studies on the existence of fully gapped superconductivity in islands of different sizes and dopings. By varying the island size it should be possible to eventually distinguish between a gap originating from the bulk or a surface induced one. By studying islands of different doping one will be able to map a phase diagram for the subdominant pairing channel and compare it to that of the dominant d -wave.

To realize YBCO devices where charging effects are dominant we have developed and tested two technologies to fabricate nanoscale YBCO GBs. Although there is still some work to be done regarding the yield and reproducibility issues, the two methods allow us to make junctions with a wide range of resistivities and critical current densities.

The development of a new soft nanopatterning technique gives access to pristine junctions that in the future could be used for different devices to further probe the quasiparticle excitation spectrum of HTS.

Appendix A

Fabrication of biepitaxial grain boundaries

Figure A.1 summarizes the main fabrication steps involved in the creation of biepitaxial YBCO junctions on MgO (110) substrates.

- a) A thin seed layer of STO is deposited by PLD on the MgO (110) substrate. The seed layer will grow epitaxially having the (110) orientation.
- b) A 50 nm thick amorphous carbon film is deposited by e-beam evaporation on top of the seed layer. Next two layers of e-beam resists (MCC Copolymer and ZEP520) are spun on the sample.
- c) The seed layer geometry is exposed by E-beam.
- d) The exposed area is developed (removed) by two different chemical developers. A thin chromium film is deposited by E-beam evaporation.
- e) The chromium, on top of the remaining resist bilayer, is removed by lift off in hot acetone.
- f) A low power Oxygen plasma is used to remove the carbon that is not protected by chromium.
- g) Argon ion milling is used to etch away the STO film that is not covered by carbon. The chromium and part of the carbon mask is also removed in this process.
- h) Oxygen plasma is used to remove the remaining carbon.
- i) A 100-120 nm thick YBCO film is deposited by PLD. In situ ion milling is performed in the PLD chamber before the deposition to remove the top layers of the MgO surface.

APPENDIX A. FABRICATION OF BIEPITAXIAL GRAIN BOUNDARIES

- j) A 200 nm thick gold film is deposited by e-beam evaporation or sputtering to protect the YBCO from the remaining fabrication steps and to act as pads to connect the sample to our measurement setup.
- k) Photoresist (Shipley S-1813) is spun on the sample. Photolithography is used to define the gold pads.
- l) The exposed resist is removed by the MF-319 developer.
- m) Argon ion milling is used to remove part of the gold film not covered by the resist mask. Approximately 40 nm is left to protect the YBCO in the final fabrication steps.
- n) The resist is removed by a combination of hot acetone and oxygen plasma.
- o) A 120 nm thick carbon film is deposited by e-beam evaporation.
- p) Steps b)-f) are now repeated to create a new carbon-chrome mask. This time the actual device or junction is patterned.
- q) Argon ion milling is used to etch away all of the YBCO not covered by the carbon mask.
- r) The carbon is removed by oxygen plasma and a short ion milling step is carried out to remove the thin gold layer still present on top of the junctions.

In step p) and q) the width, w_J , of the grain boundary is defined by the e-beam lithography and ion milling.

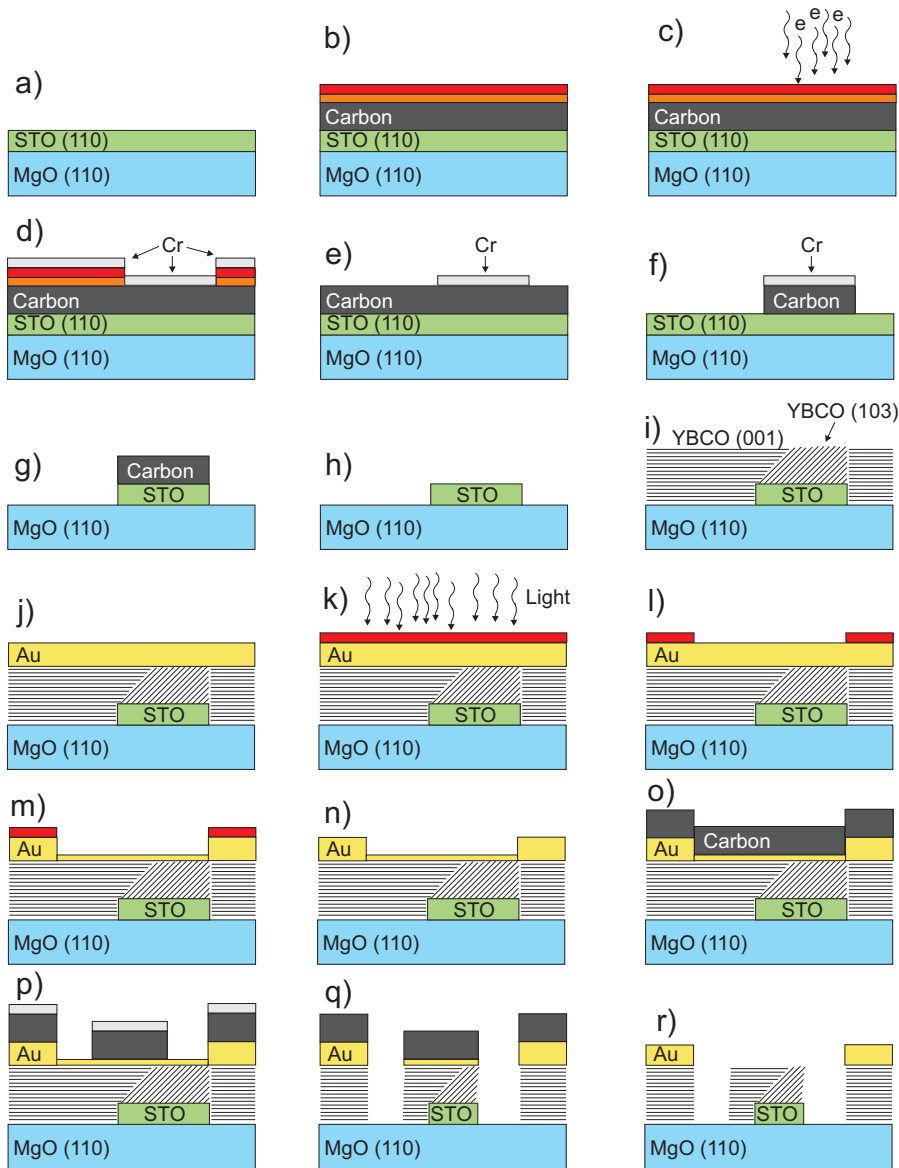


Figure A.1: An overview of the different steps required to deposit and pattern biepitaxial grain boundaries.

APPENDIX A. FABRICATION OF BIEPITAXIAL GRAIN BOUNDARIES

Acknowledgements

First of all I would like to thank my supervisor Floriana Lombardi. For introducing me to the field of high temperature superconductors, for all the support over the years and for the help to make this thesis readable.

Shahid Nawaz, with whom I shared office with for several years, we have had many interesting and entertaining discussions about politics, religion, and even some about science. You have made my work here much more enjoyable.

Mattias Torstensson, we shared office during my first years at Chalmers. Thanks for all the hilarious and nerdy discussions we had.

I would like to thank a number of talented individuals that I have had the pleasure to work with over the past five years, without whom this work would not have been possible.

My assistant supervisor Thilo Bauch for teaching me a lot about electronics, cryogenics and low temperature physics.

Karin Cedergren who helped me out when I was a new PhD student and taught me all about making films and grain boundaries.

Henrik Pettersson and Eva Olsson in the Microscopy and Microanalysis group who provided invaluable help in understanding our grain boundaries.

Dmitry Golubev and Mikael Fogelström for their theoretical help in understanding our SETs.

Henrik Frederiksen for his hard work in keeping all the deposition equipment vital to my research in excellent condition.

I would also like to thank all the people at the Quantum Device Physics Laboratory who have helped me in these past years and made this experience very enjoyable.

Finally I would like to thank my family for their support during this time.

Bibliography

- [1] P. Monthoux, D. Pines and G. G. Lonzarich, *Superconductivity without phonons*, *Nature*, textbf450, 1177 (2007)
- [2] N. Doiron-Leyraud, C. Proust, D. LeBoeuf, J. Levallois, J. Bonnemaison, R. Liang, D. A. Bonn, W. N. Hardy and L. Taillefer, *Quantum oscillations and the Fermi surface in an underdoped high- T_c superconductor*, *Nature*, **447**, 565 (2007)
- [3] K. Krishana, N. P. Ong, Q. Li, G. D. Gu and N. Koshizuka, *Plateaus Observed in the Field Profile of Thermal Conductivity in the Superconductor $\text{Bi}_2\text{Sr}_2\text{CaCu}_2\text{O}_8$* , *Science* **277**, 83 (1997)
- [4] N. E. Hussey, *Low-energy quasiparticles in high- T_c cuprates*, *Advances in Physics*, **51**, 1685 (2002)
- [5] J. Bardeen, N. Cooper and J. R. Schrieffer, *Phys. Rev., Theory of Superconductivity*, **108**, 1175 (1957)
- [6] J. G. Bednorz and K. A. Müller, *Possible High T_c Superconductivity in the Ba - La- Cu- O System*, *Z. Phys. B* **64**, 189 (1986)
- [7] M. K. Wu, et.al., *Superconductivity at 93 K in a New Mixed-Phase Y-Ba-Cu-O Compound System at Ambient Pressure*, *Phys. Rev. Lett.*, **58**, 908 (1987)
- [8] A. S. Bhalla, R. Guo and R. Roy, *The perovskite structure - a review of its role in ceramic science and technology*, *Mat. Res. Innovat.*, **4**, 3 (2000)
- [9] W. Pickett, *Electronic structure of the high-temperature oxide superconductors*, *Rev. Mod. Phys.*, **61**, 433 (1989)
- [10] A. Di Chiara, F. Lombardi, F. Miletto Granozio, U. Scotti di Uccio, M. Valentino. F. Tafuri, A. Del Vecchio, M. F. De Riccardis and L.

BIBLIOGRAPHY

- Tapfer, *Structure and morphology of MgO/YBCO bilayers for biepitaxial junctions*, *Physica C*, **273**, 30 (1996)
- [11] B. Wuyts, V. V. Moshchalkov and Y. Bruynseraede, *Resistivity and Hall effect of metallic oxygen-deficient $YBa_2Cu_3O_x$ films in the normal state*, *Phys. Rev. B*, **53**, 9418 (1996)
- [12] T. Timusk and B. Statt, *The pseudogap in high-temperature superconductors: an experimental survey*, *Rep. Prog. Phys.*, **62**, 61 (1999)
- [13] D. N. Basov and T. Timusk, *Electrodynamics of high- T_c superconductors*, *Rev. Mod. Phys.*, **77**, 721 (2005)
- [14] M. R. Norman, *The Challenge of Unconventional Superconductivity*, *Science*, **332**, 196 (2011)
- [15] D. N. Zheng, A. M. Campbell, J. D. Johnson, J. R. Cooper, F. J. Blunt, A. Porch and P. A. Freeman, *Magnetic susceptibilities, critical fields, and critical currents of Co- and Zn-doped $YBa_2Cu_3O_7$* , *Phys. Rev. B*, **49**, 1417 (1994)
- [16] C. C. Homes, S. V. Dordevic, D. A. Bonn, R. Liang, W. N. Hardy and T. Timusk, *Coherence, incoherence, and scaling along the c axis of $YBa_2Cu_3O_{6+x}$* , *Phys. Rev. B*, **71**, 184515 (2005)
- [17] C.C Tsuei and J.R. Kirtley, *Pairing symmetry in cuprate superconductors*, *Rev. Mod. Phys.*, **72**, 969 (2000)
- [18] V. Harlingen, *Phase-sensitive tests of the symmetry of the pairing state in the high-temperature superconductors-Evidence for $d_{x^2-y^2}$ symmetry* *Rev. Mod. Phys.*, **67**, 515 (1995)
- [19] J. R. Kirtley, et.al., *Angle-resolved phase-sensitive determination of the in-plane gap symmetry in $YBa_2Cu_3O_{7-\delta}$* , *Nature Physics*, **2**, 190 (2006)
- [20] L. H. Greene, M. Covington, M. Aprili, E. Badica and D. E. Pugel, *Observation of broken time-reversal symmetry with Andreev bound state tunneling spectroscopy*, *Physica B*, **280**, 159 (2000)
- [21] G. Elhalel, R. Beck, G. Leibovitch and G. Deutscher, *Transition from a Mixed to a Pure d -Wave Symmetry in Superconducting Optimally Doped $YBa_2Cu_3O_{7-x}$ Thin Films Under Applied Fields*, *Phys. Rev. Lett.*, **98**, 137002 (2007)

-
- [22] M. Covington, et.al., *Observation of Surface-Induced Broken Time-Reversal Symmetry in $YBa_2Cu_3O_7$ Tunnel Junctions*, Phys. Rev. Lett., **79**, 277 (1997)
- [23] B. D. Josephson, *Possible new effects in superconductive tunnelling*, Phys. Lett., **1**, 251 (1962)
- [24] M. Tinkham, *Introduction to Superconductivity*, (2004), Dover Publications, New York, 2nd edition
- [25] T. Lindström, J. Johansson, T. Bauch, E. Stepantsov, F. Lombardi and S. A. Charlebois, *Josephson dynamics of bicrystal d-wave $YBa_2Cu_3O_{7-\delta}$ dc-SQUIDS* Phys. Rev. B, **74**, 014503 (2006)
- [26] J. R. Waldram, *Superconductivity of metals and cuprates* (1996) J W Arrowsmith Ltd, Bristol, ISBN 0852743351
- [27] A. Barone, *Physics and Applications of the Josephson Effect*, John Wiley & Sons, New York, 1982
- [28] T. V. Duzer, C. W. Turner, *Superconductive devices and circuits* (1999) Prentice Hall, ISBN 0132627426
- [29] J.H. Miller, G. H. Gunaratne, J. Huang and T. D. Golding, *Enhanced quantum interference effects in parallel Josephson junction arrays*, Appl. Phys. Lett., **59**, 3330 (1991)
- [30] K. Licharev, *Dynamics of Josephson junctions and circuits*, (1986) Gordon and Breach Science Publishers, 1st edition ISBN 2881240429
- [31] X.G. Qui, *High temperature superconductors*, (2011), Woodhead Publishing, Philadelphia
- [32] F. Lombardi, Z. G. Ivanov, G. M. Fischer, E. Olsson and T. Claeson, *Transport and structural properties of the top and bottom grain boundaries in $YBa_2Cu_3O_{7-\delta}$ step-edge Josephson junctions* Appl. Phys. Lett. **72**, 249 (1998)
- [33] C. P. Foley, E. E. Mitchell, S. K. H. Lam, B. Sankrithyan, Y. M. Wilson, D. L. Tilbrook and S. J. Morris, *Fabrication and Characterisation of YBCO Single Grain Boundary Step Edge Junctions*, IEEE Trans. Appl. Supercond., **9**, 4281 (1999)

BIBLIOGRAPHY

- [34] A. Marx, U. Fath, L. Alff and R. Gross, *Correlation of critical current and resistance fluctuations in bicrystal grain boundary Josephson junctions*, Appl. Phys. Lett., **67**, 1929 (1995)
- [35] R. Gross, P. Chaudhari, M. Kawasaki and A. Gupta, *Scaling behavior in electrical transport across grain boundaries in $YBa_2Cu_3O_{7-\delta}$ superconductors*, Phys. Rev. B, **42**, 10735 (1990)
- [36] H. Hilgenkamp and J. Mannhart, *Grain boundaries in high- T_c superconductors*, Rev. Mod. Phys., **74**, 485 (2002)
- [37] N. D. Brownig, J. P. Budan, P. D. Nellist, D. P. Norton, M. F. Chisholm and S. J. Pennycook, *The atomic origins of reduced critical currents at [001] tilt grain boundaries in $YBa_2Cu_3O_{7-\delta}$ thin films*, Physica C, **294**, 183 (1998)
- [38] S. E. Babcock and D. C. Larbalestier, *Bicrystal studies of high transition temperature superconductors*, J. Phys. Chem. Solids, **55**, 1125 (1994)
- [39] B. H. Moeckly, D. K. Lathrop and R. A. Buhrman, *Electromigration study of oxygen disorder and grain-boundary effects in $YBa_2Cu_3O_{7-\delta}$ thin films*, Phys. Rev. Lett., **47**, 400 (1993)
- [40] R. Gross and B. Mayer, *Transport processes and noise in $YBa_2Cu_3O_{7-\delta}$ grain boundary junctions*, Physica C, **180**, 235 (1991)
- [41] A. Marx and R. Gross, *Scaling behavior of $1/f$ noise in high-temperature superconductor Josephson junctions*, Appl. Phys. Lett., **70**, 120 (1997)
- [42] O. M. Froehlich, P. Richter, A. Beck, D. Koelle and R. Gross, *Barrier Properties of Grain Boundary Junctions in High- T_c Superconductors*, IEEE Trans. App. Supercond. **7**, 3189, (1997)
- [43] F. Herbstritt, T. Kemen, L. Alff, A. Marx and R. Gross, *Transport and noise characteristics of submicron high-temperature superconductor grain-boundary junctions*, Appl. Phys. Lett., **78**, 955 (2001)
- [44] J. Mannhart and H. Hilgenkamp, *Possible influence of band bending on the normal state properties of grain boundaries in high- T_c superconductors*, Materials Science and Engineering, **B56**, 77 (1998)

- [45] H. Hilgenkamp and J. Mannhart, *Superconducting and normal-state properties of $YBa_2Cu_3O_{7-\delta}$ -bicrystal grain boundary junctions in thin films*, Appl. Phys. Lett., **73**, 265 (1998)
- [46] C. T. Rogers and R. A. Buhrman, *Composition of $1/f$ Noise in Metal-Insulator-Metal Tunnel Junctions*, Phys. Rev. Lett., **53**, 1272 (1984)
- [47] F. Lombardi, F. Tafuri, F. Ricci, F. Miletto Granozio, A. Barone, G. Testa, E. Sarnelli, J. R. Kirtley and C. C. Tsuei, *Intrinsic d -Wave Effects in $YBa_2Cu_3O_{7-\delta}$ Grain Boundary Josephson Junctions*, Phys. Rev. Lett., **89**, 207001 (2002)
- [48] A. H. Miklich, J. Clarke, M. S. Colclough and K. Char, *Flicker ($1/f$) noise in biepitaxial grain boundary junctions of $YBa_2Cu_3O_{7-\delta}$* , Appl. Phys. Lett., **60**, 1899 (1992)
- [49] A. Marx, U. Fath, W. Ludwig, R. Gross and T. Amrein, *$1/f$ noise in $Bi_2Sr_2CaCu_2O_{8+x}$ bicrystal grain-boundary Josephson junctions*, Phys. Rev. B, **51**, 6735 (1995)
- [50] M. Sigrist and T. M. Rice, *Unusual paramagnetic phenomena in granular high-temperature superconductors - A consequence of d -wave pairing?*, Rev. Mod. Phys., **67**, 503 (1995)
- [51] C. Hu, *Midgap Surface States as a Novel Signature for $d_{x^2-y^2}$ -Wave Superconductivity* Phys. Rev. Lett., **72**, 1526 (1994)
- [52] T. Löfwander, V. S. Shumeiko and G. Wendin, *Andreev bound states in high- T_c superconducting junctions*, Supercond. Sci. Technol., **14**, R53 (2001)
- [53] L. Alff, et.al., *Observation of bound surface states in grain-boundary junctions of high-temperature superconductors*, Phys. Rev. B, **58**, 11197 (1998)
- [54] E. Il'ichev, V. Zakosarenko, R. P. J. IJsselsteijn, H. E. Hoening, V. Schultze, H. G. Meyer, M. Grajcar and R. Hlubina, *Anomalous periodicity of the current-phase relationship of grain-boundary Josephson junctions in high- T_c superconductors*, Phys Rev. B, **60**, 3096 (1999)
- [55] L. S. Kuzmin and D. B. Haviland, *Observation of the Bloch Oscillations in an Ultrasmall Josephson junction*, Phys. Rev. Lett., **67**, 2890 (1991)

BIBLIOGRAPHY

- [56] D. V. Averin and K. K. Likharev, *Single-electronics*, in B. Altshuler et al. (eds.), *Mesoscopic Phenomena in Solids*, Elsevier Science Publishers, (1991) pp 173-271
- [57] D. V. Averin and Y. V. Nazarov, *Single-Electron Charging of a Superconducting Island*, *Phys. Rev. Lett.*, **69**, 1993 (1992)
- [58] M. T. Tuominen, J. M. Hergenrother, T. S. Tighe and M. Tinkham, *Experimental Evidence for Parity-Based $2e$ Periodicity in a Superconducting Single-Electron Tunneling Transistor*, *Phys. Rev. Lett.*, **69**, 1997 (1992)
- [59] M. T. Tuominen, J. M. Hergenrother, T. S. Tighe and M. Tinkham, *Even-odd electron number effects in a small superconducting island: Magnetic-field dependence*, *Phys. Rev. B*, **47**, 11599 (1993)
- [60] R. J. Fitzgerald, S. L. Pohlen and M. Tinkham, *Observation of Andreev reflection in all-superconducting single-electron transistors*, *Phys. Rev. B*, **57**, R11073 (1998)
- [61] Y. Nakamura, C. D. Chen and J. S. Tsai, *Quantitative analysis of Josephson-quasiparticle current in superconducting single-electron transistors*, *Phys. Rev. B*, **53**, 8234 (1996)
- [62] P. Hadley, E. Delvigne, E. H. Visscher, S. Lähteenmäki and J.E. Mooij, *$3e$ tunneling processes in a superconducting single-electron tunneling transistor*, *Phys. Rev. B*, **58**, 15317 (1998)
- [63] T. M. Eiles, J. M. Martinis and M. H. Devoret, *Even-Odd Asymmetry of a Superconductor Revealed by the Coulomb Blockade of Andreev Reflection*, *Phys. Rev. Lett.*, **70**, 1862 (1993)
- [64] J. M. Hergenrother, M. T. Tuominen and M. Tinkham, *Charge Transport by Andreev Reflection through a Mesoscopic Superconducting Island*, *Phys. Rev. Lett.*, **72**, 1742 (1994)
- [65] G. E. Blonder, M. Tinkham and T. M. Klapwijk, *Transition from metallic to tunneling regimes in superconducting microconstrictions: Excess current, charge imbalance, and supercurrent conversion*, *Phys. Rev. B*, **25**, 4515 (1982)
- [66] R. Dolata, H. Scherer, A. B. Zorin and J. Niemeyer, *Single electron transistors with high-quality superconducting niobium islands*, *Appl. Phys. Lett.*, **80**, 2776 (2002)

- [67] A. M. Savin, M. Meschke, J. P. Pekola, Y. A. Peshkin, T. F. Li, H. Im and J. S. Tsai, *Parity effect in Al and Nb single electron transistors in a tunable environment*, Appl. Phys. Lett., **91**, 063512 (2007)
- [68] T. Bauch, T. Lindström, F. Tafuri, G. Rotoli, P. Delsing, T. Claeson and F. Lombardi, *Quantum Dynamics of a d-Wave Josephson Junction*, Science, **311**, 57 (2006)
- [69] D. Stornaiuolo, G. Rotoli, K. Cedergren, D. Born, T. Bauch, F. Lombardi, and F. Tafuri, *Submicron YBaCuO biepitaxial Josephson junctions: d-wave effects and phase dynamics*, J. Appl. Phys., **107**, 113901 (2010)
- [70] J.M. Phillips, *Substrate selection for high-temperature superconducting thin films*, J. Appl. Phys., **79**, 1829 (1995)
- [71] R. C. Neville, B. Hoeneisen and C. A. Mead, *Permittivity of Strontium Titanate*, J. Appl. Phys., **43**, 2124 (1972)
- [72] F. Tafuri, et.al., *Microstructure and Josephson phenomenology in 45^{circ} tilt and twist YBa₂Cu₃O_{7- δ} artificial grain boundaries*, Phys. Rev. B, **59**, 11523 (1999)
- [73] R. M. Hazen, L. W. Finger, R. J. Angel, C. T. Prewitt, N. L. Ross, H. K. Mao, C. G. Hadidiacos, P. H. Hor, R. L. Meng and C. W. Chu, *Crystallographic description of phases in the Y-Ba-Cu-O superconductor*, Phys. Rev. B, **35**, 7238 (1987)
- [74] T. B. Lindemer, F. A. Washburn, C. S. MacDougall, R. Feenstra and O. B. Cavin, *Decomposition of YBa₂Cu₃O_{7-x} and YBa₂Cu₄O₈ for P_{O₂} < 0.1 MPa*, Physica C, **178**, 93 (1991)
- [75] R. K Williams, K. B. Alexander, J. Brynstad, T. J. Henson, D. M. Kroegar, T. B. Lindemer, G. C. Marsh, J. O. Scarbrough and E.D Specht, *Oxidation induced decomposition of YBa₂Cu₃O_{7-x}*, J. Appl. Phys., **70**, 906 (1991)
- [76] U. Scotti di Uccio, F. Miletto Granozio, A. Di Chiara, F. Tafuri, O. I. Lebedev, K. Verbist and G. van Tendeloo, *Phase competition between Y₂BaCuO and Y₂O₃ precipitates in Y-rich YBCO thin films*, Physica C, **321**, 162 (1999)
- [77] K. Bladh, D. Gunnarsson, E. Hürfeld, S. Devi, C. Kristoffersson, B. Smålander, S. Pehrson, T. Claeson, P. Delsing and M. Taslakov,

BIBLIOGRAPHY

- Comparison of cryogenic filters for use in single electronics experiments*, Rev. Sci. Inst. **74**, 1323 (2003)
- [78] E. Berg, E. Fradkin and S. A. Kivelson, *Charge-4e superconductivity from pair-density-wave order in certain high-temperature superconductors*, Nat. Phys., **5**, 830 (2009)
- [79] A. A. Aligia, A. P. Kampf, and J. Mannhart, *Quartet Formation at (100)/(110) Interfaces of d-Wave Superconductors*, Phys. Rev. Lett., **94**, 247004 (2005)
- [80] P. A. Rosenthal, M. R. Beasley, K. Char, M. S. Colclough, and G. Zaharchuk, *Flux focusing effects in planar thin-film grain-boundary Josephson junctions* Appl. Phys. Lett., **59**, 2482 (1991)
- [81] Y. Zuev, M. S. Kim, and T. R. Lemberger, *Correlation between Superfluid Density and TC of Underdoped $YBa_2Cu_3O_{6+x}$ Near the Superconductor-Insulator Transition*, Phys. Rev. Lett., **95**, 137002 (2005)
- [82] J. Johansson, K. Cedergren, T. Bauch and F. Lombardi, *Properties of inductance and magnetic penetration depth in (103)-oriented $YBa_2Cu_3O_{7-\delta}$ thin films*, Phys. Rev. B, **79**, 214513 (2009)
- [83] M. V. Liatti, U. Poppe, and Y. Y. Divin, *Low-frequency voltage noise and electrical transport in [100]-tilt $YBa_2Cu_3O_{7-x}$ grain-boundary junctions* Appl. Phys. Lett. **88**, 152504 (2006)
- [84] S. Machlup, *Noise in Semiconductors: Spectrum of a Two-Parameter Random Signal*, J. Appl. Phys., **25**, 341 (1954)
- [85] R.B. Laughlin, *Magnetic Induction of $d_{x^2-y^2} + id_{xy}$ Order in High-Tc Superconductors*, Phys. Rev. Lett., **80**, 5188 (1998)
- [86] M. Fogelström, D. Rainer, and A. Sauls, *Tunneling into Current-Carrying Surface States of High-Tc Superconductors*, Phys. Rev. Lett., **79**, 281 (1997)
- [87] A. V. Danilov, D. S. Golubev and S. E. Kubatkin, *Tunneling through a multigrain system: Deducing sample topology from nonlinear conductance*, Phys. Rev. B, **65**, 125312 (2002)
- [88] S. E. Kubatkin, A. Y. Tzalenchuk, Z. G. Ivanov, P. Delsing, R. I. Shekhter and T. Claeson, *Coulomb blockade electrometer with a high-Tc island*. JETP Lett., **63**, 126 (1996)

- [89] G. Stejic, A. Gurevich, E. Kadyrov, D. Christen, R. Joynt and D. C. Larbalestier, *Effect of geometry on the critical currents of thin films*, Phys. Rev. B., **49**, 1274 (1994)
- [90] L. Kouwenhoven and C. Marcus, *Quantum dots*, Physics World, June, pp 35-39 (1998)
- [91] M. A. Kasfner *ARTIFICIAL ATOMS*, Physics today, January, pp 24-31 (1993)
- [92] R. Hanson, L. P. Kouwenhoven, J. R. Petta, S. Tarucha and L. M. K. Vandersypen, *Spins in few-electron quantum dots*, Rev. Mod. Phys., **79**, 1217 (2007)
- [93] S. Tarucha, D. G. Austing, T. Honda, R. J. van der Hage and L. P. Kouwenhoven, *Shell Filling and Spin Effects in a Few Electron Quantum Dot*, Phys. Rev. Lett., **77**, 3613 (1996)
- [94] Y. Dagan and G. Deutscher, *Doping and Magnetic Field Dependence of In-Plane Tunneling into $YBa_2Cu_3O_{7-x}$: Possible Evidence for the Existence of a Quantum Critical Point* Phys. Rev. Lett., **87**, 177004 (2001)

